

UNDERSTANDING FILM FORMATION MECHANISM IN LATEX DISPERSIONS

Submitted in Partial Fulfillment of the Requirements for the Degree of

DOCTOR OF PHILOSOPHY

In

CHEMICAL ENGINEERING

By

KARNAIL B. SINGH

(Roll No. 03402601)

Under the guidance of

Prof. Mahesh S. Tirumkudulu



**DEPARTMENT OF CHEMICAL ENGINEERING
INDIAN INSTITUTE OF TECHNOLOGY BOMBAY
MUMABI 400 076**

2008



DEDICATED
TO
MUMMY & PAPA
AND
LOVING ISHU

Thesis Approval Sheet

The thesis titled: “**UNDERSTANDING FILM FORMATION
MECHANISM IN LATEX DISPERSIONS**”

by: **Karnail B. Singh**

is approved for the degree of **DOCTOR OF PHILOSOPHY:**

EXAMINERS

[Prof. Sunil S. Bhagwat]

[Prof. Vinay A. Juvekar]

SUPERVISOR

[Prof. Mahesh S. Tirumkudulu]

CHAIRMAN

[Prof. Prasenjit Ghosh]

Date: December 31, 2008

Place: I. I. T. Bombay

Indian Institute of Technology Bombay, India

Certificate of Course Work

This is to certify that **Mr. Karnail B. Singh** was admitted to the candidacy of the Ph.D. degree on July 22, 2003, after successfully completing all the courses required for the Ph. D. Degree Programme. The details of the course work done are given below.

Sr. No.	Course Code	Course Name	Credits	Mode
1	CL 601	Advanced Transport Phenomena	6	Credit
2	CL 701	Computational Methods in Chemical Engineering	8	Credit
3	CL 612	Multiphase Flow Systems	6	Credit
4	CLS 801	Seminar	4	Credit
5	CL 702	Lecture Series	2	Credit
6	HS 699	Communication and Presentation Skills	4	Credit
7	CL 704	Lecture Series	2	Credit
Total Credits			32	

IIT Bombay

Dy. Registrar (Academic)

Date:

ABSTRACT

Understanding the mechanism of film formation in latex dispersions is essential to the success of many industrially important products such as paints, coatings, adhesives, caulks and sealants, photonic band gap crystals, etc. In recent times, the environmental concerns due to emission of large amounts of volatile organic compound (VOC) have forced the paint/coating industry to move away from the traditional organic based formulations towards water based dispersions. Hence the latex, where the dispersing media is water, has become an attractive alternative to the traditional formulations. However, one of the major concerns with water-based dispersions is the problem of cracking. It has been observed that while drying, these aqueous dispersions show an intricate pattern of cracks. Further, not only the paints/coatings but the more classical systems such as ceramics also show this fascinating array of cracks. In the present thesis, we have addressed the issue of cracking in drying dispersions. Also the latex blends that are a potential candidate for zero VOCs formulations have also been investigated.

In the first part of the research work, we have investigated the cracking in drying films of stable colloidal dispersions. Here, based on the magnitude of compressive strain at the maximum attainable capillary pressure, two distinct regimes for obtaining crack free films have been identified. In the first regime, which we call as the *Strain-Limited* regime, the maximum crack free thickness (referred to as *CCT*) decreases with the increase in particle rigidity. In the second regime, which is referred to as the *Stress-Limited* regime, the CCT increases with increase in particle rigidity. A theoretical model for predicting the critical cracking thickness of hard particle systems has been developed. It is shown that the model is universal and can be applied to a wide variety of colloidal

dispersions. Further, the drying in strain-limited regime leads to impermeable films whereas in the stress-limited regime, film formation yields crack free porous films. We have also measured the crack spacing in large number of dispersion and found that the crack spacing agrees well with the general elastic energy based criteria (Griffith's energy balance concept) for crack spacing.

In the next part of the thesis, the cracking phenomenon in flocculated dispersions has been studied. As is well known, the particles form chain like structures in the flocculated dispersions and hence the volume fraction in the final film is generally very low. In this work, the importance of particle packing on film formation has been investigated. Here, the extent of flocculation was controlled by varying the pH of the dispersions. The influence of varying final (dried film) particle volume fraction on critical cracking thickness and critical cracking stress is measured. We show that the experimental measurements for CCT are in good agreement with the model developed for stable dispersions (see chapter 3), suggesting that the model is universal and applies equally well to stable as well as flocculated systems.

In the final part of the research work, we have investigated the film formation in soft-hard latex blends. In these blends the soft particles coalesce to give a continuous matrix where as the undeformed hard particles are embedded in the continuous matrix and provide the mechanical strength to the final film. In this work, the existing model of Routh and Russel⁴⁰ for the stress versus strain relation for monodisperse identical particles in a colloidal film was extended to blends containing a mixture of equal-sized hard and soft elastic spheres while accounting for the non-affine deformation. The model predicts a transition from soft to rigidlike behavior at a critical value of the hard particle

volume fraction that matches well with the simulation results reported in the literature. Further, the experimental measurements on critical cracking thickness and critical cracking stress were used to compare the model predictions. While the predicted trend for the critical stress agrees with the experiments, the variation of the CCT showed differences.

CONTENTS

Thesis Approval Sheet.....	i
Certificate of Course Work.....	ii
Abstract.....	iii
Contents.....	vi
List of Figures.....	x
List of Tables.....	xv
Chapter 1 GENERAL INTRODUCTION.....	1
1.1 Introduction.....	1
1.2 Stages of film formation.....	2
1.2.1 Drying.....	3
1.2.1.1 Drying normal to the surface.....	5
1.2.1.2 Drying laterally in the plane of film.....	6
1.2.2 Deformation of particles.....	8
1.2.2.1 Polymer-air interfacial tension (Dry sintering)	8
1.2.2.2 Solvent-air interfacial tension (Capillary deformation)	9
1.2.2.3 Polymer-solvent interfacial tension (Wet sintering)	10
1.2.2.4 Sheetz deformation (Surface layer)	11
1.2.3 Coalescence and diffusion across particle–particle interface.....	14
1.3 Cracking in drying latex dispersions.....	15
1.4 Motivation for the present work.....	18
1.5 Organization of the thesis.....	19
References.....	21

Chapter 2 EXPERIMENTAL TECHNIQUES.....	29
2.1 Measurements of critical cracking thickness (CCT).....	29
2.2 Measurement of maximum capillary pressure.....	33
2.2.1 Measurement of maximum capillary pressure using a capillary tube.....	33
2.2.2 Measurement of maximum capillary pressure using Dewpoint PotentiaMeter.....	40
2.3 Measurement of stress in drying dispersion.....	43
2.3.1 Calibration and stress measurements.....	46
2.4 Conclusion.....	51
References.....	52
Chapter 3 CRACKING IN DRYING COLLOIDAL FILMS	53
Abstract.....	53
3.1 Introduction.....	53
3.2 Experimental section.....	56
3.3 Results and discussion.....	57
3.4 Concluding remarks.....	63
Acknowledgement.....	63
References.....	65
Chapter 4 CRACKING IN DRYING COLLOIDAL FILMS OF FLOCCULATED DISPERSIONS.....	68
Abstract.....	68

4.1	Introduction.....	69
4.2	Experimental section.....	73
4.3	Results and discussion.....	77
4.4	Conclusion.....	83
	Acknowledgement.....	83
	References.....	84

Chapter 5	FILM FORMATION IN LATEX BLENDS: THEORY AND EXERIMENTS.....	87
	Abstract.....	87
5.1	Introduction.....	88
5.2	Model.....	91
5.2.1	Non-affine deformation.....	95
5.2.2	Orientational average stress-strain relation.....	96
5.3	Experiments.....	100
5.4	Results and discussion.....	101
5.4.1	Comparison with the model.....	103
5.5	Conclusion.....	105
	Acknowledgement.....	105
	References.....	106
	APPENDIX A: CALCULATION OF R_T/R_0 RATIO.....	108
	APPENDIX B: TWO PARTICLE CO-ORDINATE SYSTEM.....	109

Chapter 6 CONCLUSIONS AND RECOMMENDATIONS.....	127
6.1 Summary and conclusions.....	127
6.2 Recommendations for future work.....	128
CONTRIBUTIONS: PATENTS/PUBLICATIONS/CONFERENCES.....	129
AWARDS AND HONORS.....	131
ACKNOWLEDGEMENT.....	132

LIST OF FIGURES

Figure 1.1	Various stages in the process of film formation.....	4
Figure 2.1	Optical micrographs showing the films with and without cracks at different magnifications of 4X, 10X, 20X and 40X respectively. Note that the films were cast from styronal ND 811 (styrene-butadiene random copolymer) dispersion at a temperature of 25.35 ⁰ C and a relative humidity of 52%.....	31
Figure 2.2	A typical thickness profile for an acrylic dispersion film. Note that the region between P and Q was having no cracks.....	32
Figure 2.3	Thickness profile for a flocculated dispersion film dried in an open vial.....	34
Figure 2.4	Experimental measurement of maximum capillary pressure using a capillary tube.....	35
Figure 2.5	Rear meniscus propagation for a dilute dispersion ($\phi_0 = 0.006$) of colloidal silica dispersion. The experiments were conducted at an ambient temperature of 32 \pm 1 ⁰ C and a relative humidity of 50 \pm 1%.....	38
Figure 2.6	Rear meniscus propagation for (a) silica dispersion of $\phi_0 = 0.03$ at an ambient temperature of 25 \pm 1 ⁰ C and a relative humidity of 54 \pm 4% and, (b) styronal ND 811 latex dispersion for $\phi_0 = 0.05$ at an ambient temperature of 34 \pm 1 ⁰ C and a relative humidity of 46 \pm 1%.....	39
Figure 2.7	Schematic of the Dewpoint PotentialMeter used to measure the maximum capillary pressure.....	42

Figure 2.8	Schematic of the experimental set-up used to measure the stress in a drying film.....45
Figure 2.9	Typical weight loss vs. time data for the drying of dispersions used in the present work.....48
Figure 2.10	Calculated evaporation rate by considering the first and last few points..49
Figure 2.11	Technique used to calibrate the set-up.....50
Figure 3.1	Thickness profile of a dried film. (A) Thickness profile measured along the diameter of a dry styrene-butadiene film. (B) SEM of the film surface in the crack free region. (C) SEM of the film interior in the crack free region. The region between S and T was crack free.....58
Figure 3.2	Critical thickness variations as a function of the shear modulus. At random close packing, the menisci at the top particle layer exert a compressive force on the particle network. For very soft particles, the particles deform completely to close the voids for capillary pressure less than the maximum so that the uniaxial compressive strain is, $\varepsilon \equiv \frac{(h_{rcp} - h)}{h_{rcp}} = 1 - \phi_{rcp}$. In case of hard particles, the menisci adjust their curvature till the maximum capillary pressure (P_{max}) is reached, beyond which they recede into the network resulting in partial deformation.....59
Figure 3.3	The measured critical thickness versus the characteristic scale, $\frac{GM\phi_{rcp}R^3}{2\gamma}$. The data points are for films of acrylic (■, $G = 0.8$ GPa, $2R = 82, 133, 206$ and 353 nm, and $\phi_{rcp}(M) = 0.65(6.7), 0.66(6.8), 0.68(7.0)$ and $0.67(6.9)$, respectively), styrene-butadiene (○, $G = 1$ GPa, $2R = 250$ nm,

and $\phi_{rcp}(M) = 0.64(6.6)$, silica (\blacktriangle , $G = 31$ GPa, $2R = 330$ and 22 nm, and $\phi_{rcp}(M) = 0.60(6.1)$ for both), alumina (\bullet , $G = 156$ GPa, $2R = 230, 379, 458$ and 489 nm, and $\phi_{rcp}(M) = 0.60(6.1)$ for all), polystyrene (\star , $G = 1.6$ GPa, $2R = 300$ nm, and $\phi_{rcp}(M) = 0.60(6.1)$), and zirconia [\ast , $G = 81$ GPa, $2R = 200$ nm, and $\phi_{rcp}(M) = 0.60(6.1)$]. Here the value of surface tension, γ , is taken as 0.072 N/m for all the cases. The solid line is a power law with an exponent $\frac{1}{2}$ and the multiplying coefficient is obtained via regression. The inset plots the same data in the non-dimensional form.....61

Figure 3.4 Variations in crack spacing with the film thickness. The data points are for films of alumina⁷ (\blacklozenge , $2R = 13$ nm), PMMA³ (\blacksquare , $2R = 95$ nm), silica⁴ (\blacktriangle , $2R = 20$ nm), styrene-butadiene (\circ , $2R = 250$ nm), acrylic⁸² (\times , $2R = 82$ nm), acrylic¹³³ (\bullet , $2R = 133$ nm), silica³³⁰ ($+$, $2R = 330$ nm)64

Figure 4.1 Schematic of a drying colloidal film of (i) stable and (ii) flocculated dispersion.....72

Figure 4.2 Variation of the final packing volume fraction (ϕ_f) and zeta potential as a function of pH for AKP-30 dispersion (26.1 °C and 43% RH). The zeta potential data is taken from Johnson et al.¹⁶. The solid lines are provided as a guide to the eye.....75

Figure 4.3 Comparison of measured critical cracking thickness (CCT) with the model of Singh and Tirumkudulu¹ at different pH values. Further, the values for ϕ_f and M at different pH values are; [(pH, ϕ_f , M) = (3.97, 0.66, 6.96),

(4.98, 0.61, 6.18), (6, 0.56, 5.12), (7.25, 0.52, 4.90), (9.3, 0.18, 1.03), (10.46, 0.40, 3.82) and (11.88, 0.68, 7.02)] respectively. A contact angle of 35° was assumed.....79

Figure 4.4 Plot of measured dimensionless critical cracking stress ($\sigma_c R/2\gamma$) vs. the dimensionless characteristic scale ($M \phi_f / N^2$). The data points are for films of AKP-30 dispersion with varying pH. The solid line is a power law fit with an exponent of 1/3. The values for ϕ_f and M at different pH are; [(pH, ϕ_f , M)=(3.3, 0.69, 7.2), (6.5, 0.55, 5.23), (7.8, 0.35, 3.3), (10, 0.29, 2.76) and (11.1, 0.58, 5.51)] respectively.....82

Figure 5.1 Particle positions during deformation.....114

Figure 5.2 Scanning electron micrograph of the surface of a blend film with $\alpha = 0.5$ 115

Figure 5.3 Scanning electron micrograph of the cross-section of a blend film with $\alpha = 0.5$ 116

Figure 5.4 Scanning electron micrograph of the cross-section of a blend film with $\alpha = 0.5$, heated at 70°C for about half an hour.....117

Figure 5.5 Scanning electron micrograph of the film-substrate interface of a blend film with $\alpha = 0.5$, heated at 70°C for about half an hour.....118

Figure 5.6 Scanning electron micrograph of the surface of a blend film with $\alpha = 0.95$ 119

Figure 5.7 Dimensionless stress versus dimensionless time, $\bar{t} \equiv \dot{E}t/(h_0(1-\phi_0))$, for various α , where \dot{E} is the evaporation rate, h_0 is the initial average wet

film thickness and ϕ_0 is the initial particle volume fraction. Note that the initial thickness is different in the four cases.....120

Figure 5.8 Variation of effective shear modulus (G_{eff}) with α . Note that the shear moduli for different interactions are $G_{HH} = 31$ GPa, $G_{SS} = 0.8$ GPa and $G_{HS} = 0.8$ GPa.....121

Figure 5.9 Variation of dimensionless critical stress with dimensionless film thickness for a blend of silica and acrylic (BX261) for different hard particle volume fractions.....122

Figure 5.10 Comparison of experimental results with the theoretical predictions for various values of α . Here, E represents experimental measurements while T refers to the theory.....123

Figure 5.11 Comparison of experimental results for CCT with model predictions for different blends.....124

Figure 5.12 Sectional volumes, V_1 and V_2125

Figure 5.13 Calculation of area for the surface element126

LIST OF TABLES

Table 5.1	Details of dispersions used in the present study.....	113
------------------	---	-----

GENERAL INTRODUCTION

Chapter 1

GENERAL INTRODUCTION

1.1 INTRODUCTION

As per the International Union for Pure and Applied Chemistry (IUPAC), Latex is defined as a colloidal dispersion of submicron particles in an aqueous medium. The particles may be organic such as polystyrene, poly(methyl methacrylate), etc. or inorganic such as silica, alumina etc. However, the use of latex is generally associated with organic polymers.¹ There are a variety of applications where latex dispersions are used to produce mechanically coherent films. Some of these include paints, coatings, adhesives, caulks and sealants etc.² In addition to these common products, many other applications such as pressure sensitive adhesives, carpet backing, floor polish, textiles and textile sizing, coatings for drug delivery and sustained/controlled release etc. have also been mentioned in the literature.^{3,4}

Traditionally, the paint/coating formulations have been based on organic solvents. The advantage of using organic solvents is that they plasticize the polymer particles by reducing the particle shear modulus. Consequently the viscous deformation of particles takes place easily and a mechanically strong film can be achieved at ambient conditions.⁵⁻
⁷ Moreover, as the solvents used are generally high boiling, the “open time” for such products is sufficient for their easy applications. The open time is defined as the period

during which an adjacent or subsequent layer can merge homogeneously with the first without altering the dominant physical mechanism for film formation.⁸

Despite the aforementioned advantages, the traditional paints/coatings are being phased out due to environmental and health concerns and replaced by environmental friendly dispersions. Traditional formulations emit large amounts of volatile organic compounds (VOCs) during film formation. Organic solvents, as is well known, reduce air quality and produce the toxic oxidants that pollute the atmosphere. A report by the European Commission reveals that an estimated 17 percent of the total of 10 million tons of “man-made non-methane emissions” of VOCs per year is from the paint and dry cleaning operations. Another report by the Environmental Protection Agency showed that the indoor air pollution is 10 to 40 times higher than the outdoors. This higher rate is due to the emission of VOCs by the paints and coatings.² Due to these concerns, there is a need to replace the conventional organic based paint/coating formulations with environmental friendly dispersions. The fact that latex is water-borne (i.e. the solvent used is water instead of an organic compound) has made it an attractive alternative to the traditional paint and coating formulations. However, the absence of plasticizers means that the particle size and modulus have to be carefully tuned so that they deform and fuse to form a coherent film at ambient temperatures. Hence significant research work has focused on the film formation and cracking in latex dispersions.^{2, 9-11}

1.2 STAGES OF FILM FORMATION

During latex film formation, a stable colloidal dispersion transforms into a continuous polymer film. The entire process of film formation in latex dispersions is

divided into three stages viz. drying, deformation and coalescence.^{2,10,12} Figure 1.1 schematically shows the three stages during the process of film formation in latex dispersions. When a stable colloidal dispersion is applied on to a non-porous substrate, the mass- transfer limited evaporation brings the particles into a close packed structure. During the next stage, van der Waals and capillary forces deform the particles to render a film without voids. Here the particles though deformed, still retain their identity and are still distinguishable. Finally the polymer chains diffuse across the particle-particle interface and hence provide the mechanical strength to the film with particles no more distinguishable.⁸ The three stages of film formation are briefly discussed in the following sections.

1.2.1 Drying

In most latex systems, drying refers to the process of evaporation of water accompanied by the particle ordering. Further, the transport of water between particles is faster than through particles or through a coalesced film. Hence most drying models assume the water loss from the water-gas interface to be dominant than from polymer-gas interface.² The mechanism of water loss from latex dispersions is surprisingly complex and it is still not known as to how the evaporation process affects the structure of the final film.¹³ Several models have considered the drying of film normal to its surface i.e. the transport of water is in the direction normal to the film surface. Also there are models, which consider the drying laterally in the plane of the film. Hence drying of the film has been described as a moving front, both in the normal as well as in the horizontal directions.

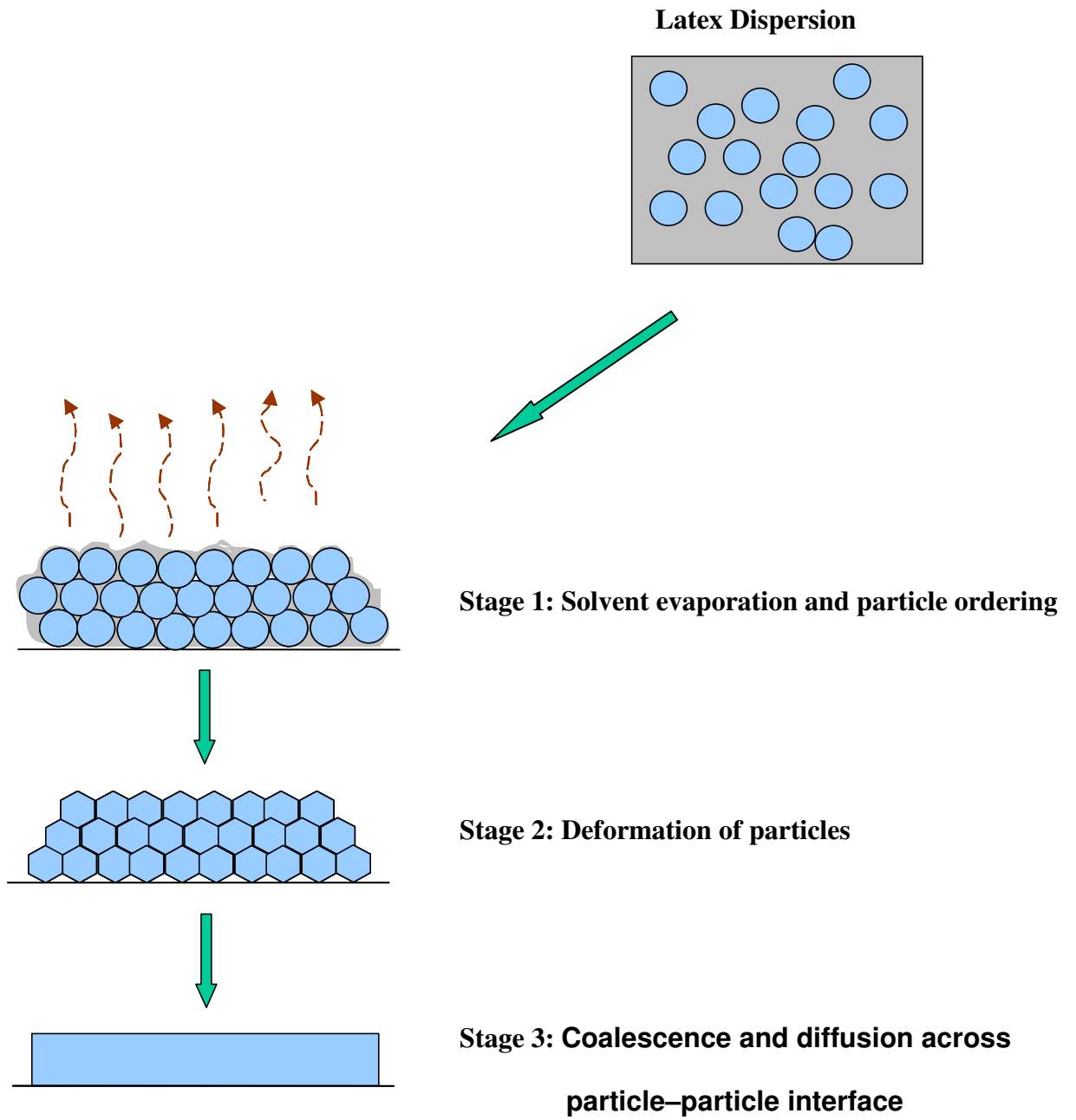


Figure 1.1: Various stages in the process of film formation.

1.2.1.1 Drying normal to the surface

Vanderhoff et al.¹⁴ studied the water loss from latex dispersions using gravimetric techniques. They described the drying as a three-stage process and correlated each of the stages with structural changes occurring during film formation. In the first stage, water evaporates at a constant rate close to that of pure water or latex serum. This stage is observed during the initial period when the dispersion is very dilute such that water can escape freely from water-air interface. In the second stage, the rate of water loss decreases rapidly. This is attributed to the increased region of coalesced film that decreases the total area of air-water interface. The third and final stage is characterized by a diminished rate of water loss that decreases slowly with time. In this stage, water escapes from the film by diffusion through polymers. Here all the channels between particles are almost closed and water has to diffuse through the polymer particles itself. It is found that the asymptotic rate of water loss is indeed similar to the water loss rate, which is observed when water diffuses through continuous polymers.

Unlike Vanderhoff et al.'s three-stage model, Croll¹⁵ has described the drying of latices as a two-stage process. In the first stage, when the dispersion is highly dilute, water evaporates at a constant rate for some time. This rate is equivalent to that of water or latex serum. Moreover for the non-film forming slurries, he observed the constant rate throughout the drying process and supported the concept of a receding drying front. In the second stage, which was described as the falling rate, the transport of water is governed by the diffusion through the dry polymer layer.

Sheetz¹⁶ proposed that there is a dry layer of coalesced particles over a wet layer. Hence water has to diffuse through this dry layer (skin) in order to escape from the wet

film. He made an analogy to a piston in which a coalesced surface layer exerts pressure on the wet layer underneath it. Many others like Eckersley and Rudin¹⁷ and Butt et al.¹⁸ have also observed such a skin over the wet film. Routh and Russel⁸ have shown that the presence or the absence of the packed layer at the top surface is governed by a balance of the particle diffusion and convection induced by the evaporation. A skin is expected to form when convection dominates diffusion.

1.2.1.2 Drying laterally in the plane of film

Experiments have also demonstrated the presence of spatial non-uniformity in drying rates over a latex film. Under such circumstances, the transport of water takes place horizontally in the plane of film. This mode is observed when the non-uniform thickness of the film (thinnest at the edges) causes the particles to concentrate first at the edges. Here the low pressure caused by the liquid menisci at the edge draws the dispersion from the bulk towards the edges. This results in the lateral propagation of the front, in a direction opposite to the water flux.¹⁹ Further, for film forming lattices, three different regions with a central wet region that is turbid, a peripheral dry region that is optically clear and a region between these two that is partly cloudy are observed.^{19,20} Water evaporates more rapidly from this middle region than from the water surface above the wet region. This creates a flux of water and particles from the central wet region to the edge consequently resulting in the propagations of fronts from the edge towards the center.^{19,21,22}

In a review by Holl et al.²³, various aspects of drying during film formation have been discussed in detail. Here, they have distinguished three primary modes of drying in a wet film. In the first mode, water concentration remains uniform over the entire surface

of the film and hence all the parts of the film dry at the same rate. This mode is called as homogeneous drying and is rarely observed. The second mode of drying occurs under conditions of negligible particle diffusivity. Here the evaporating liquid concentrates the particles at the liquid-air interface resulting in a sheet of packed particles at the surface of film. As particle diffusivity back to the wet dispersion is very small, the thickness of the sheet increases as the vertical convection induced by the negative capillary draws more particles from the bulk. Note that here the capillary pressure is caused by the liquid menisci between the particles at air-film interface. Finally the third mode is observed when the non-uniform thickness of the film causes the flow of water from center toward the edges. Here, in contrast to the previous case, the low pressure caused by the liquid menisci at the edge draws water laterally from the bulk and deposits particles at the front.

Routh and Russel^{8,24} have developed a theory based on the lubrication approximation that can capture the drying fronts while ignoring particle deformation. Depending on the Peclet number (Pe), defined as the ratio of rate of evaporation to the rate of diffusion, they could differentiate the way drying would proceed either as a drying front in the horizontal direction or as a compaction front in the vertical direction. For the case when Peclet number approaches zero ($Pe \ll 1$), particles distribute uniformly in the vertical direction and drying proceeds as a moving front in the horizontal direction. On the other hand, for the case when Peclet number is much higher than unity ($Pe \gg 1$), particles distribute non-uniformly in the vertical direction with a layer of particles formed at the surface of the film that further grows with time (moving front in the vertical direction).

1.2.2 Deformation of particles

During the second stage of film formation, polymer particles are deformed by strong forces so as to produce a structure without voids. For the last few decades, a number of theoretical and experimental studies have looked at the compaction or deformation step. Possible causes of particle deformation include air-water, water-polymer or polymer-air interfacial tensions, osmotic forces or surface adhesive forces.² It is still unclear that whether the forces arise from either one or a combination of polymer-air (dry sintering), polymer-water (wet sintering) and solvent-air (capillary compaction) interfacial tensions. All of the above interfacial tensions are reported as being the driving forces behind particle deformation. The following sections discuss briefly the various driving forces for particle deformation.

1.2.2.1 Polymer-air interfacial tension (Dry sintering)

Dillon et al.²⁵ proposed that the driving force for particle deformation is the interfacial tension between polymer and surrounding air. As per their theory, latex dries before particles lose their shape on deformation. They employed Frenkel's theory of sintering to describe the viscous deformation of latex particles. In their work, the sintering of poly(vinyl chloride-co-vinylidene chloride) (P(VC-VdC)) and P(S) particles was observed on a colloidal film. It was found that the results were in good agreement with the Frenkel's model. Chainey et al.²⁶ have also presented evidence for polymer-air interfacial tension as being the driving force for particle deformation. In this work, the flash cast films that were initially rough, smoothed out on ageing after a period of one month. Because there was no water present in these samples, the cause of deformation is presumably by the polymer-air interfacial tension. The work of Sperry et al.²⁷ suggests a

strong evidence of polymer-air interfacial tension being the driving force for particle deformation. They studied the particle deformation step by minimum film formation temperature (MFT) measurements for several types of polymers. It was concluded that the presence of water does not play any significant role in the particle deformation. They argued that the film formation process can be separated into two independent steps. In the first, water evaporates completely and in the next, particles are deformed due to polymer-air interfacial tension and van der Waals forces. Keddie et al.^{28,29} have also supported the concept of polymer-air interfacial tension as being the driving force for particle deformation.

1.2.2.2 Solvent-air interfacial tension (Capillary deformation)

Brown³⁰ was the first to suggest that **the air-water interfacial tension** plays an important role in film formation. He observed that evaporative drying of latex finishes at the same time as film formation, suggesting that evaporation of water and deformation are concurrent phenomena. It was further observed that if the evaporation is slowed or delayed, the film formation is also affected in the similar manner. This phenomenon was attributed to the dual effects of **plasticization by water and a strong capillary force**. The other important observation was that even the lightly crosslinked emulsion polymers can form homogeneous films. As purely viscous flow is impossible in such systems, he concluded that the viscous flow of polymers, as described by Dillon et al.²⁵, cannot be the mechanism for film formation. He on the other hand considered the polymeric particles as being elastic bodies. As per Brown theory, the condition for film formation is

$$G(t) < \frac{35\gamma_{WA}}{R} \quad (1.1)$$

Here ' γ_{WA} ' is the interfacial tension between water and air and ' $G(t)$ ' is the shear modulus measured by examining the strain resulting from the application of stress for time ' t '.

Eckersley and Rudin³¹ suggested that the capillary force is not the only force that is responsible for particle deformation. They argued that in addition to the capillary force, either the polymer-water or the polymer-air interfacial tension is also responsible for particle deformation. As per their model, deformation is a two-stage process. In the first stage, capillary force deformed the particles whereas in the next stage, depending on whether or not water is present, polymer-water or polymer-air interfacial tension complete the deformation. Dobler et al.³² have also forwarded the similar view of an additional force causing the deformation of particles. Lin and Meier^{33,34} have strongly recommended the capillary force as the dominant driving force for film formation. In their work, it was shown that the role of water is not to plasticize the polymer particles but to generate a strong capillary force. Hence capillary force is indeed a dominating force for particle deformation. A recent study by Tirumkudulu and Russel¹⁹ has also led to a similar conclusion of capillary force as the one responsible for particle deformation.

1.2.2.3 Polymer-solvent interfacial tension (Wet sintering)

In the wet sintering regime, the driving force for particle deformation is the interfacial tension between polymer and solvent or latex serum. Vanderhoff et al.³⁵ developed the concept of polymer-water interfacial tension as the driving force for particle deformation. They observed that film formation does not show strong dependence on particle size as is predicted by Brown's theory and also by the dry sintering models. Hence they concluded that the only possible force can be the interfacial

tension between polymer and solvent. They developed a model in which water-air interfacial tension (i.e. the capillary force) first forces the particles into close contacts. This force overcomes the double layer repulsion of the particles and when the polymer particles start contacting each other, the polymer-water interfacial tension becomes operative.

Sheetz¹⁶ experimentally showed the polymer-water interfacial tension as the driving force for particle deformation. A more extensive experimental study of wet sintering was carried out by Dobler et al.³⁶ In their work, it was confirmed that particle-water interfacial tension was indeed able to cause the particle deformation, even at temperatures below the glass transition temperature of the polymer.

1.2.2.4 Sheetz deformation (Surface layer)

In contrast to the previous mentioned models for particle deformation, Sheetz¹⁶ accounted for the inhomogeneous drying of the film. As per Sheetz theory, the capillary force causes some initial deformation of latex particles in such a way that a continuous polymeric film is formed on the surface of the drying latex. This skin is permeable to water and hence water continues to diffuse through this layer. As per this model, the energy for film formation is supplied as heat from the surroundings. This heat is converted to useful (film-forming) work by evaporation of water. **As water diffuses through the top layer, it exerts a compressive force normal to the film surface.** He made an analogy to a piston compressing the wet dispersion. This piston is however permeable to water. **The particle packing is compressed by this force thus leading to particle deformation.** Dobler et al.³⁶ have also supported the Sheetz view of film formation.

All the above discussed film formation regimes were based on the nature of force causing the deformation. In addition to this, there are models that are based on particle rheology. These models relate the amount of deformation to the external force through particle rheology. In the earliest model proposed by Hertz, the two spheres are considered as elastic bodies.³⁷ The amount of deformation, which is caused when the spheres are pushed together by external point force (F) acting along the line joining their centers, is given by

$$\varepsilon_R = \left(\frac{3}{16} \right)^{\frac{2}{3}} \left(\frac{F}{GR_0^2} \right)^{\frac{2}{3}} \quad (1.2)$$

Where ‘G’ is the shear modulus and ‘R₀’ the original radius of particle. Here ε_R is the local strain and is defined as the ratio of change in the center-to-center distance with the original distance before deformation.

In the model by Frenkel³⁸, the particles are treated as viscous drops. Further, a balance between the interfacial tension ‘ γ_{PA} ’ which minimizes the particle surface area with the viscous force resisting deformation gives a simple relation between particle viscosity and local strain as

$$\varepsilon_R = \frac{3\gamma_{PA}t}{4\pi\eta_p R_0} \quad (1.3)$$

Here, ‘ η_p ’ is the viscosity of polymer, ‘t’ is the time over which the strain is applied, and ‘R₀’ the radius of particle. Johnson et al.³⁹ also considered the spheres as elastic bodies and proposed a theory, which is commonly known as JKR theory. In their model, a balance between stored elastic energy in the deformed material, lost surface energy

caused by fusion of two spheres and the energy of an applied load is made. This balance leads to the following relation for the local strain

$$\varepsilon_R = 0.234 \left(\frac{\gamma_{PA}}{GR_0} \right)^{\frac{2}{3}} \quad (1.4)$$

In contrast to the above models, which consider the particles either viscous or perfect elastic bodies, Routh and Russel^{40,41} (henceforth referred to as RR) have considered the particles as being viscoelastic. They found the deformation of a pair of particles due to both interfacial tension and external forces exerted by contacting neighbors. Starting from a microscopic description of the local stress versus strain relation, they volume averaged over all possible orientations of the pair to arrive at a macroscopic description of stress and strain relation for a deforming film. In this model, a balance between the viscous deformation rate and evaporation rate led to a single dimensionless group ‘ λ ’. For typical evaporation rates, this dimensionless group can distinguish between the various regimes of film formation. While very low values of ‘ λ ’ lead to wet sintering, a large value signifies dry sintering. Intermediate values coupled with homogeneous drying lead to capillary compression. But in the case when vertical front is present, intermediate values of ‘ λ ’ result in Sheetz deformation. It was found that the model predictions were in good agreement with experimental results.^{8,24,40,41} Thus they provided a theoretical framework that was able to explain many of the experimental results on film formation reported in literature.

1.2.3 Coalescence and diffusion across particle–particle interface

Coalescence is a term used to describe the fusion of two particles with the elimination of boundary between them. The driving force for coalescence is the reduction in surface energy associated with the particles surfaces. The deformed particles during second stage finally coalesce with one-another. Here, the polymer chains diffuse from one globule to another and hence result in a homogeneous and continuous film. Voyutskii⁴² argued that mere physical contact between particles cannot produce a strong and continuous film. To obtain a stable film, it is necessary that polymer molecules must diffuse from one globule to another, thus forming a stable link.⁴³ With the development of new techniques of neutron scattering and non-radiative energy transfer, it is now possible to show that the interdiffusion between particles does indeed occur. Hahn et al.⁴⁴ employed SANS to observe the interdiffusion between particles of hydrogenated and deuterated acrylic latex. They obtained the diffusion coefficients in the range of 10^{-20} at 90°C . Sperling et al.⁴⁵ also studied the film formation from polystyrene latexes using SANS. They found that full mechanical strength in the films is achieved when the diffusion length is comparable to the radius of gyration of the latex polymers.⁴⁶⁻⁴⁸ The technique of non-radiative energy transfer (ET) has also been employed to study the interdiffusion of polymer chains.⁴⁹ This technique monitors concentration profiles of donor and acceptor chromophores that are initially isolated in separate particles. As interdiffusion occurs, mixing of donor and acceptor groups can be measure by an increase in energy transfer between them. Hence, it is now well accepted that the diffusion of polymer chains across the particle-particle boundary is essential for mechanical strength of the final film.

1.3 CRACKING IN DRYING LATEX DISPERSIONS

As discussed above, during the second stage of film formation, polymer particles are deformed by forces so as to produce a film without voids. However, depending on the particle glass transition temperature (T_g) and ambient temperature, the final film may be a homogeneous one or may contain large number of cracks in it. It has been observed that if the particle glass transition temperature (T_g) is higher than the ambient temperature, the final film generally contains large number of cracks in it. Also for dispersions containing inorganic polymer particles (hard particles) such as alumina, silica, etc., the phenomena of cracking can be observed very commonly.

The problem of cracking during drying of wet films has received the attention of scientific community in the last couple of decades. Chiu et al.^{50,51} have studied the cracking during drying of wet ceramic films prepared from α -alumina particles of 200 and 400 nm diameters. In this study they showed that irrespective of the particle size and rigidity, all films cracked only above a critical thickness. Further, the critical thickness depends on the particle size and was found to increase with increase in particle diameter. Also, the films cast on a pool of mercury resulted in much higher critical thickness indicating that the tensile stress induced during drying is influenced by the nature of the underlying substrate. In a recent work, Tirumkudulu and Russel^{19,52} have also reported the phenomena of cracking in drying latex films. These films were cast from aqueous dispersions containing polymer spheres of diameters ranging from 95 to 610 nm. They solved the RR model while accounting for the lateral drying front and compared the predicted stress and front propagation with the measured values for dispersions in the capillary deformation regime. By measuring the stresses generated during film formation,

they showed that the tensile stresses in the plane of the film responsible for the bending of the cantilever arises from the same capillary pressure that drives particle compaction in the normal direction. Finally, based on the Griffith's energy balance concept, a model that can predict the critical thickness beyond which a given film would crack was also developed. Allain and Limat⁵³ studied the cracking of a colloidal suspension during one directional drying. Here, a colloidal silica suspension of particle size 9 nm was allowed to dry from one end of a thin parallelepiped cell whose thickness was varied from 15 to 100 μ m. They found that the cracks started at the free surface and then penetrated into the sample as evaporation continued. The variation in crack spacing was measured with the sample thickness. It was found that the crack spacing increases almost linearly with the thickness of the sample. In another study, Lee and Routh⁵⁴ proposed a new scaling for the crack spacing and showed that the hydrodynamics of the systems sets the spacing between the cracks. In their study, experiments were performed in a petri dish where cracks were observed at the free surface of the film. In this study, it was proposed that once the cracks nucleate due to high negative capillary pressure, the capillary pressure becomes negligible in the vicinity of the crack that sets the flow of the solvent toward the bulk where pressure is still lower than the atmospheric pressure. It was found that the distance over which solvent flows in order to relax the capillary pressure gives the spacing between the cracks.

Dufresne et al.^{55,56} have reported the dynamics of fracture in drying nanoparticle suspensions. In this work, a comprehensive physical picture of the fluid to solid transition induced by drying was presented. They showed that the dynamics of drying are determined by a blend of capillary and viscous forces, regulated by the nanometer-scale

texture of the air-water interface. It was further shown that the crack growth is controlled by a balance of elastic energy, surface energy and the viscous dissipation due to interstitial fluid flow. In a recent study, Man and Russel⁵⁷ have also shown that the cracking is controlled by the elastic energy recovery, though the energy criterion is shown to give the lower bound for cracking. Russel et al.⁵⁸ have recently proposed a generalized model based on Hertzian contact mechanics for the deformation and cracking of colloidal packing of spheres saturated with water. They identified the different regimes of film formation similar to Routh and Russel^{40,41} but with a more generalized constitutive equation. Ambient conditions are also found to affect the way cracks form and grow. In an experimental study by Lecocq and Vandewalle⁵⁹ it was found that drying rate has a strong effect on the crack nucleation and growth with fast drying favoring a large number of small cracks while a slow drying gives a small number of larger cracks.

One of the new promising solutions to the traditional organic formulations is the use of latex blends containing soft (low T_g) and hard (high T_g) polymer particles. In these blends, soft particles coalesce to fill the voids and the hard ones give mechanical strength to the final film. The film formation and the properties of these systems are strongly dependant on the composition of the blend. In a study by Winnik and Feng⁶⁰, it was found that the average evaporation rate for latex blends is lower compared to that for dispersions containing either of the pure components (hard or soft particles) with the minimum evaporation rate occurring close to a volume fraction ratio of 0.50 (i.e. ratio of hard particle volume to the total particle volume). In another study, Martinez and Lewis⁶¹ showed that the addition of hard particles to a dispersion containing soft particles has a profound influence on the densification behavior of the film. They measured the stress

induced in a drying film prepared from latex blends containing varying relative volume fractions of hard and soft particles. Interestingly, the maximum stress increased with increasing amounts of hard particles and peaked when the ratio of hard particle volume to the total particle volume was 0.58. On increasing the hard particle content further, the peak stress decreased initially and then finally increased to attain the maximum stress value for the dispersions containing only hard particles. These experiments clearly show that the mixtures of hard and soft particles can lead to rather unexpected drying and film formation. On theoretical front, the densification of binary mixtures of particles of different moduli has also been studied using both continuum models as well as discrete numerical methods.^{62,63} The former performs well for dilute concentrations of hard particles but fails to capture the sintering behavior at high relative volume fractions of hard particles. On the other hand, the latter provides information about particle deformation in the packing over the full range of relative volume fractions. Here, the model replaces a packing of particles by a network of points (representing particle centers) and links that connect these points (representing contacts between particles). The mechanics of sintering and deformation of the packing are then analyzed by studying the deformation of this network.

1.4 MOTIVATION FOR THE PRESENT WORK

Despite the fact that film formation in water-based dispersions has been studied for several decades, the overall understanding of the process is still not very clear. Further, the mechanisms responsible for drying and deformation are rather complex and are not understood completely. The most important and outstanding issue is the origin of

compressive forces that deform the particles. Due to the complex mechanism of the process, film formation is still an active area of research. Many new studies are continuously being reported with the advent of modern instrumentation techniques of spectroscopy, electron microscopy, atomic force microscopy, etc.⁶⁴⁻⁶⁸ Further, as discussed before, one of the more interesting and challenging problems associated with aqueous dispersions is the cracking during drying of the films. The stresses generated during second stage of film formation are released either by the viscous flow of the particles, which happens for the case of soft particles, or by the nucleation and propagation of cracks, which is observed in case of hard particles. Though the issue of cracking in surface coatings was reported long back⁶⁹, it is only recently that this problem is being tackled actively due to its importance in many applications such as latex dispersions, ceramic films, etc. where obtaining a crack free film is the primary concern. Further, from a fundamental point of view, it is important to understand why aqueous dispersions including mud slurries crack during drying. Also, in case of binary mixtures of soft-hard particles, the film formation is rather complex and hence poses new challenges in understanding the process. The lack of understanding of cracking mechanism and the absence of a theoretical framework for latex blends motivated us to carry out the work presented in this thesis.

1.5 ORGANIZATION OF THE THESIS

The work presented in this thesis is organized into six chapters describing the research methodology and results, followed by conclusions and recommendation for future work. In chapter 1, the overview of film formation in latex dispersions is presented

briefly. Chapter 2 describes the various experimental techniques/methods used in the present work. Here in addition to the standard techniques, some of the methods developed to measure the maximum capillary pressure and stresses in drying dispersions have been described. Further, chapter 3 deals with cracking in drying colloidal films of stable dispersions. Here, a comprehensive study on critical cracking thickness of stable aqueous dispersions has been presented. In chapter 4, the cracking behavior of flocculated dispersions over the entire range of pH values is described. It is shown that the theory developed for stable dispersions is also capable of describing the cracking phenomena in flocculated dispersions. The focus of chapter 5 is on the film formation mechanism in latex blends. Here, a mathematical model for film formation in soft-hard latex blends is developed and validated with extensive experimental data. Chapters 3-5 are written in the form of separate papers. Hence the relevant literature and the conclusions are presented at the end of each chapter. Finally, the overall conclusions and directions for future work are presented in chapter 6.

REFERENCE

- [1] D. Urban and K. Takamura. Polymer dispersions and their industrial applications. *Wiley-VCH*, 2002.
- [2] J. L. Keddie. Film formation of latex. *Materl. Sci.Eng.*, 21: 101-170, 1997.
- [3] V. Granier and A. Sarte. Ordering and adhesion of latex particles on model inorganic surfaces. *Langmuir*, 11: 2179-2196, 1995.
- [4] F. Dobler, T. Pith, M. Lambla, and Y. Holl. Coalescence Mechanisms of Polymer Colloids I. Coalescence under the Influence of Particle-Water Interfacial Tension. *J. Colloid Interface Sci.*, 152 (1): 1-11, 1992.
- [5] D. Juhue and J. Lang. Film formation from dispersion of core-shell latex particles. *Macromolecules*, 28: 1306-1308, 1995.
- [6] E. Arda, S. Kara, A. Sarac, and O. Pekcan. Vapor-induced film formation from low-*T_g* particles for different solvent compositions. *J. Colloid Interface Sci.*, 297: 520-524, 2005.
- [7] Y. Wang and M. A. Winnik. Effect of coalescing aid on polymer diffusion in latex films. *Macromolecules*, 23 (21): 4731- 4732, 1990.
- [8] A. F. Routh and W. B. Russel. Deformation mechanism during latex film formation: Experimental evidences. *Ind. Eng. Chem. Res.*, 40: 4302-4308, 2001.
- [9] P. A. Steward, J. Hearn, and M. C. Wilkinson. An overview of polymer latex film formation and properties. *Adv. in Colloid and Interface Sci.*, 86: 195-267, 2000.
- [10] M. A. Winnik. Latex film formation. *Curr. Opin. Colloid Interface Sci.*, 2 (2): 192-199, 1997.

- [11] M. Visschers, J. Laven, and A. L. German. Current understanding of the deformation of latex particles during film formation. *Prog. Org. Coat.*, 30: 39-49, 1997.
- [12] F. Dobler and Y. Holl. Mechanism of latex film formation. *Trend. Poly. Sci.*, 4(5): 145-150, 1996.
- [13] Y. Reyes and Y. Duda. Modeling of drying in films of colloidal particles. *Langmuir*, 21: 7057-7060, 2005.
- [14] J. W. Vanderhoff, E. B. Bradford, and W. K. Carrington. The transport of water through latex films. *J. Polym. Sci.: Symposium No.* 41: 155-174, 1973.
- [15] S. G. Croll. Drying of latex paint. *J. Coat. Technol.*, 58 (734): 41-49, 1986.
- [16] D. P. Sheetz. Formation of films by drying of latex. *J. Appl. Polym. Sci.*, 9: 3759-3773, 1965.
- [17] S. T. Eckersley and A. Rudin. Drying behaviour of acrylic latexes. *Prog. Org. Coat.*, 23: 387-402, 1994.
- [18] H. J. Butt, R. Kuropka, and B. Christensen. Latex film formation studied with the atomic force microscopy: influence of aging and annealing. *Colloid Polym. Sci.*, 272: 1218-1223, 1994.
- [19] M. S. Tirumkudulu and W. B. Russel. Role of capillary stresses in film formation. *Langmuir*, 20 (7): 2947-2961, 2004.
- [20] J. C. H. Hwa. Mechanism of film formation from latices: Phenomenon of flocculation, *J. Polym. Sci.*, A 2: 785-796, 1964.

- [21] N. D. Denkov, O. D. Velev, P. A. Kralchevsky, I. B. Ivanov, H. Yoshimura, and K. Nagayama. Mechanism of formation of two-dimensional crystals from latex particles on substrate. *Langmuir*, 8: 3183-3190, 1992.
- [22] E. Sutanto, Y. Ma, H. T. Davis, and L. E. Scriven. Film formation in coatings: Mechanisms, properties and morphology. *ACS symposium series 790, Provder, T. and Urban, M. W., Eds. ACS*, 174-192, 2001.
- [23] Y. Holl, J. L. Keddie, P. J. McDonald, and W. A. Winnik. Film formation in coatings: Mechanisms, properties and morphology. *ACS symposium series 790, Provder, T. and Urban, M. W., Eds. ACS*, 2-26, 2001.
- [24] A. F. Routh and W. B. Russel. Horizontal drying fronts during solvent evaporation from latex films. *AIChE*, 44 (9): 2088-2098, 1998.
- [25] R. E. Dillon, L. A. Matheson, and E. B. Bradford. Sintering of synthetic latex particles. *J. Colloid Sci.*, 6(2): 108-117, 1951.
- [26] M. Chainey, M. C. Wilkinson, and J. Hearn. Preparation of polymer latex films by a flash casting technique, *J. Appl. Polym. Sci.*, 30: 4273-4285, 1985.
- [27] P. R. Sperry, B. S. Snyder, M. L. O'Dowd, and P. M. Lesko. Role of water in particle deformation and compaction in latex film formation. *Langmuir*, 10: 2619-2628, 1994.
- [28] J. L. Keddie, P. Meredith, R. A. L. Jones, and A. M. Donald. Kinetics of film formation in acrylic latices studied with multiple-angle-of-incidence ellipsometry and environmental SEM. *Macromolecules*, 28: 2673-2682, 1995.

- [29] J. L. Keddie, P. Meredith, R. A. L. Jones, and A. M. Donald. Film formation in waterborne coatings. *ACS symposium series 648, Provder, T., Winnik, M. A. and Urban, M. W., Eds. ACS, 332, 1996.*
- [30] G. L. Brown. Formation of films from polymer dispersions. *J. Polym. Sci., 22: 423-434, 1956.*
- [31] S. T. Eckersley and A. Rudin. Mechanism of film formation from latexes. *J. Coat. Technol., 62 (780): 89-100, 1990.*
- [32] F. Dobler, T. Pith, M. Lambla, and Y. Holl. Coalescence mechanism of polymer colloids ii Coalescence with evaporation of water. *J. Colloid Interface Sci., 152 (1): 12-21, 1992.*
- [33] F. Lin and D. J. Meier. A study of latex film formation by atomic force microscopy. I. A comparison of wet and dry conditions. *Langmuir, 11: 2726-2733, 1995.*
- [34] F. Lin and D. J. Meier. Latex film formation: atomic force microscopy and theoretical results. *Prog. Org. Coat., 29: 139-146, 1996.*
- [35] J. W. Vanderhoff, H. L. Tarkowski, M. C. Jenkins, and E. B. Bradford. Theoretical consideration of the interfacial forces involved in coalescence of latex particles, *J. Macromol. Chem., 1 (2): 361-397, 1966.*
- [36] F. Dobler, T. Pith, M. Lambla, and Y. Holl. Coalescence mechanisms of polymer colloids. *J. Colloid Interface Sci., 152, 1-21, 1992.*
- [37] D. Maugis. Contact, Adhesion and Rupture of Elastic Solids, *Springer, 1999.*
- [38] J. Frenkel. Viscous flow of crystalline bodies under the action of surface tension. *J. Phys., 9 (5): 385-391, 1945.*

- [39] K. L. Johnson, K. Kendall, and A. D. Roberts. Surface energy and the contact of elastic solids. *Proc. R. Soc. Lond. A.*, 324: 301-313, 1971.
- [40] A. F. Routh and W. B. Russel. A process model for latex film formation: Limiting regimes for individual driving forces. *Langmuir*, 15 (22): 7762-7773, 1999.
- [41] A. F. Routh and W. B. Russel. A process model for latex film formation: Limiting regimes for individual driving forces. *Langmuir*, 17 (23): 7446-7447, 1999.
- [42] S. S. Voyutskii. Amendment to the papers by Bradford, Brown, and co-workers: Concerning mechanism of film formation from high-polymer dispersions. *J. Polym. Sci.*, 32: 528-530, 1958.
- [43] S. S. Voyutskii. Autohesion and adhesion of high polymers. *New York: Interscience*, 1963.
- [44] K. Hahn, G. Ley, H. Schuller, and R. Oberthur. On particle coalescence in latex films, *Colloid Polym. Sci.*, 264: 1082-1096, 1986.
- [45] L. H. Sperling, A. Klein, K. D. Kim, and G. D. Wignall. Characterization of film formation from direct mini-emulsified polystyrene latex particles via SANS. *Macromolecules*, 26: 4624-4631, 1993a.
- [46] L. H. Sperling, A. Klein, and N. Mohammadi. Polymer chain rupture and the fracture behavior of glassy polystyrene. *Macromolecules*, 26: 1019-1026, 1993b.
- [47] K. D. Kim, L. H. Sperling, A. Klein, and B. Hammouda. Reptation time, temperature, and cosurfactant effects on the molecular interdiffusion rate during polystyrene latex film formation. *Macromolecules*, 27: 6841-6850, 1994.

- [48] M. Sambasivam, A. Klein, and L. H. Sperling. Energy-consuming micromechanisms in the fracture of glassy polymers. 2: Effect of molecular weight on the fracture of polystyrene. *Macromolecules*, 28: 152-159, 1995.
- [49] C. L. Zhao, Y. Wang, Z. Hruska, and M. A. Winnik. Molecular aspects of latex film formation. An energy transfer study. *Macromolecules*, 23: 4082-4087, 1990.
- [50] R. C. Chiu and M. J. Cima. Drying of granular ceramic films: II Drying stress and saturation uniformity. *J. Am. Ceram. Soc.*, 76(11): 2769-2777, 1993a.
- [51] R. C. Chiu, T. J. Garino, and M. J. Cima. Drying of granular ceramic films: I Effect of processing variables on cracking behavior. *J. Am. Ceram. Soc.*, 76(9): 2257-2264, 1993b.
- [52] M. S. Tirumkudulu and W. B Russel. Cracking in drying latex films. *Langmuir*, 21 (11): 4938-4948, 2005.
- [53] C. Allain and L. Limat. Regular patterns of cracks formed by directional drying of a colloidal suspension. *Phys. Rev. Lett.* 74(15): 2981-2984, 1995.
- [54] W. P. Lee and A. F. Routh. Why do drying films crack? *Langmuir*, 20(23): 9885-9888, 2004.
- [55] E. R. Dufresne, E. I. Corwin, N. A. Greenblatt, J. Ashmore, D. Y. Wang, A. D. Dinsmore, J. X. Cheng, X. S. Xie, J.W. Hutchinson, and D. A. Weitz. Flow and fracture in drying nanoparticle suspensions. *Phys. Rev. Lett.* 91 (22): (4501-1)-(4501-4), 2003.
- [56] E. R. Dufresne, D. J. Stark, N. A. Greenblatt, J. W. Cheng, J.W. Hutchinson, L. Mahadevan, and D. A. Weitz. Dynamics of fracture in drying suspensions. *Langmuir*, 22: 7144-7147, 2006.

- [57] W. Man and W. B. Russel. Direct measurements of critical stresses and cracking in thin films of colloid dispersions. *Phys. Rev. Lett.*, 100: 198302(1)- 198302(4), 2007.
- [58] W. B. Russel, N. Wu, and W. Man. Generalized Hertzian model for the deformation and cracking of colloidal packings saturated with water. *Langmuir*, 24: 172-1730, 2008.
- [59] N. Lecocq and N. Vandewalle. Experimental study of cracking induced by desiccation in 1-dimensional systems. *Eur. Phys. J. E.*, 8: 445-452, 2002.
- [60] M. A. Winnik and J. Feng. Latex blends: An approach to zero VOC coatings. *J. Coat. Technol.*, 68 (852): 39-50, 1996.
- [61] C. J. Martinez and J. A. Lewis. Shape evolution and stress development during latex-silica film formation. *Langmuir*, 18: 4689-4698, 2002.
- [62] A. Jagota and G. W. Scherer. Viscosities and sintering rates of a two-dimensional granular composite. *J. Am. Ceram. Soc.*, 76(12): 3123-3135, 1993.
- [63] A. Jagota and G. W. Scherer. Viscosities and sintering rates of composite packings of spheres. *J. Am. Ceram. Soc.*, 78(3): 521-528, 1995.
- [64] J. Rottstegge, B. Traub, M. Wilhelm, K. Landfester, C. Heldmann, and H. W. Spiess. Investigations on the Film-Formation Process of Latex Dispersions by Solid-State NMR Spectroscopy. *Macromol. Chem. Phys.*, 204: 787-802, 2003.
- [65] I. Ludwig, W. Schabel, M. Kind, J. C. Castaing, and P. Ferlin. Drying and film formation of industrial waterborne latices. *AIChE*, 53 (3): 549-560, 2006.
- [66] S. Schantz, H. T. Carlsson, T. Andersson, S. Erkselius, A. Larsson, and O. J. Karlsson. Poly(methyl methacrylate-co-ethyl acrylate) latex particles with

- poly(ethylene glycol) grafts: Structure and film formation. *Langmuir*, 23 (7): 3590-3602, 2007.
- [67] Y. Reyes, T. J. Campos, F. Vazquez, and Y. Duda. Properties of films obtained from aqueous polymer dispersions: study of drying rate and particle polydispersity effects. *Modelling Simul. Mater. Sci. Eng.*, 15: 355–368, 2007.
- [68] K. I. Dragnevski and A. M. Donald. An environmental scanning electron microscopy examination of the film formation mechanism of novel acrylic latex. *Colloid Surf. A: Physicochem. Eng. Aspect*, 317: 551–556, 2008.
- [69] J. C. Grosskreutz and M. B. McNeil. The fracture of surface coatings on a strained substrate. *J. Appl. Phys.*, 40 (1): 355-359, 1969.

EXPERIMENTAL TECHNIQUES

Chapter 2

EXPERIMENTAL TECHNIQUES

In this chapter, the experimental techniques/methods used to measure the critical cracking thickness, maximum capillary pressure in a drying dispersion and the critical stress at which a film cracks are discussed in detail. The various techniques/methods are discussed in the following sections.

2.1. MEASUREMENTS OF CRITICAL CRACKING THICKNESS (CCT)

Thin circular films of aqueous dispersions were cast uniformly on glass substrates using a spin coater. Prior to the start of experiments, the glass substrates were cleaned thoroughly with de-ionized water to remove impurities from the surface. Note that unlike pure liquids, concentrated dispersions can be difficult to spread on solid substrates. Hence, once the dispersion drop is put on the glass substrate, the contact line is pinned and it becomes difficult to spread the dispersion over desired area so as to control the thickness of the dried film. To overcome this difficulty, a spin coater was used at low rpm (~100 rpm). Here, the dispersion was discharged using a micropipette on the rotating glass substrate and the tip of the micropipette was used to gently push the contact line so as to spread the film over the designated area. The rotation of the substrate ensured that the film occupied a circular area. The thickness of the film was varied by controlling the

amount of dispersion dispersed on to the substrate. Hence, using a spin coater, we can cast circular films of desired thickness. After the film dried completely, it was examined for cracks under an upright optical microscope (Olympus, BX-60) at varying magnifications (4X, 10X and 20X). Most films exhibited cracks at the rim and close to the centre with the remaining area devoid of cracks. Further, the crack-free region increased in area with decreasing average film thickness. Note that in some of the cases, we were able to get completely crack free films. Figure 2.1 shows some optical images of a crack free and a cracked film. In case of flocculated dispersions (discussed in chapter 4), the critical cracking thickness of some of the dispersions was very high. Hence it was not possible to cast the film using spin coater technique, as the required amount was more than the maximum supportable amount over that area. Therefore for these dispersions, the films were dried in open vials of rectangular cross section with dimension, 13 (length) x 13 (breadth) x 6 (height) mm³.

The thickness profile of the dried film was measured using a surface profilometer. In the present work, two models of the profilometer i.e. Sloan Dektak-II and Dektak-150 supplied by Veeco Instruments Inc. were employed. Before carrying out the thickness measurements of the film, the blank substrate was scanned to check its flatness. It should be noted that the substrates were found to be flat in all the cases with a variation of less than 0.15 μ m over its entire length of ~16mm. Figure 2.2 shows a typical thickness profile for an acrylic dispersion film. Note that the region between P and Q is crack free. Hence the critical cracking thickness (CCT) corresponds to the maximum thickness in this region. Further, as mentioned above, the films for some of the flocculated dispersions

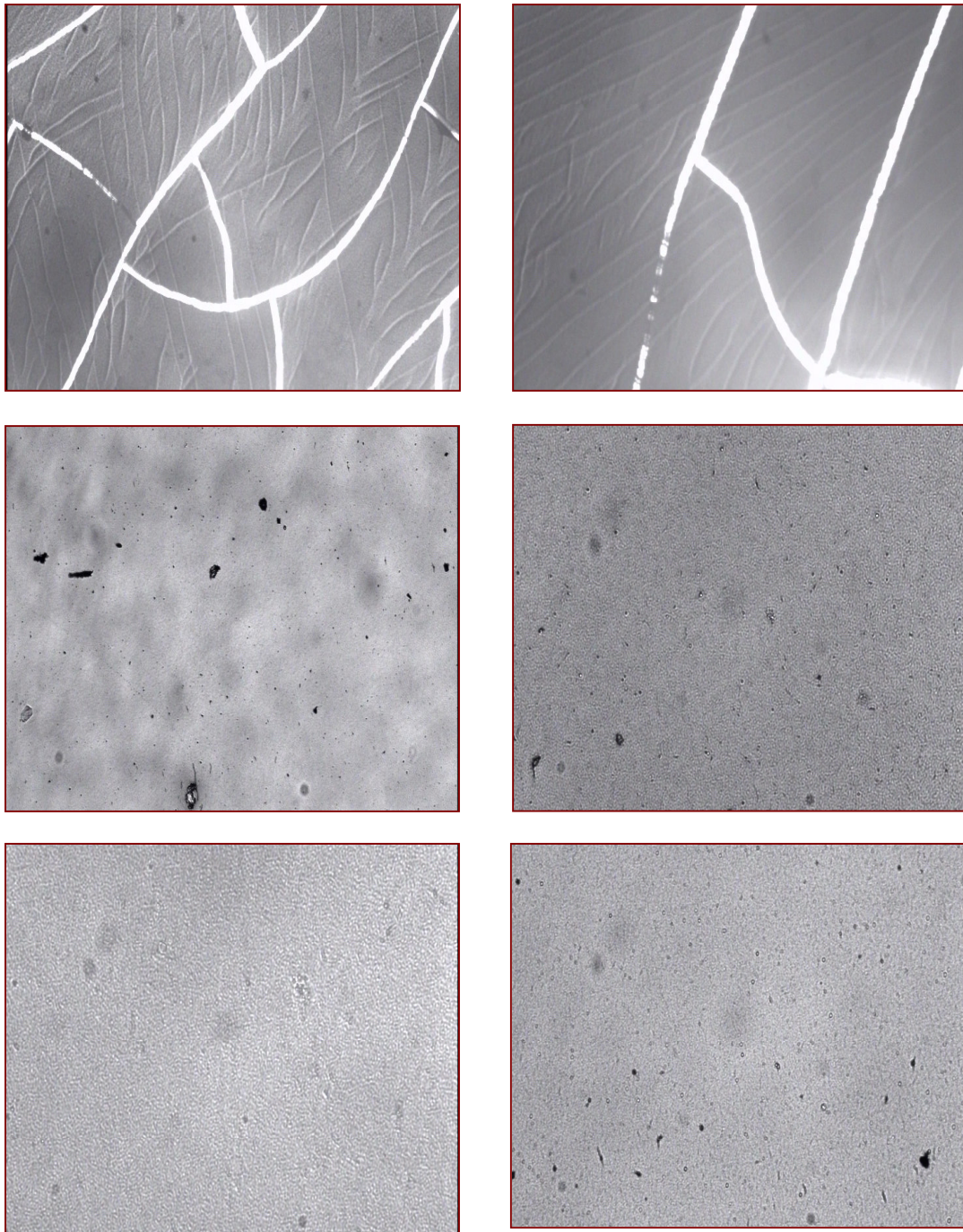


Figure 2.1: Optical micrographs showing the films with and without cracks at different magnifications of 4X, 10X, 20X and 40X respectively. Note that the films were cast from styronal ND 811 (styrene-butadiene random copolymer) dispersion at a temperature of 25⁰C and a relative humidity of 52%.

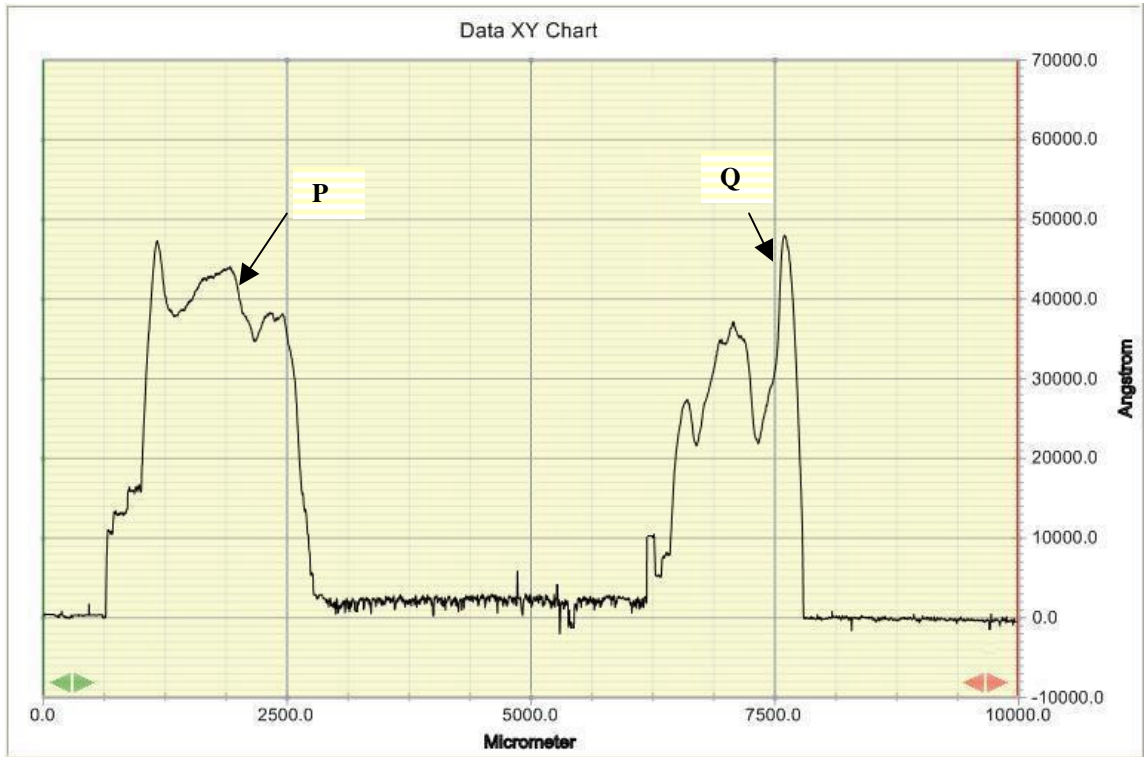


Figure 2.2: A typical thickness profile for an acrylic dispersion film. Note that the region between P and Q was having no cracks.

were dried in open vials. Measurement of the thickness profile for such films was a little tricky. Here, a small piece of the dried film was carefully scrapped off the central part of the vial and was used for thickness measurement. The small piece of the film was kept on a glass substrate and the sample was scanned under the profilometer. Note that the surface of the glass where the piece of the dried film was kept was made slightly wet. This ensured that the small adhesion force due to the capillarity holds the film in place while the stylus scans the profile. Figure 2.3 shows the thickness profile for one such measurement. As can be seen, the thickness of the film at the central part of the vial is almost constant.

2.2. MEASUREMENT OF MAXIMUM CAPILLARY PRESSURE

Maximum capillary pressure is an important parameter in the study of film formation and cracking in aqueous dispersions. In all the subsequent chapters, the concept of maximum capillary pressure is used to compare the predictions of the theoretical models with the experimental measurements. Hence, the exact knowledge of maximum capillary pressure attained during drying is very critical for understanding the film formation and cracking mechanisms in aqueous dispersions. In this work, we measured the maximum capillary pressure using two different techniques/methods as discussed below.

2.2.1. Measurement of maximum capillary pressure using a capillary tube

A schematic of the experimental set-up used to measure the maximum capillary pressure is shown in figure 2.4. A glass capillary of length 10cm (approximate) and an inside diameter of 300 μ m (approximate) was partially filled with dispersion such that

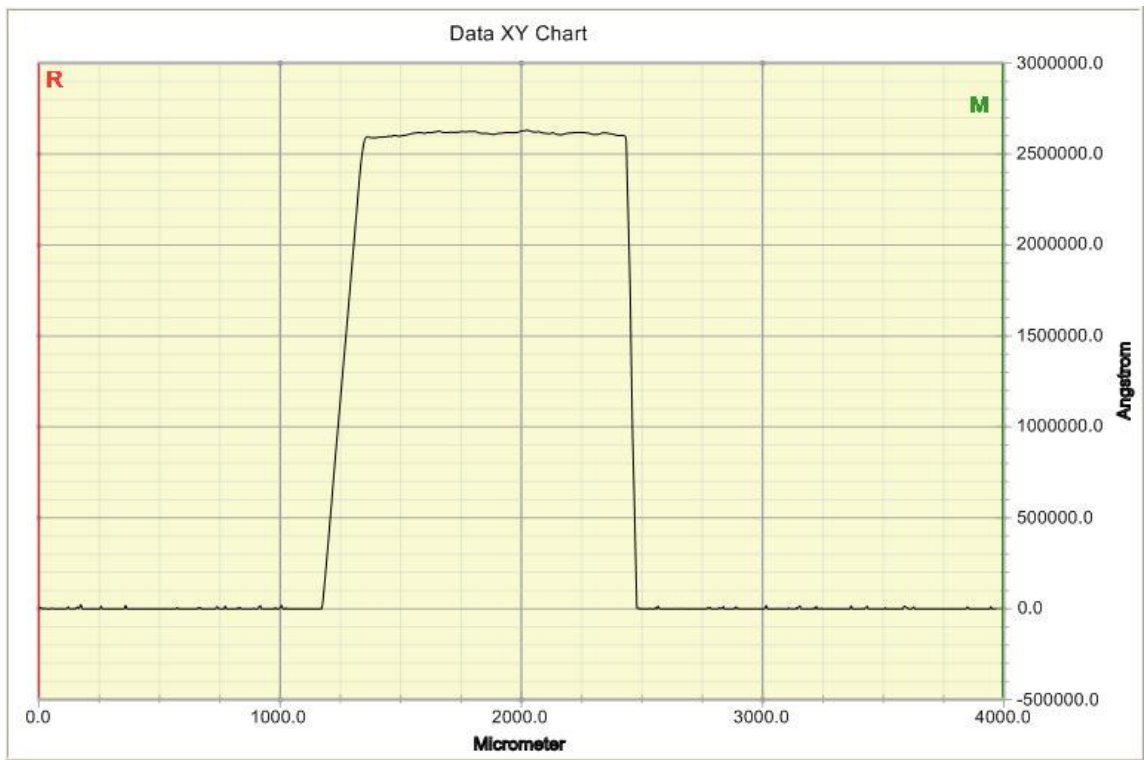


Figure 2.3: Thickness profile for a flocculated dispersion film dried in an open vial.

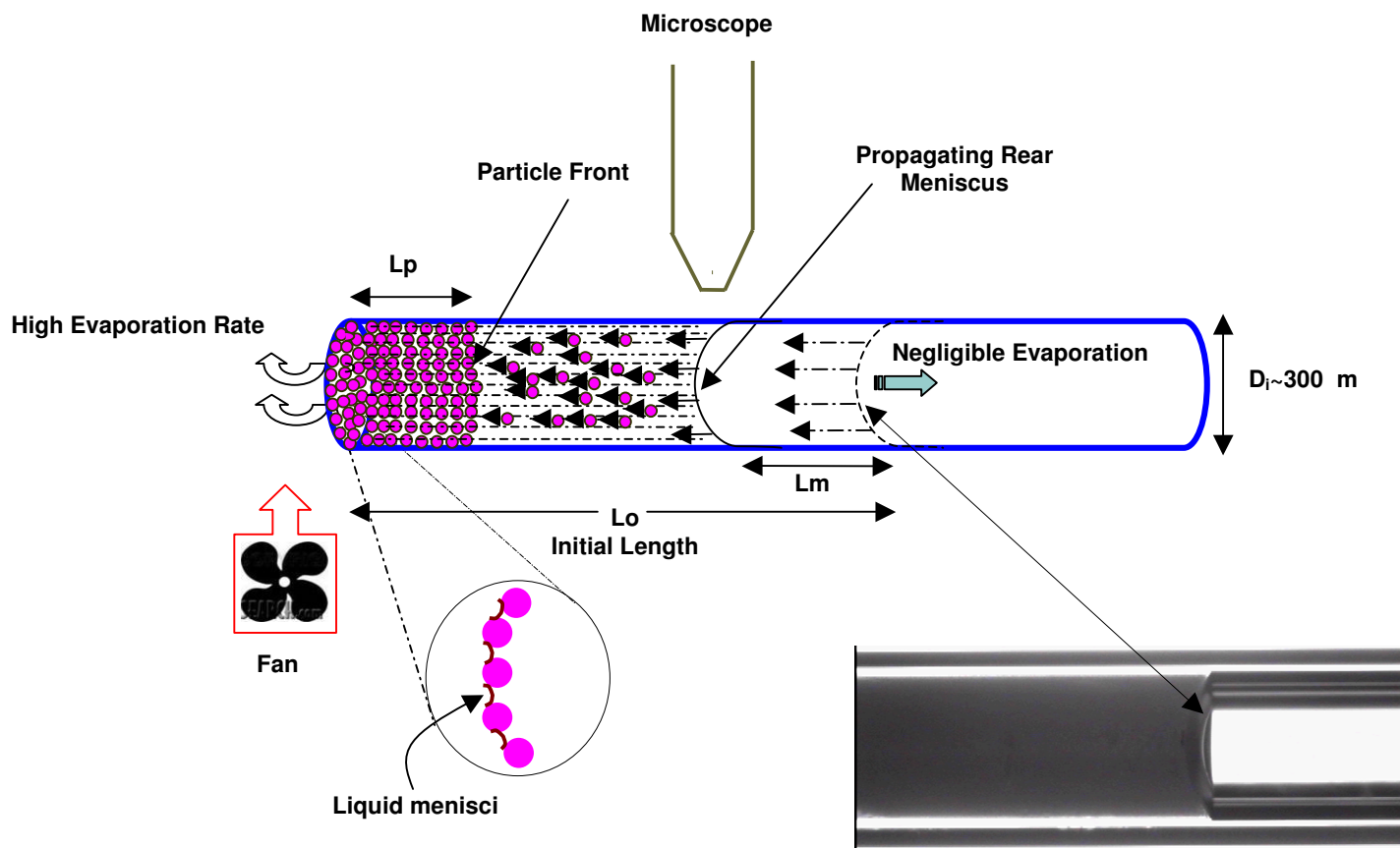


Figure 2.4: Experimental measurement of maximum capillary pressure using a capillary tube.

one of the dispersion-air menisci is located inside the tube (rear meniscus) while the other is located at the mouth of the capillary (front meniscus). The initial length of the dispersion column was varied from 0.5 to 2 cm. As the rear meniscus is well within the tube, the air inside the capillary rapidly saturates with water resulting in negligible evaporation at the rear meniscus. Thus all the evaporation occurs at the front end of the capillary tube. Further, a fan was placed close to the front end of the capillary to increase the evaporation rate. The position of the rear meniscus was tracked using an optical microscope. The high rate of evaporation at the front end of the capillary tube causes the particles to form a packed region that grows with time. Presumably, the high rate of water loss at the front-end results in liquid menisci between the particles packed in the first layer thereby creating a region of low pressure that draws the liquid from inside the capillary to sustain the evaporation. The increasing length of the packed region requires the curvature of the inter particle menisci at the front end to increase so as to overcome the increased bed resistance. This implies that until the capillary pressure reaches the maximum value, the contact line will remain fixed at the first layer of particles consequently resulting in constant evaporation rate. A simple mass balance shows that the evaporation rate is equal to the speed of the rear meniscus as long as the front menisci are pinned on the first layer of particles. Once the capillary pressure reaches the maximum value, liquid menisci are no longer capable of overcoming the increased bed resistance that causes the menisci to recede into the sample. The latter will manifest as a fall in the evaporation rate.

One may be tempted to attribute the fall in the evaporation rate to the Kelvin's phenomena (capillary condensation) where larger negative curvatures suppress the

evaporation of the liquid. This effect, however, becomes dominant when the radius of curvature becomes comparable to the molecular dimensions. Since the particles in the present case are much larger ($\geq 100\text{nm}$), this phenomenon is unlikely. Also, since the colloidal particles in the dispersions used for the current experiment are rigid, the possibility of fall in evaporation rate due to particle deformation is also ruled out.

Some of the initial drying experiments were conducted with extremely dilute dispersions that contained a very small fraction of particles ($\phi_0 \cong 0.006$). Figure 2.5 plots the rear meniscus position with time for one such experiment. As can be seen, the meniscus propagation rate, which is also the evaporation rate, is constant throughout the experiment as there is no significant build up of particles thereby suggesting that the liquid menisci stay at the first layer of particles. Figure 2.6 shows similar plots for more concentrated colloidal silica and latex dispersions. Initially, the rear meniscus propagates at a constant rate, implying that the capillary menisci are located at the leading edge. Once the capillary pressure reaches its maximum value, further evaporation causes the liquid menisci to recede into the bulk resulting in the decrease of the rear meniscus propagation speed. As expected, the position of the rear meniscus at which the evaporation rate starts to decrease varied over experiments due to the varying initial particles volume fraction and ambient conditions.

If L_m is the length over which the rear meniscus propagates before the evaporation rate falls (see figure 2.4), then a simple mass balance that neglects particle

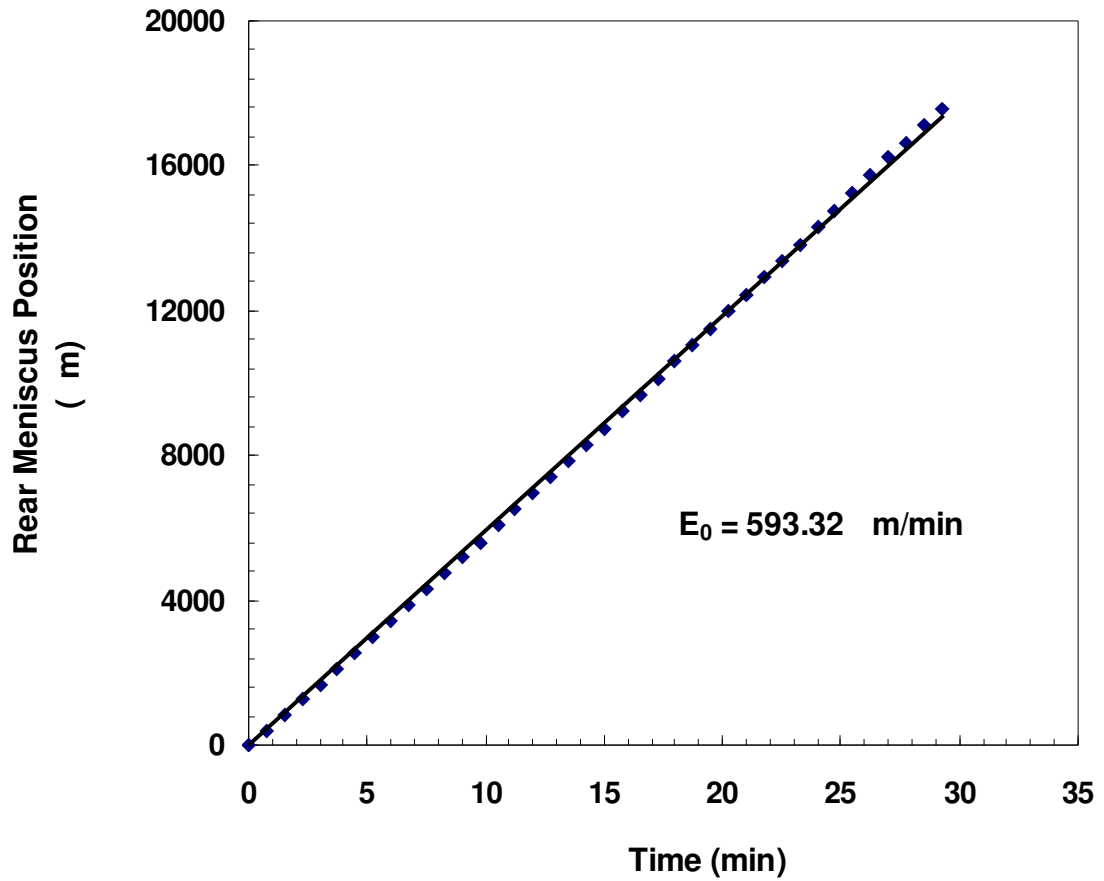
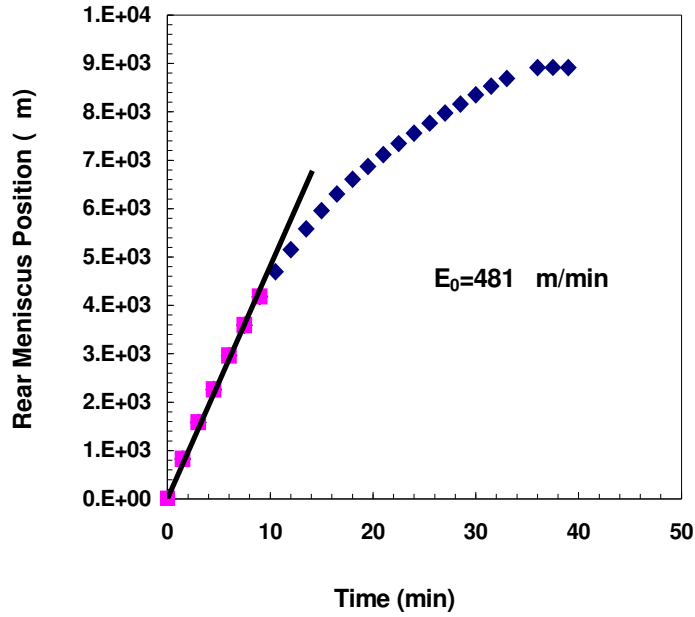
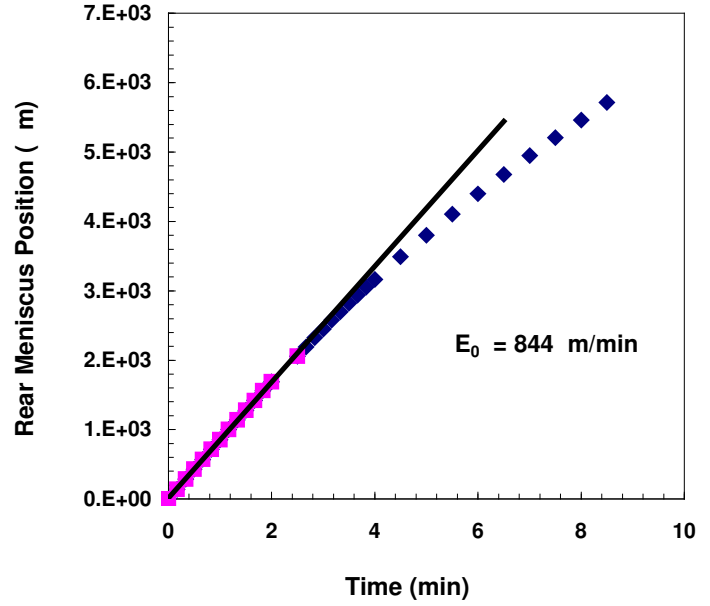


Figure 2.5: Rear meniscus propagation for a dilute dispersion ($\phi_0 \cong 0.006$) of colloidal silica dispersion. The experiments were conducted at an ambient temperature of $32 \pm 1^\circ\text{C}$ and a relative humidity of $50 \pm 1\%$.



(a)



(b)

Figure 2.6: Rear meniscus propagation for (a) silica dispersion of ($\phi_0 = 0.03$) at an ambient temperature of $25 \pm 1^{\circ}\text{C}$ and a relative humidity of $54 \pm 4\%$ and, (b) styronal ND 811 latex dispersion for ($\phi_0 = 0.05$) at an ambient temperature of $34 \pm 1^{\circ}\text{C}$ and a relative humidity of $46 \pm 1\%$.

diffusion gives the length of the packed region corresponding to the maximum capillary pressure,

$$L_p = \frac{L_m \phi_0}{(\phi_{rcp} - \phi_0)} \quad (2.1)$$

Here, ϕ_{rcp} is determined from the length of the packed layer measured at the end of the experiment.

The pressure drop across the packed bed is then given by the Darcy's law,

$$-\Delta P = \frac{E_0 L_p}{k} \quad (2.2)$$

where E_0 is the evaporation rate, μ is the viscosity of water and k is the permeability of packed bed. Since the pressure drop due to the dispersion flow in the capillary is negligible compared to (2.2), the above pressure drop also gives the maximum capillary pressure.

2.2.2. Measurement of maximum capillary pressure using Dewpoint PotentiaMeter

We also measured the maximum capillary pressure using a Dewpoint Potentiameter (WP4[®]). This is a standard instrument used by research community in the area of soil mechanics to establish the soil-water characteristic curve (SWCC).¹⁻³ The soil water characteristic curve gives the relationship between soil suction and the water content present in the soil and is a standard approach to determine the properties of unsaturated soil.⁴⁻⁸ As soil sample is also an aqueous suspension of particles, the same concept can be used to measure the suction (capillary pressure in general) for any aqueous dispersion. We used Dewpoint PotentiaMeter to measure the capillary pressure for some of the dispersions used in the present work. The following section explains the

measurement of maximum capillary pressure using a Dewpoint PotentiaMeter (WP4[®] Decagon Devices Inc.) in detail.

A Dewpoint PotentiaMeter (WP4[®]) works on the chilled mirror concept and can be used to measure the suction as high as 80 MPa. The device consists of a sealed block chamber equipped with a mirror, dew point sensor, which is a photoelectric cell, a thermocouple that acts as a temperature sensor, an infrared thermometer (optical sensor) and a fan. The schematic of the instrument is shown in figure 2.7. A soil specimen (or in general any sample whose suction is to be measured) of approximately 6 ml is placed in the PVC cup and equilibrated with the air in the headspace of the sealed block chamber for its relative humidity. At equilibrium, the water potential of air in the chamber is the same as the water potential or suction of the sample, which occurs within 5–15 minutes. Note that the water potential or suction of the sample is but the same as the capillary pressure of the sample. A chamber fan is provided to accelerate the process of equilibration. The relationship between the total suction, ϕ , and the vapor pressure of air in the headspace can be expressed using Kelvin's equation as follows,

$$p = p_0 \exp\left(\frac{2\gamma}{r} * \frac{V_{mol}}{RT}\right) \quad (2.3)$$

where R is the universal gas constant, T is the temperature of the sample in K, p is the vapor pressure of air, p_0 is the saturation vapor pressure, r is the radius of curvature of the liquid menisci and V_{mol} is the molar volume of water and is equal to $18 \times 10^{-6} \text{ m}^3 / \text{gmol}$.

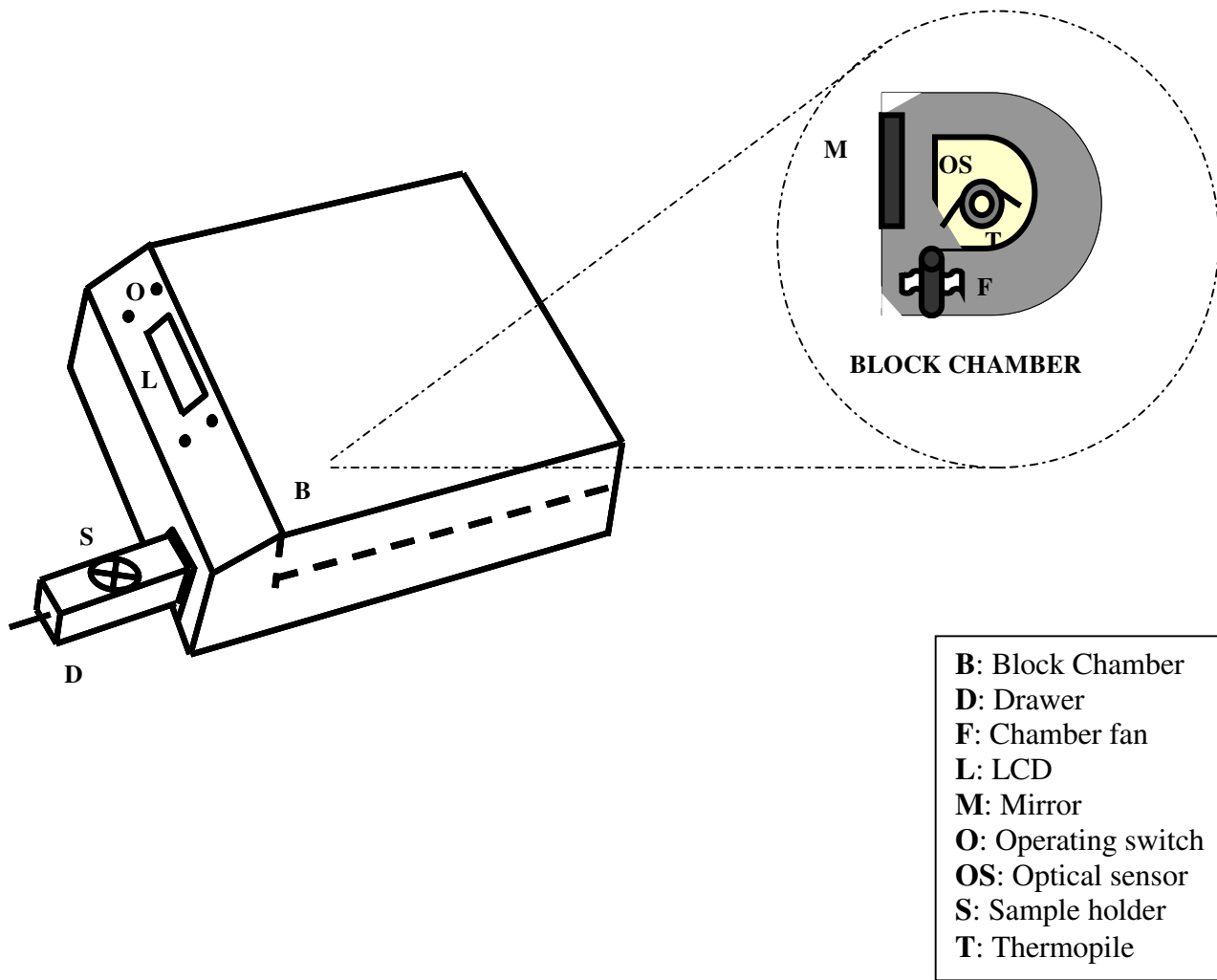


Figure 2.7: Schematic of the Dewpoint Potential Meter used to measure the maximum capillary pressure adapted from Shah et al.¹

If the capillary pressure, $\frac{2\gamma}{r}$, is denoted by the total suction, ϕ , the above equation on rearranging the terms becomes,

$$\phi = \frac{RT}{V_{mol}} \ln \frac{p}{p_0} \quad (2.4)$$

A photoelectric cell detects the condensation on the mirror and the thermocouple records the temperature at which condensation occurs. The infrared thermometer is used to measure the specimen temperature. At equilibrium, the headspace vapor pressure is measured and the saturation vapor pressure is computed. With the assistance of the in-built software, the total suction of the soil specimen (in MPa and pF units) is displayed on the LCD panel with its temperature. Before carrying out the capillary pressure measurements, the weight of the sample cup along with the specimen was recorded using a high precision balance in each run. This gravimetric analysis is used to find the solid volume fraction corresponding to a specific pressure measurement run. Before using the WP4, it was calibrated by adopting the following procedure and using standard solution of 0.5 M KCl, which should yield a suction of 2.19 ± 0.1 MPa, at 25 °C, (Decagon Services Ltd., 2002). Hence using the above procedure, the capillary pressure versus volume fraction data was generated. The maximum capillary pressure was then taken as the capillary pressure corresponding to the random close packed volume fraction of 0.64 (stable dispersion) and when the film was crack free.

2.3 MEASUREMENT OF STRESS IN DRYING DISPERSION

During film formation, an aqueous dispersion undergoes a complete transformation from a stable colloidal dispersion to a mechanically coherent film. As

described earlier, during the second stage of film formation, large capillary forces deform the particles and generate transverse tensile stresses in the plane of the film. If the magnitude of this tensile stress increases beyond a critical value, cracks nucleate which ultimately leads to failure of the film.^{10,11} The knowledge of this maximum tensile stress is important for understanding the deformation mechanism and to produce mechanically coherent films. In the following sections, we will explain the experimental technique used to measure the tensile stress in a drying film.

The schematic of the experimental set up used to measure the tensile stress in a drying film is shown in figure 2.8. A thin layer of the latex dispersion is applied on a thin silicon wafer (thickness ~128 μ m). The substrate (silicone wafer) is clamped on one end whereas the other end is free such that it forms a cantilever type of beam. The silicon wafer used was ~15 mm long and 4.5 mm in width. The reason for using a silicon wafer over other metallic substrates is its reflecting surface. Further, as the wafer is very flat, there is no residual stress in the substrate. A laser beam from a laser source is incident on the free end of the substrate that reflects the incident beam. The beam reflected from the substrate is collected by a position sensitive detector (On-track[®]). As the name suggests, the detector gives the position data (i.e. the x, y coordinates) of the laser beam on the detector surface. The orientation of the detector is set in such a way so that the reflected beam falls normally on the surface of the detector. The entire detector assembly is mounted on an X-Y traverse so that the desired positioning can be done with great accuracy. Hence in the present set up both, the laser source and the detector can be adjusted easily to get the desired configuration. The position data (i.e. the x, y coordinates

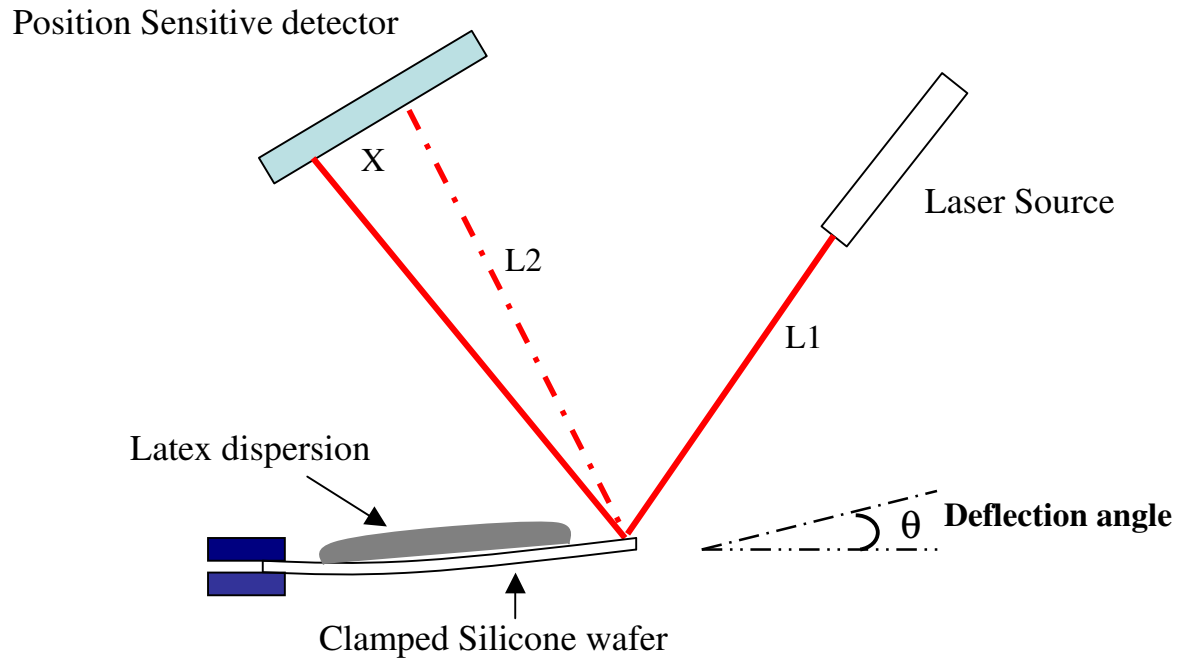


Figure 2.8: Schematic of the experimental set-up used to measure the stress in a drying film.

of the reflected beam) from the detector is directly fed to a computer through a national instrument card (SCB-68[®]). The data card gives the output in volts that is converted to the corresponding length units by calibrating the instrument as discussed in the next section. Finally the clamped substrate, after the film is applied, is enclosed in a plexiglas so as to maintain a stagnant environment during measurements. A digital hygrometer is also kept inside the plexiglas to measure the temperature and humidity inside the chamber.

2.3.1 Calibration and stress measurements

As the film dries, the drying stresses bend the substrate. The bending of the substrate causes a small movement of the reflected beam on the surface of the detector. As discussed above, the new position of the reflected beam can be sensed by the detector and is directly acquired by the computer. Finally, the displacement of reflected beam on detector surface is correlated to the amount of deflection in the substrate that can further be related to the average stress in the film as,

$$\sigma_f(t) = \frac{E_s t_s^3}{12 t_f(t) L_f (t_s + t_f(t))} \tan^{-1} \left(\frac{X(t)}{L_{Laser}} \right) \quad (2.5)$$

where E_s is the elastic modulus of the substrate, L_f is the length of the film, L_{Laser} is the length of the initial reflected laser beam, $X(t)$ is the displacement of the beam on detector surface and t_s, t_f are substrate and film thickness respectively. The film thickness changes continuously as water evaporates and the thickness at any instant is related to the original thickness as

$$t_f(t) = t_{f0} - \dot{E} t \quad (2.6)$$

where t_{f0} is the film thickness at the initial volume fraction and \dot{E} is the evaporation rate in (m/s). The rate of evaporation was constant throughout the experiment and was calculated by a simple mass balance. Here, the amount of water present in the dispersion at the start of the experiment was known. Further, to know the amount of water towards the end of the experiment, the clamped substrate was removed immediately after the film cracked and was put on a weigh balance where the weight versus time data was acquired for the last few points. Since the time from the start of the experiment is continuously logged, a simple mass balance gives the rate of evaporation. Figure 2.9 shows that the weight of the sample decreases at a constant rate, which indicates a constant evaporation rate. The solid line is a linear fit to all the points and the evaporation rate (in g/s) is given by the slope of the line. In this particular experiment, the crack occurred around 840 s and figure 2.10 shows the evaporation rate calculated by considering the first point and the last three data points that were logged after the nucleation of the crack. The evaporation rate thus obtained differs by less than 1% from the true value. We therefore adopted this technique to obtain both the stress and evaporation rate data from the same experiment.

For calibration of the instrument, a blank substrate (silicone wafer) is employed. After making the initial settings (i.e. making sure that the reflected beam falls normally on the surface of the detector), the detector is moved in X-direction by a known amount using the X-Y traverse. The displacement of the laser point on the detector surface is displayed on the computer in units of volts. Further, this displacement can also be calculated geometrically since the angle to which the detector is inclined with horizontal is known. Hence the measured displacements in volts can be related to the calculated displacement in length units. The calibration technique is shown schematically in figure 2.11.

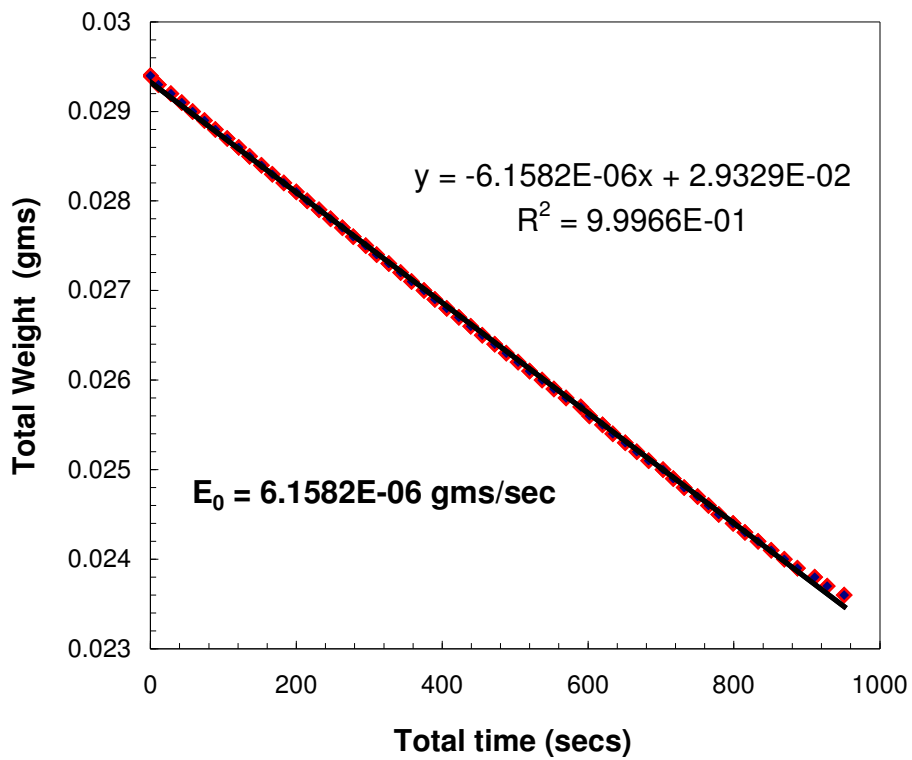


Figure 2.9: Typical weight loss vs. time data for the drying of dispersions used in the present work.

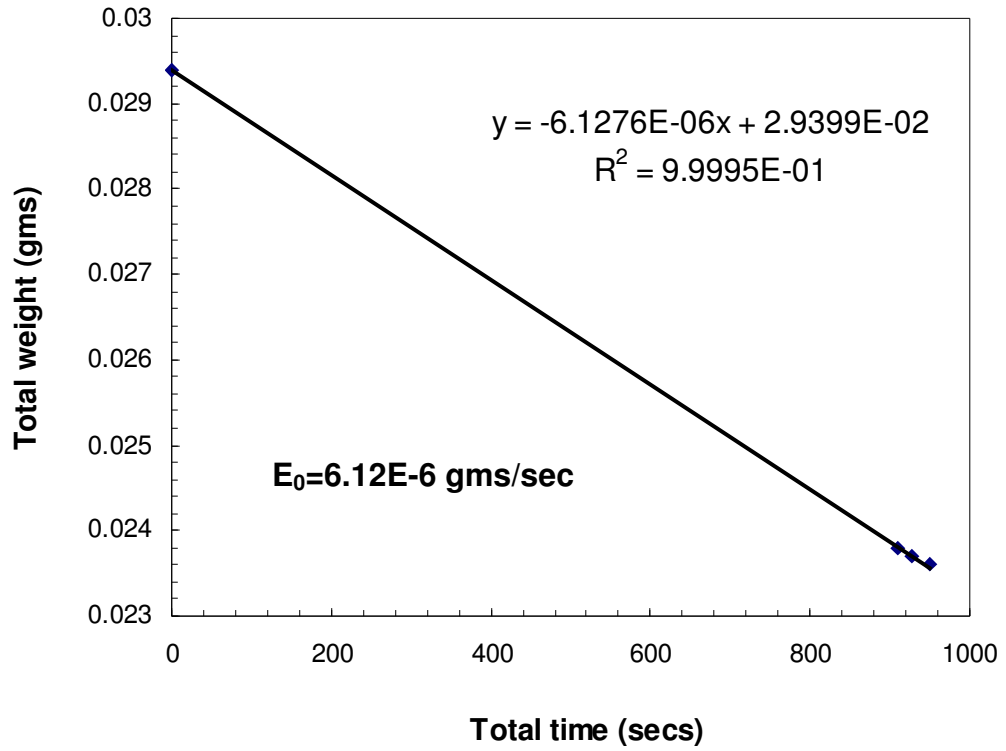


Figure 2.10: Calculated evaporation rate by considering the first and last few points.

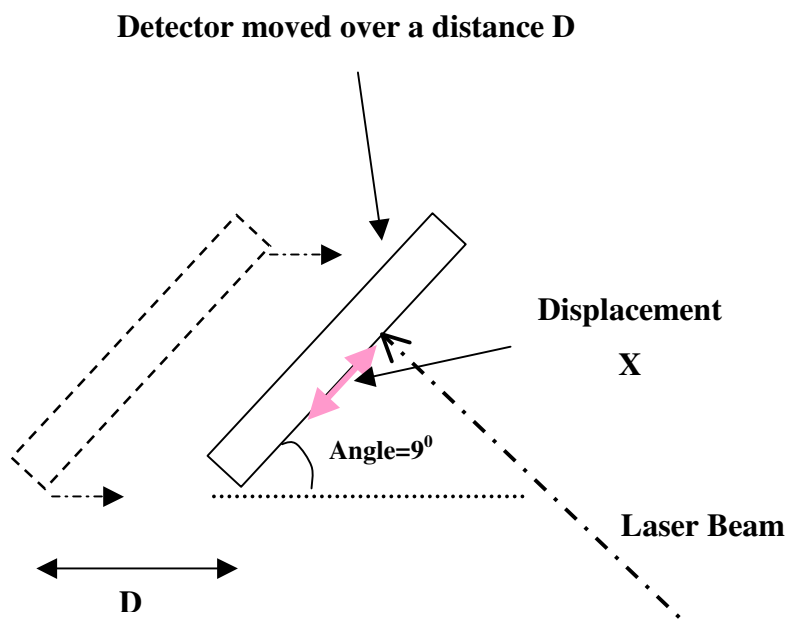


Figure 2.11: Technique used to calibrate the set-up.

2.4 CONCLUSION

In this chapter, we discussed various techniques to obtain the stress profile in a drying dispersion, critical cracking thickness, maximum capillary pressure and evaporation rate. The next three chapters report experimental results using one or more of these techniques.

REFERENCE

- [1] P. H. Shah, S. Sreedeeep, and D. N. Singh. Evaluation of methodologies used for establishing Soil-Water Characteristic Curve. *J ASTM Int.*, 3 (6): 1-11, 2006.
- [2] V. K. Thakur, S. Sreedeeep, and D. N. Singh. Laboratory investigations on extremely high suction measurements for fine-grained soils. *Geotech. & Geolog. Eng.*, 24: 565–578, 2006.
- [3] E. C. Leong, S. Tripathy, and H. Rahardjo. Total suction measurement of unsaturated soils with a device using the chilled-mirror dew-point technique. *Geotechnique*, 53(2): 173–182, 2003.
- [4] D. G. Fredlund and A. Xing., Equations for the Soil-Water Characteristic Curve. *Can. Geotech. J.*, 31 (3): 521–532, 1994.
- [5] S. Sreedeeep and D. N Singh. A Study to Investigate Influence of Soil Properties on its Suction. *J. Test. Eval.*, 33 (1): 579–584, 2005a.
- [6] K. Garbulewski and S. Zakowicz. Suction as an Indicator of Soil Expansive Potential. *Proceedings of the First International Conference on Unsaturated Soils*, E. E. Alonso and P. Delage, Eds., Paris, 2: 593–597, 1995.
- [7] S. K. Vanapalli, D. G. Fredlund, and D. E. Pufahl. The Relationship Between the Soil-Water Characteristic Curve and the Shear Strength of a Compacted Glacial Till. *Geotech. Test. J.*, 19 (3): 259–268, 1996.
- [8] R. G. McKeen. A model for predicting expansive soil behaviour. *Proceedings of the 7th International Conference on Expansive soils*, Dallas, 1: 1–6, 1992.
- [9] Decagon Services Ltd. WP4 User’s Manual, Decagonservices, U.S.A., 2002.
- [10] M. S. Tirumkudulu and W. B. Russel. Role of capillary stresses in film formation. *Langmuir*, 20 (7): 2947-2961, 2004.
- M. S. Tirumkudulu and W. B. Russel. Cracking in drying latex films. *Langmuir*, 21 (11), 4938-4948, 2005.

CRACKING IN DRYING COLLOIDAL FILMS

Chapter 3

CRACKING IN DRYING COLLOIDAL FILMS

ABSTRACT

It has been long known that thick films of colloidal dispersions such as wet clays, paints and coatings crack under drying. Although capillary stresses generated during drying have been recently identified as the cause for cracking, the existence of a maximum crack-free film thickness that depends on particle size, rigidity and packing has not been understood. Here, we identify two distinct regimes for crack free films based on the magnitude of compressive strain at the maximum attainable capillary pressure and show remarkable agreement of measurements with our theory. We anticipate our results to not only form the basis for design of coating formulations for the paints, coatings and ceramics industry but also assist in the production of crack free photonic band gap crystals.

3.1 INTRODUCTION

When a thin film of wet paint or coating containing suspended sub-micron sized colloidal particles is dried on a substrate, evaporation of the solvent concentrates the particles into a closed packed array. Further evaporation causes the liquid menisci at the top layer of the particle network to exert compressive capillary force on the particle network.^{1,2} The film generally binds to the substrate and resists deformation in the

transverse direction giving rise to transverse tensile stresses.³ If the particles are soft, they deform to close the pores but in case of hard particles the film cracks to release the stresses. Though cracking in drying systems has been investigated on diverse systems such as wet clays,⁴⁻⁷ ceramic films,^{8,9} latex and model colloidal dispersions,^{10,11} it is only recently that a fundamental understanding of the cracking mechanism is beginning to emerge.^{3,12-14} For instance, it has been long observed that irrespective of the particle size and hardness, cracks nucleate spontaneously only above a critical film thickness. Chiu et al.^{8,9} measured the maximum crack free thickness for films cast on glass substrates and prepared from aqueous dispersions of alumina, polystyrene, and zirconia. The thickness was independent of the drying rate and increased with particle size suggesting that films containing large particles were less likely to crack; though crack free films of polystyrene spheres of similar size were considerably thinner than those obtained with alumina and zirconia. The measured critical tensile stress at cracking scaled with the capillary pressure (based on particle size). On the theoretical front, Meakin^{10,11} and others¹⁴ adopted the statistical description where, starting from a uniformly stressed film, bonds (or springs) between the particles are broken at random and the system relaxed to a new equilibrium. When this process is repeated a number of times, crack patterns emerge that resemble those observed in experiments. Alternatively, the continuum approach, that will be adopted here, assumes a macroscopic stress versus strain relation along with energy balances to predict crack dynamics. To this end, we adopt the non-linear stress strain relation proposed by Routh and Russel² for drying films composed of a homogeneous packing of deformable particles. The constitutive relation was derived by accounting for the viscoelastic deformation of a pair of particles due to both interfacial tension and external forces such as those exerted by contacting neighbors. Tirumkudulu and Russel³

measured the stress evolution and the crack spacing for drying films of dispersions containing polymer spheres of varying diameters and shear moduli. They employed the Griffith's criterion for equilibrium crack propagation¹⁵ along with the aforementioned constitutive relation for a network of identical elastic spheres to predict the critical stress (σ_c) for nucleation of an isolated crack,

$$\frac{\sigma_c R}{2\gamma} = 0.1877 \left(\frac{2R}{h} \right)^{\frac{2}{3}} \left(\frac{GM\phi_{rcp}R}{2\gamma} \right)^{\frac{1}{3}} \quad (3.1)$$

Here, R is the particle radius, γ is the solvent-air interfacial tension, h is the film thickness at cracking, G is the shear modulus of the particles, M is the coordination number and ϕ_{rcp} is the particle volume fraction at random close packing. The model assumed no-slip between the substrate and the particle layer in contact with it, with the former assumed to be rigid. Consequently, the film consolidates in the direction perpendicular to its plane. For particles and substrate of comparable modulus, the multiplying constant in Eq. (3.1) reduces by a factor of 0.7. Thus Eq. (3.1) predicts thinner films to be tougher as they crack at higher stresses. The predicted scaling agrees with experiments though the measured values were about twice the predictions. Next, the biaxial stress, $\sigma = (3/35)MG\phi_{rcp}(\epsilon)^2$ in the crack free state at the maximum compressive strain, $\epsilon_{\max} = 1 - \phi_{rcp}$, was set equal to the critical stress for cracking to obtain the critical thickness,^{3,16}

$$h_{\max} = \frac{37\gamma}{GM\phi_{rcp}(1 - \phi_{rcp})^3} \quad (3.2)$$

This regime, henceforth referred to as the *strain-limited* regime, predicts the critical thickness to be independent of particle size and increases with decrease in modulus, both

in variance with experiments.⁸ These discrepancies led to the current investigation where we show the existence of a second regime for crack free films which is applicable for films containing hard particles.

3.2 EXPERIMENTAL SECTION

Our experiments were performed with various stable aqueous dispersions containing particles over a wide range of sizes and shear moduli. Silica dispersion of particle volume fraction 0.03 was obtained from Colloidal Dynamics (CD 350 NM[®]) and concentrated to 0.14 via centrifugation. Colloidal silica dispersion (LUDOX, TM 50) was procured from Sigma-Aldrich and diluted to 0.03 volume fraction by adding de-ionized water. Acrylic dispersions with product codes BX 261, BX 269, BX 273 and Standard were obtained from ICI Inc. and diluted to particle volume fraction of 0.13 by adding de-ionized water. Further, the styrene-butadiene dispersion with product code Styronal ND 811 was obtained from BASF and diluted to 0.06 particle volume fraction by adding de-ionized water.

Thin circular films of approximately 10 mm diameter were cast on clean glass substrates using a spin coater. The experiments were conducted at temperatures ranging from 26 to 29⁰C and relative humidity from 50 to 60%. The thickness of the final dried film could be varied by controlling the initial amount of dispersion disbursed on to the substrate. On complete drying, the film was examined for cracks under an upright optical microscope (Olympus, BX-60) at varying magnifications. Most films exhibited cracks at the rim and close to the center (relatively thick regions) with the remaining area devoid of cracks. The thickness profile of the film was measured using a surface profilometer (Sloan Dektak-II). The critical thickness corresponds to the maximum thickness of the

film in the crack free region.

3.3 RESULTS AND DISCUSSION

Figure 3.1 shows a typical thickness profile for one such film with the region between S and T being crack free. Films whose thicknesses were everywhere less than the critical thickness were completely devoid of cracks. Not only were the measured critical thicknesses larger than that predicted by Eq. (3.2) by over two orders, scanning electron microscopy images (Figure 3.1 B and C) of the top and interior of the crack free domains showed negligible particle deformation even for films containing polymer spheres. These observations suggest a maximum capillary pressure (P_{\max}) beyond which the liquid menisci recede into the porous film, limiting the deformation of the film (Figure 3.2). Thus, we predict a *stress-limited* regime, where the critical thickness is set by the balance of the biaxial stress¹⁷ at the maximum attainable capillary pressure (P_{\max}) and the critical stress for cracking, Eq. (3.1),¹⁶

$$h_{\max} = 0.64 \left[\frac{GM\phi_{rcp}R^3}{2\gamma} \right]^{1/2} \left[\frac{2\gamma}{(-P_{\max})R} \right]^{3/2}. \quad (3.3)$$

Since the final crack free film is porous, the strain at the maximum attainable capillary pressure, $\sqrt{(28/3)(-P_{\max})/MG\phi_{rcp}}$, is less than $(1-\phi_{rcp})$. Interestingly, while the critical thickness decreases with shear modulus for the first regime, the trend is exactly opposite for the *stress-limited* regime. This is because for a given maximum capillary pressure, the stored elastic energy density decreases with increasing shear modulus, thereby allowing thicker crack free porous films.

A better insight into the above theoretical results can be gained by a simple scaling analysis. According to the nonlinear constitutive relation for a drying colloidal film containing monodisperse elastic spheres,² the transverse tensile stress scales with the

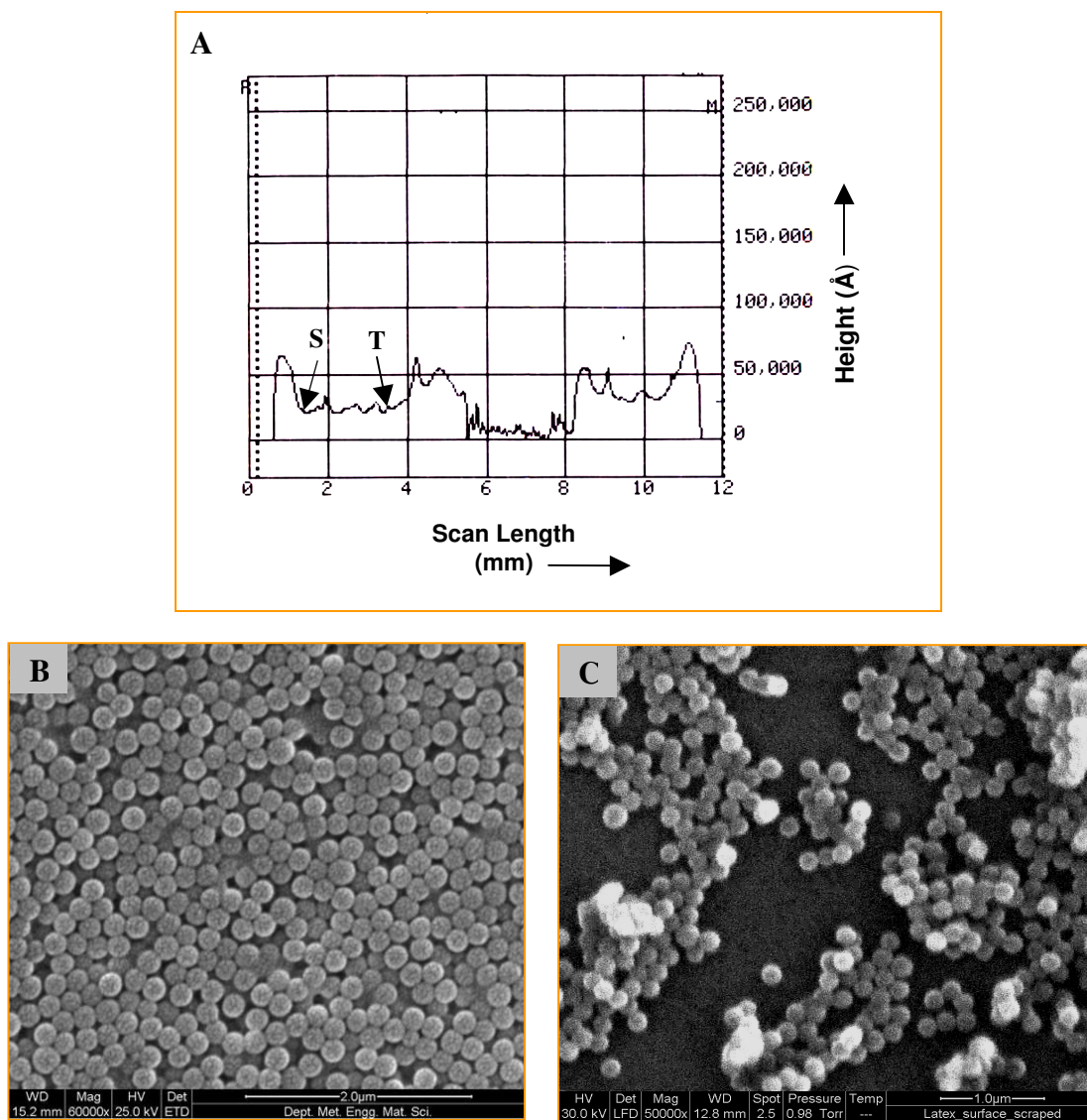


Figure 3.1: Thickness profile of a dried film. (A) Thickness profile measured along the diameter of a dry styrene-butadiene film. (B) SEM of the film surface in the crack free region. (C) SEM of the film interior in the crack free region. The region between S and T was crack free.

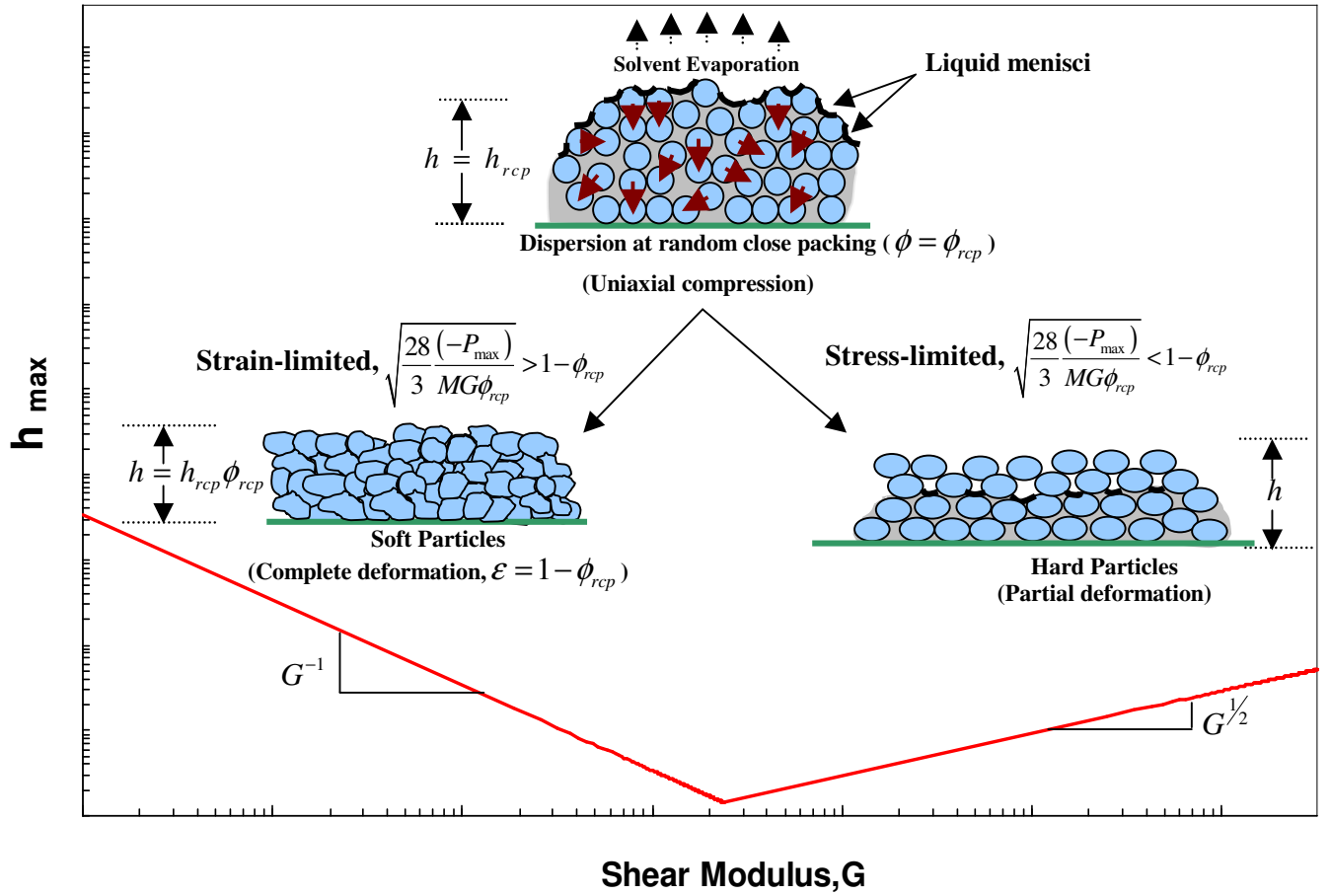


Figure 3.2: Critical thickness variations as a function of the shear modulus. At random close packing, the menisci at the top particle layer exert a compressive force on the particle network. For very soft particles, the particles deform completely to close the voids for capillary pressure less than the maximum so that the uniaxial compressive strain is, $\epsilon \equiv \frac{(h_{rcp} - h)}{h_{rcp}} = 1 - \phi_{rcp}$. In case of hard particles, the menisci adjust their curvature till the maximum capillary pressure (P_{max}) is reached, beyond which they recede into the network resulting in partial deformation.

square of the compressive strain, $\sigma \sim G\varepsilon^2$. When an isolated crack nucleates spontaneously in the film, portions of the film over a length that scales with the film thickness (h) relax, so that elastic energy recovery per unit length of the crack scales as, $E_{elastic} \sim h^2\sigma\varepsilon$. On setting this equal to the increased surface energy per unit length ($E_s \sim \gamma h$) gives (3.1), $\sigma_c \sim G^{1/3}(\gamma/h)^{2/3}$. The strain-limited regime is obtained when the capillary pressure is able to completely deform the particles without inducing a crack. This is possible only when the tensile stress at maximum deformation ($\varepsilon_{max} = 1 - \phi_{rcp}$) is less than the critical stress. Thus the critical film thickness (h_{max}) for this regime scales as $G^{1/3}(\gamma/h_{max})^{2/3} \sim G(1 - \phi_{rcp})^2$ giving (3.2), $h_{max} \sim \gamma/G(1 - \phi_{rcp})^3$. On the other hand, if the particles are so hard that even the maximum capillary pressure is not able to completely deform them, then the critical cracking thickness is obtained by equating the critical stress to the tensile stress at the maximum capillary pressure, $G^{1/3}(\gamma/h_{max})^{2/3} \sim (-P_{max})$, giving (3.3), i.e. $h_{max} \sim \gamma G^{1/2}/(-P_{max})^{3/2}$.

Figure 3.3 plots the measured critical thickness over a wide range of sizes and shear moduli against the characteristic scale for the stress-limited regime. Here, the particle volume fraction was measured by drying the dispersion in a capillary tube and noting the initial and the final length of the dispersion plug. The measured values of ϕ_{rcp} varied from 0.60 to 0.68 while that for Chiu et al.⁸ were from 0.59 to 0.62. While the measured values of ϕ_{rcp} were used for our experiments, we chose $\phi_{rcp} = 0.6$ for that of Chiu et al.⁸ The observed scaling is in remarkable agreement with the predictions over five orders of the characteristic scale. Interestingly, though both alumina and zirconia particles had a narrow size distribution, the particles were not spherical⁸ suggesting that

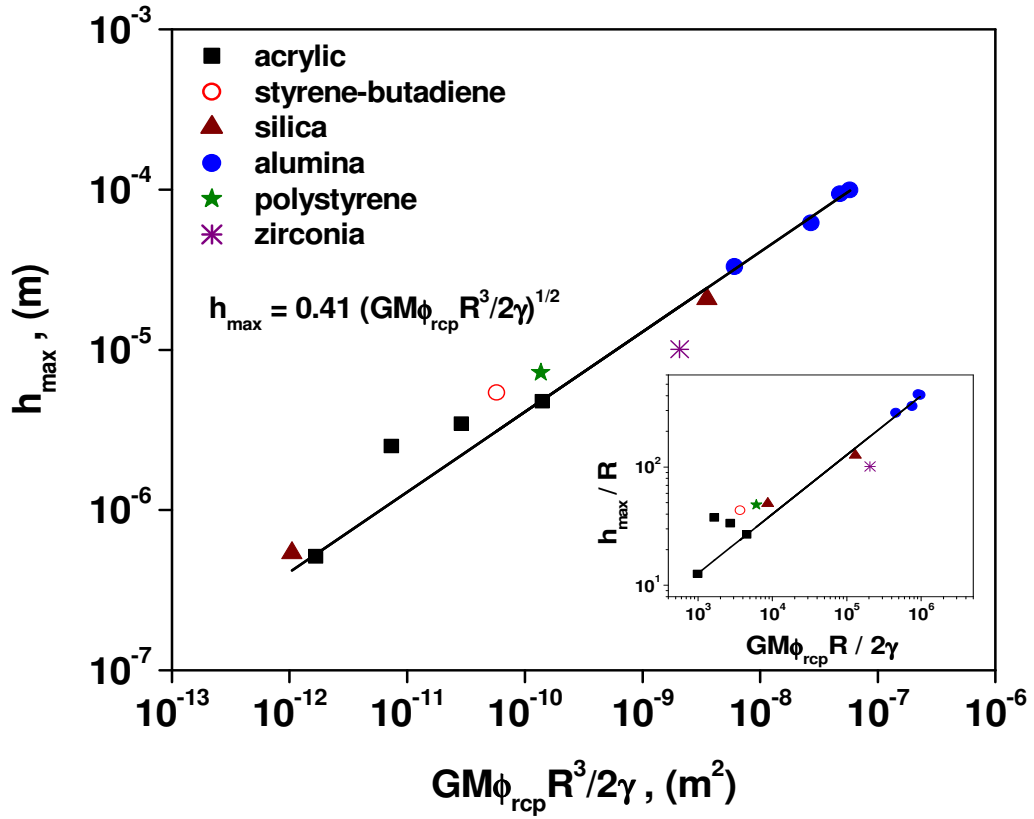


Figure 3.3: The measured critical thickness versus the characteristic scale, $\frac{GM\phi_{rcp}R^3}{2\gamma}$.

The data points are for films of acrylic (■, $G = 0.8$ GPa, $2R = 82, 133, 206$ and 353 nm, and $\phi_{rcp}(M) = 0.65(6.7), 0.66(6.8), 0.68(7.0)$ and $0.67(6.9)$, respectively), styrene-butadiene (○, $G = 1$ GPa, $2R = 250$ nm, and $\phi_{rcp}(M) = 0.64(6.6)$), silica (▲, $G = 31$ GPa, $2R = 330$ and 22 nm, and $\phi_{rcp}(M) = 0.60(6.1)$ for both), alumina⁸ (●, $G = 156$ GPa, $2R = 230, 379, 458$ and 489 nm, and $\phi_{rcp}(M) = 0.60(6.1)$ for all), polystyrene⁸ (★, $G = 1.6$ GPa, $2R = 300$ nm, and $\phi_{rcp}(M) = 0.60(6.1)$), and zirconia⁸ [(*, $G = 81$ GPa, $2R = 200$ nm, and $\phi_{rcp}(M) = 0.60(6.1)$). Here the value of surface tension, γ , is taken as 0.072 N/m for all the cases. The solid line is a power law with an exponent $\frac{1}{2}$ and the multiplying coefficient is obtained via regression. The inset plots the same data in the non-dimensional form.

in the present case, the asphericity of the particles does not significantly affect the critical thickness. The coefficient of the best fit (solid line) when compared with Eq. (3.3) gives the maximum attainable dimensionless capillary pressure, $(-P_{\max})R/2\gamma = 1.4$. We also measured the vapor pressure in equilibrium with a saturated dispersion of styrene-butadiene particles at close packing ($\phi_{rcp} = 0.64$) using a dew point potentiometer (WP4[®], Decagon Devices Inc.). The dimensionless capillary pressure was determined using Kelvin equation¹⁸ to be 1.2 ± 0.08 which is close to the predicted value of 1.4. Energetic arguments¹⁹ for a packing of identical spheres show that the maximum capillary pressure depends on the wetting characteristics of the solvent and is given by, $(-P_{\max})R/2\gamma = 3 \cos \theta \phi_{rcp} / 2(1 - \phi_{rcp})$, where θ is the wetting angle. At complete wetting and for $\phi_{rcp} = 0.64$, we obtain a value of 2.7. Given that the wetting angle will depend on the nature of particles, the predicted value of the maximum capillary pressure from the power law fit and that measured using the dew point potentiometer is within the expected range. Further, substituting the maximum capillary pressure in Eq. (3.3) results in the critical thickness being proportional to $\sqrt{M(1 - \phi_{rcp})^3 / \phi_{rcp}^2}$. Consequently, the close packing concentration/coordination number could be varied to control the critical thickness. Experiments⁸ show that the critical thickness increased by about a factor of two when the addition of electrolyte flocculated the dispersion and reduced the packing fraction of the final film from 0.62 to 0.53. Interestingly, with $M = 6.5$ for $\phi_{rcp} = 0.62$ and $M = 5$ for $\phi_{rcp} = 0.53$,²⁰ our model predicts an increase by a factor of 1.4, in line with the observations.

We also measured the crack spacing for a large number of dispersions. The dried film was examined under an optical upright microscope and for each film thickness, large no of cracks (>50) were considered to find the average spacing. The cracks were mostly radial and the distance between the cracks varied according to film thickness. Combined measurements of the thickness and crack spacing gave a number of data points from a

single sample. Figure 3.4 plots the variations in crack spacing with film thickness. Here in addition to our experimental results, we also took the spacing data from literature.^{3,4,7} As can be seen, the crack spacing varies almost linearly with the film thickness and agrees well with the predictions of a linear relationship between crack spacing and film thickness by Tirumkudulu and Russel.³

3.4 CONCLUDING REMARKS

Our study identifies a new regime for obtaining crack free films and thereby elucidates the fundamental mechanism responsible for cracking in drying dispersions. Since a control on the crack free film thickness is critical to several industrial coating processes, the results presented here could form the basis for efficient design of coating formulations. These results also have implications for the synthesis of photonic band gap crystals via the colloidal crystallization route where capillary forces induced during drying of colloidal dispersions pack particles into an ordered 3D array.^{21,22} Our analysis sets an upper limit on the thickness of large single domain bandgap crystals possible via this synthesis route.

ACKNOWLEDGEMENTS

The present work was financially supported by the Department of Science and Technology, India under Project # 04DS026. The experimental support of Dr. S. L. Kamath and Prof. N. Venkataramani of Department of Metallurgical Engineering and Materials Science, IIT-Bombay and Prof. D. N. Singh of Department of Civil Engineering, IIT-Bombay is acknowledged. The authors thank Dr. Martin Murray of ICI and Dr. Richard Buscall of MSACT Consulting for stimulating discussions and for generous donation of dispersions. Dr. K. Takamura of BASF is also acknowledged for providing the styrene-butadiene dispersion.

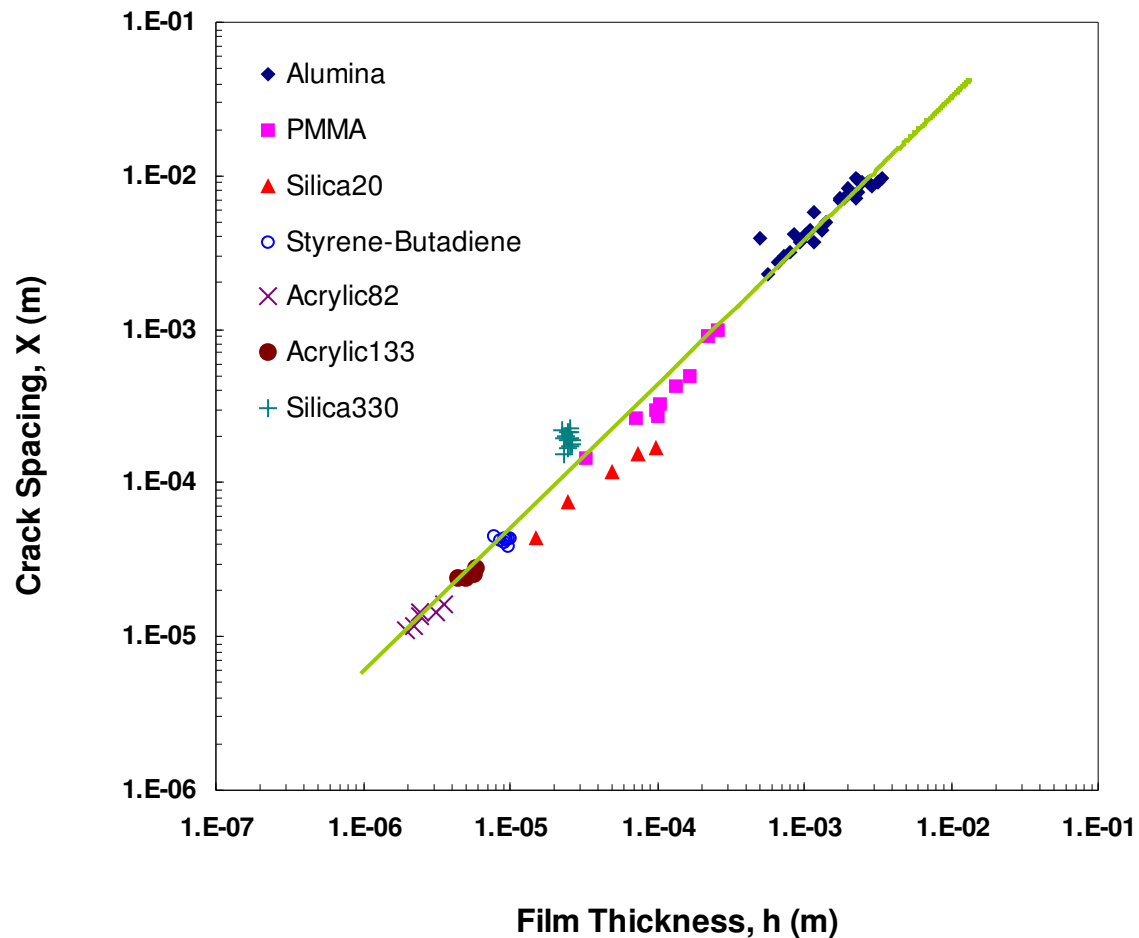


Figure 3.4: Variations in crack spacing with the film thickness. The data points are for films of alumina⁷ (\blacklozenge , $2R=13$ nm), PMMA³ (\blacksquare , $2R=95$ nm), silica⁴ (\blacktriangle , $2R=20$ nm), styrene-butadiene (\circ , $2R=250$ nm), acrylic82 (\times , $2R=82$ nm), acrylic133 (\bullet , $2R=133$ nm), silica330 ($+$, $2R=330$ nm).

REFERENCES

- [1] C. J. Brinker and G. W. Scherer. Sol-Gel Science: The Physics and Chemistry of Sol-Gel Processing. *Academic Press, Inc.: New York*, 1990.
- [2] A. F. Routh and W. B. Russel. A process model for latex film formation: Limiting regimes for individual driving forces. *Langmuir*, 15 (22): 7762-7773, 1999.
- [3] M. S. Tirumkudulu and W. B. Russel. Cracking in drying latex films. *Langmuir* 21: 4938-4948, 2005.
- [4] C. Allain and L. Limat. Regular patterns of cracks formed by directional drying of a colloidal suspension. *Phys. Rev. Lett.* 74(15): 2981-2984, 1995.
- [5] L. Pauchard, F. Parisse, and C. Allain. Influence of salt content on crack patterns formed through colloidal suspension desiccation. *Phys. Rev. E*, 59: 3737-3740, 1999.
- [6] H. Colina and S. Roux. Experimental model of cracking induced by drying shrinkage. *Eur. Phys. J. E*, 1: 189-194, 2000.
- [7] K. A. Shorlin, J. R. deBruyn, M. Graham, and S. W. Morris. Development and geometry of isotropic and directional shrinkage-crack patterns. *Phys. Rev. E*, 61: 6950-6957, 2000.
- [8] R. C. Chiu, T. J. Garino, and M. J. Cima. Drying of granular ceramic films: I Effect of processing variables on cracking behavior. *J. Am. Ceram. Soc.*, 76(9): 2257-2264, 1993a.
- [9] R. C. Chiu and M. J. Cima. Drying of granular ceramic films: II Drying stress and saturation uniformity. *J. Am. Ceram. Soc.*, 76(11): 2769-2777, 1993b.
- [10] P. A. Meakin. A simple model for elastic fractures in thin films. *Thin Solid Films*, 151: 165-190, (1987).

- [11] T. Skjeltorp and P. Meakin. Fracture in microsphere monolayers studied by experiment and computer simulation. *Nature*, 335 (29): 424-426, 1988.
- [12] W. P. Lee and A. F. Routh. Why do drying films crack? *Langmuir* 20: 9885-9888, 2004.
- [13] E. R. Dufresne, E. I. Corwin, N. A. Greenblatt, J. Ashmore, D. Y. Wang, A. D. Dinsmore, J. X. Cheng, X. S. Xie, J.W. Hutchinson, and D. A. Weitz. Flow and fracture in drying nanoparticle suspensions. *Phys. Rev. Lett.* 91 (22): (4501-1)-(4501-4), 2003.
- [14] H. J. Herman and S. Roux. Statistical Models for Fracture of Disordered Media. *North-Holland, Amsterdam*, 1990.
- [15] A. Griffith. The phenomenon of rupture and flow in solids. *Phil. Trans. Roy. Soc.* 221: 163-198, 1921.
- [16] The multiplying factor in Eq. (3.1) has been increased by a factor of two in arriving at Eq. (3.2) and (3.3).
- [17] The capillary pressure (P) in the solvent phase is related to the biaxial stress by
- $$P = -\frac{5}{4} \sigma .$$
- [18] W. Adamson and A. P. Gast, Physical Chemistry of Surfaces. *John Wiley & Sons, Inc.: New York*, 1997.
- [19] L. R. White. Capillary rise in powders. *J. Colloid Interface Sci.*, 90 (2): 536-538, 1982.
- [20] L. Uri, T. Walmann, L. Alberts, D. K. Dysthe, and J. Feder. Structure of plastically compacting granular packings. *Phys. Rev. E*, 73: (051301-1)- (051301-11), 2006.

- [21] E. G. Judith, J. Wijnhoven, and L. V. Willem. Preparation of photonic crystals made of air spheres in Titania. *Science* 281: 802-804, 1998.
- [22] Y. A. Vlasov, X.-Z. Bo, J. C. Sturm, and J. N. David. On-chip natural assembly of silicon photonic bandgap crystals. *Nature* 414: 289-293, 2001.

CRACKING IN DRYING COLLOIDAL

FILMS OF FLOCCULATED DISPERSIONS

Chapter 4

CRACKING IN DRYING COLLOIDAL FILMS OF FLOCCULATED DISPERSIONS[†]

ABSTRACT

Understanding the mechanism of cracking during drying of aqueous colloidal dispersions is important to prevent film failure. While most of the reported work has dealt with stable aqueous dispersions, few have focused on flocculated systems. The latter especially assumes importance as the role of particle packing on the mechanism of cracking is not understood. In this work, we study the cracking of colloidal films cast from flocculated aqueous dispersions of α -alumina. Here, the extent of flocculation is controlled by varying the pH of the dispersion and characterized in terms of final packing volume fraction of the dried film. The influence of varying close-packed volume fraction on critical cracking thickness and critical cracking stress is measured. The measurements are compared with the model predictions of Singh and Tirumkudulu¹ and good agreement is found between theory and experiments, suggesting that the model is universal and applies equally well to stable as well as flocculated systems.

[†] This work was carried out jointly with Laxman R. Bhosale and part of this chapter also appears in his Master's thesis.²

4.1 INTRODUCTION

Cracking of colloidal films has received considerable attention in the recent years due to its importance in many important applications such as paints, wet clays, ceramics, and coatings where cracking is highly undesirable. When a thin film of aqueous colloidal dispersion is applied on an impermeable substrate, water evaporates resulting in an increase in solid concentration. In stable dispersions, the strong interparticle repulsive forces disperse the particles against the tendency of the attractive forces to bring them together. Further evaporation causes particles to concentrate into a closed packed array³⁻⁶ accompanied with the development of stresses in the wet film.⁷ If the particles are soft, they deform and coalesce so as to close the pores whereas in case of hard particles, stresses are released by the nucleation and propagation of cracks.^{1,8}

One of the most important experimental study on cracking of colloidal films was reported by Chiu et al.⁹ who found that irrespective of particle size and rigidity, there exists a critical cracking thickness (CCT) below which films do not crack. This thickness was further found to increase with particle size. On the theoretical end, Tirumkudulu and Russel⁸ proposed a model based on Griffith's concept of energy balance between the elastic and surface energies to determine the critical stress at which a drying film cracks,

$$\frac{\sigma_c R}{2\gamma} = 0.1877 \left(\frac{M \phi_{rcp}}{N^2} \right)^{1/3} \left(\frac{G R}{2\gamma} \right)^{1/3} \quad (4.1)$$

Here, σ_c is the critical cracking stress (CCS) at which film cracks, R is the particle radius, ϕ_{rcp} is random close-packed volume fraction, γ is the solvent-air interfacial tension, M is the coordination number, $N \equiv (h/2R)$ is dimensionless film thickness and G is the shear modulus of particles. Man and Russel¹⁰ have also

emphasized the role of elastic energy in the nucleation and propagation of cracks although they use a different constitutive relation to predict the critical stress and thickness. Using scaling analysis, they showed that the Griffith's energy balance concept provides the lower bound i.e. the necessary condition for crack formation. They have further identified the role of flaws as the nucleation sites for crack initiations. Some of the recent work has also investigated the resulting crack spacing in drying dispersions.^{11,12} which is not the focus of this work.

A recent study by Singh and Tirumkudulu¹ reports the critical cracking thickness for a large number of stable aqueous dispersions. They identify two regimes for obtaining crack free films. For dispersions containing hard particles (*stress-limited* regime), the CCT increases with particle size as well as particle rigidity while for soft particles where the particles completely deform to close the pores (*strain-limited* regime), the critical thickness decreases with increasing particle rigidity but is independent of particle size. In the stress-limited regime, particles do not deform completely and the critical cracking thickness is obtained by equating the bulk stress in the film at maximum attainable capillary pressure to the critical stress for cracking. On the other hand, in the strain-limited regime, particles completely deform before capillary pressure reaches the maximum value. Here the critical cracking thickness is obtained by equating the bulk stress at maximum strain with the critical stress for cracking. The critical thickness for the stress-limited regime given by,

$$h_{\max} = 0.64 \left[\frac{GM \phi_{rcp} R^3}{2\gamma} \right]^{1/2} \left[\frac{2\gamma}{(-P_{\max}) R} \right]^{3/2} \quad (4.2)$$

agrees well with measurements over a wide range of particle sizes and particle shear moduli. Here, P_{max} is the maximum attainable capillary pressure and h_{max} is the critical cracking thickness. Further, the model also suggests that the cracking behavior is influenced by particles packing fraction in the drying film; a prediction yet to be verified.

We study the effect of flocculation on both the critical stress and the critical cracking thickness in drying films. Here, the interparticle stabilizing forces are weak and are overcome by the attractive van der Waals forces causing the particles to contact well before reaching random close packing volume fractions. An electrostatically stabilized dispersion can be flocculated either by adding electrolyte to the dispersion or by altering the pH to reduce the effective surface charge. In general, the particles agglomerate to form flocs that are open fractal structures (figure 4.1). As the water continues to evaporate, the flocs connect to form a percolating network that spans the entire thickness of the film. The network has a yield stress and the film consolidates when the capillary pressure exerted by the fluid interface at the top of the film exceeds the network strength.¹³ As the film consolidates and the particles rearrange to form stronger networks, the liquid either recedes into the porous packing when the capillary pressure reaches a maximum while still below the yield stress of the network or the film cracks under transverse tensile stresses generated due to the constraint imposed by the substrate to lateral shrinkage. The final packing volume fraction of the dried film is less than the random close packing fraction. Chiu et al.⁹ varied the degree of flocculation of alumina dispersion by adding salt (NaCl) and found that the CCT initially increases with salt concentration, passes through a maximum and then starts decreasing. The CCT was found to increase from 70 μm to $\sim 200 \mu\text{m}$ when the salt concentration was increased

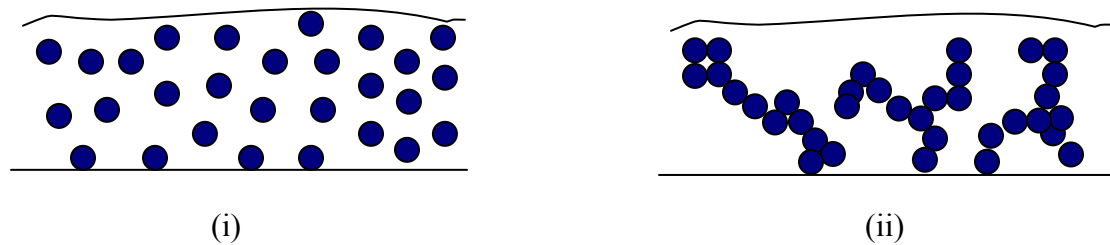


Figure 4.1: Schematic of a drying colloidal film of (i) stable and (ii) flocculated dispersion.

from zero to 100mM. They attributed the increase in CCT to the decrease in stabilizing electrostatic double layer forces that flocculate the particles and ultimately result in films with low green densities. On the other hand, Carreras et al.¹⁴ have recently shown that the measured CCT for films cast from stable alumina dispersions (pH~1.75) were three times higher than that obtained from flocculated suspensions (pH~9) in apparent contradiction to the earlier work of Chiu et al.⁹ Here the increase in CCT at low pH is attributed to the superior mechanical properties due to higher final solids concentration.

While the above experiments do suggest a clear influence of flocculation on cracking, the observed trends are contradictory. More importantly, it is not clear what mechanism controls cracking in flocculated systems. Further, if the Griffith's criterion is applicable to flocculated systems, how does one account for the network strength? We address these questions by varying the degree of flocculation of aqueous α -alumina dispersions over a wide range of pH and measuring the final packing volume fraction (ϕ_f), the critical stress at cracking for varying film thicknesses and the critical cracking thickness. We show that the model developed for cracking in stable dispersions predicts well the measurements if ϕ_{rcp} is replaced by ϕ_f while correcting for the number of nearest neighbors in contact. In other words, the model is universal and can predict equally well the cracking phenomenon in both stable as well as flocculated dispersions.

4.2 EXPERIMENTAL SECTION

High purity α -alumina (AKP-30) with average particle size of 335nm was obtained from Sigma-Aldrich[®]. Dilute dispersions with initial volume fraction of 13-20% were prepared by dispersing AKP-30 in deionized water. Because of extensive

ageing of dispersion in glass, the iso-electric point changes over time.¹⁵ To prevent this, all the dispersions were prepared in polypropylene bottles. Before preparing the dispersions, polypropylene bottles were thoroughly cleaned by soaking successively in 1M solution of HNO₃, distilled water, 1M solution of KOH and finally in distilled water, each for 12 hours. The pH of these dispersions was adjusted using analytical grade HNO₃ and KOH respectively. Before carrying out the measurements, all the dispersions were re-dispersed using cyclo-mixer and an ultrasonicator for 4-5 minutes. The final packing volume fraction of these dispersions at different pH was measured using glass capillaries, each having a size of 300 μm in diameter. Here, the original dispersion was allowed to dry from one end of the capillary tube under ambient conditions. The final packing volume fraction (ϕ_f) was calculated by noting the initial and the final length of the dispersion plug and then applying the mass balance relation. To further establish the authenticity of the data, we also measured the final packing volume fraction (ϕ_f) using a Goniometer (Dizidrop[®]). A small drop of the dispersion was put on a glass substrate kept on the platform of the instrument and was continuously imaged during the entire period of drying. Care was taken to ensure that the drop is symmetric and is fully focused during imaging. Finally the images taken at the start ($t = 0$) and at the end of the drying process were used to determine the profile of the drop. These profiles were then integrated to get the initial and the final volume of the drop. As the initial volume fraction is known, a volume balance gives the final packing volume fraction (ϕ_f). The data generated using this technique for two different pH values is also plotted along with the other data in Figure 4.2.

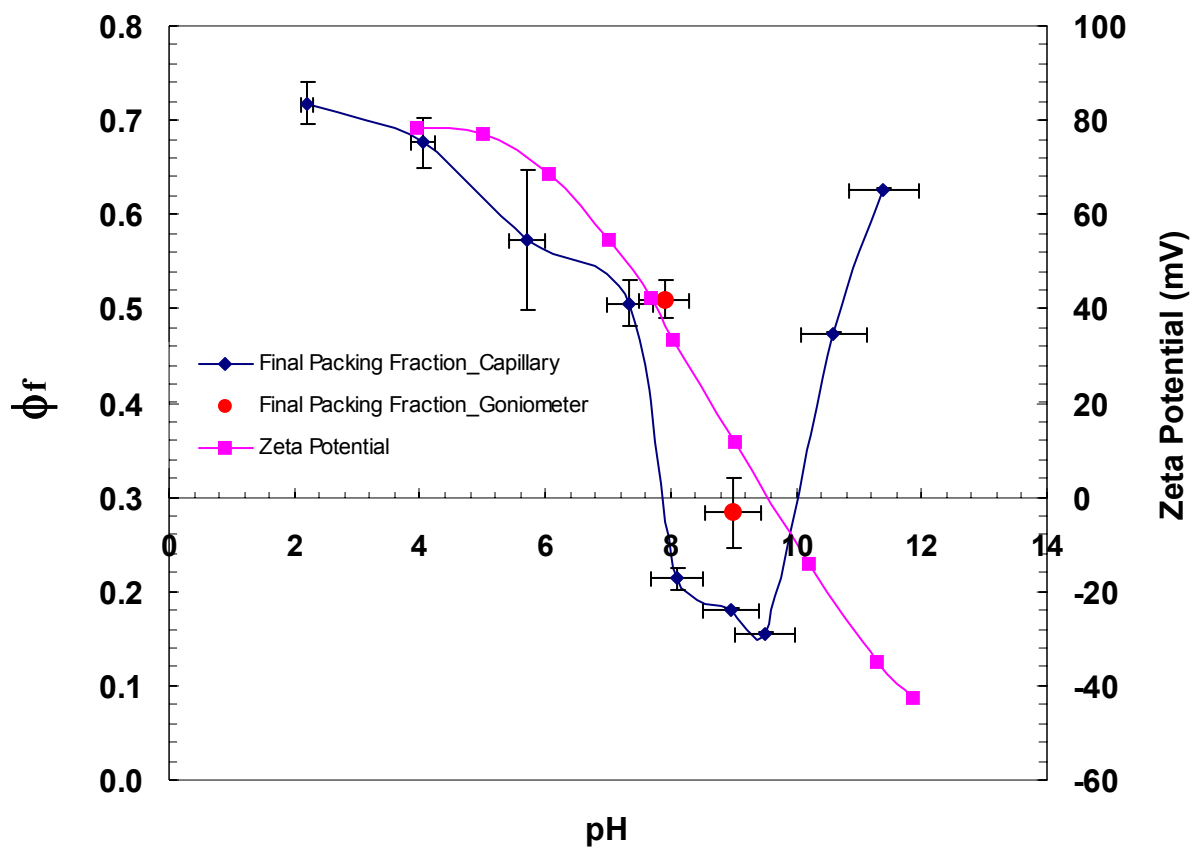


Figure 4.2: Variation of the final packing volume fraction (ϕ_f) and zeta potential as a function of pH for AKP-30 dispersion (26.1 °C and 43% RH). The zeta potential data is taken from Johnson et al.¹⁶ The solid lines are provided as a guide to the eye.

As can be seen, the two different measurement techniques essentially give the same values for the final packing volume fraction (ϕ_f) confirming that the data is reliable and the effect of shear stresses due to capillary walls is negligible.

The CCT measurements were performed over a temperature range of 25-28°C and a relative humidity of 35-40%. Thin films of the dispersions were cast on glass substrates by disbursing a small amount of liquid using a spin coater (slow rotation rate~20 rpm). Here, the spin coater was employed to spread the liquid uniformly over a fixed area so as to obtain a nearly circular film. Further, the thickness of the film was varied by disbursing increasing amounts of dispersion over the same area. After the films were cast, they were left to dry under ambient conditions. On complete drying, it was examined under an optical upright microscope (Olympus[®], BX-60) for cracks at varying magnifications. In case of dispersions that were highly flocculated and had very large critical thicknesses, the films were dried in open vials of square cross section (1.3 cm by 1.3 cm). Finally, the thickness profile of the dry film was obtained using a surface profilometer (Dektak-150[®]). It should be noted that in some cases the entire film was crack free which gave the lower limit for CCT.

The classical cantilever technique was employed to measure the stress in a drying film.¹⁷ Here, a thin layer of the dispersion was applied on a thin silicon wafer of dimensions 13mm (length) by 5mm (width) by 0.128 mm (thickness) and clamped on one side. A laser beam is reflected from the free end of the substrate and collected by a position sensitive detector (On-track[®]). The position of the detector is set in such a way that the reflected beam falls normally on the surface of the detector. The entire detector

assembly is mounted on an X-Y traverse so that the desired positioning can be done with precision. The position data (i.e. the x, y coordinate of the reflected beam) from the detector is directly fed to a computer. As the film dries, the tensile stresses in the drying film bend the substrate that consequently results in the movement of reflected beam on detector surface. Finally, the displacement of the reflected beam is related to the average tensile stress in the film. The details of the technique and the typical stress profiles can be found elsewhere.⁶

4.3 RESULTS AND DISCUSSION

The zeta potential measurements for AKP-30 dispersions at varying volume fractions by Johnson et al.¹⁶ are reproduced on the secondary y-axis of figure 4.2. The potential is high and positive at low pH and decreases with increasing pH. At pH~9.6, the potential passes through the iso-electric point and decreases further with pH to become large and negative. We quantify the extent of flocculation in a dried dispersion in terms of final packing volume fraction (ϕ_f).

The variation of final packing volume fraction with pH for the AKP-30 dispersion is plotted on the primary y-axis of figure 4.2. The measured volume fraction shows direct correspondence with the reported zeta potential measurement in that, at low pH, the final packing volume fraction is highest due to the higher surface charge. As the pH is increased, the surface charge decreases which results in a weaker stabilizing force. As the stabilizing repulsive forces between particles decrease, the dispersion becomes unstable and leads to particle flocculation. This is evident from lower values of final packing volume fraction as we increase the pH. At a pH of ~9.6 (iso-electric point), the charges at

the surface are completely neutralized and there are no stabilizing forces. As expected, the final packing volume fraction is the lowest, $\phi_f \sim 0.16$ at this pH. The low values of ϕ_f close to the iso-electric point are not entirely surprising since it is well known that the gelation volume fraction at iso-electric point for similar systems is approximately 0.14.¹⁸ With further increase in pH the particle surface acquires negative charge resulting in a greater stability of the dispersion. This is again evident from higher values of final packing volume fraction at high pH.

In figure 4.3, the experimentally measured CCTs are compared with the model of Singh and Tirumkudulu¹ over almost the entire range of pH values. The measured CCT (filled squares) initially decreases slightly as the pH is increased from ~ 4 to 6. With the further increase in pH from 6 to ~ 10 , there is a sharp increase in the CCT values with the maximum observed at a pH of ~ 10 . Finally, the measured CCT is found to decrease as pH is further increased from 10 to ~ 12 . The solid line in figure 4.3 is the prediction by the model of Singh and Tirumkudulu.¹ As per the model, the critical cracking thickness depends on the value of the maximum capillary pressure ($-P_{\max}$) (equation (4.2)).

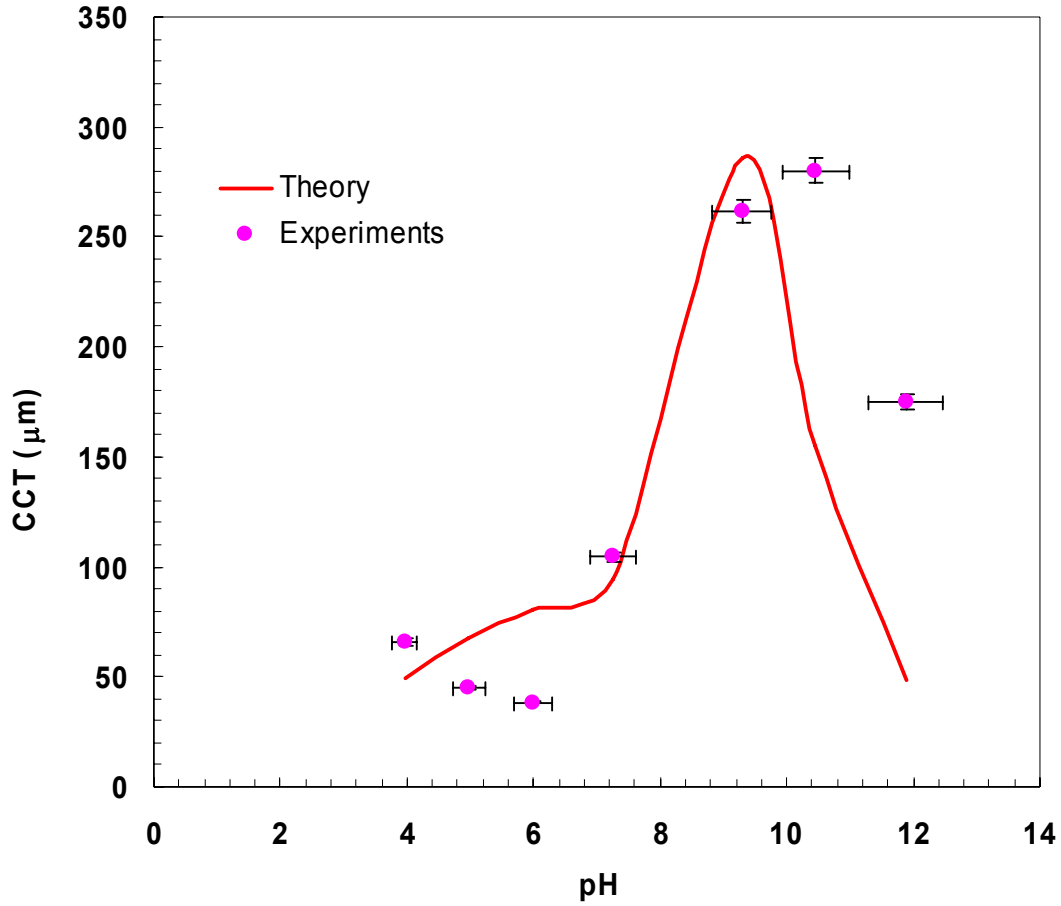


Figure 4.3: Comparison of measured critical cracking thickness (CCT) with the model of Singh and Tirumkudulu¹ at different pH values. Further, the values for ϕ_f and M at different pH values are; [(pH, ϕ_f , M)=(3.97, 0.66, 6.96), (4.98, 0.61, 6.18), (6, 0.56, 5.12), (7.25, 0.52, 4.90), (9.3, 0.18, 1.03), (10.46, 0.40, 3.82) and (11.88, 0.68, 7.02)] respectively. A contact angle of 35° was assumed.²⁷

However, the maximum capillary pressure itself is a function of final packing volume fraction and the wetting angle^{1,19}

$$\frac{(-P_{\max})R}{2\gamma} = \frac{3}{2} \cos \theta \frac{\phi_f}{1 - \phi_f}. \quad (4.3)$$

On replacing the above dimensionless capillary pressure in (4.2), the dependence of CCT on final packing volume fraction ϕ_f becomes

$$h_{\max} = 0.64 \left[\frac{4GM R^3 (1 - \phi_f)^3}{27 \gamma \cos^3 \theta (\phi_f)^2} \right]^{1/2} \quad (4.4)$$

The model clearly predicts an increase in CCT with decrease in final packing volume fraction ϕ_f . This is because a decrease in capillary pressure due to the lower final packing fraction results in lower stored elastic energy in the drying film. Consequently, the film cracks at a greater thickness to equal the increase in the surface energy. The model prediction compares fairly well against the measured CCTs in that the model captures the peak close to the iso-electric point and the subsequent decrease at higher pH values. The number of contacting neighbors (M) is calculated by extrapolating the data from Uri et al.²⁰ who have reported the coordination number as a function of final packing volume fraction for a large number of particle systems. The slight shift in the predicted peak compared to the measured values can be attributed to small errors in pH measurements (about ± 0.25 pH). At low pH (<6) however, the experiments exhibit a reverse trend compared to the model predictions. One plausible reason could be the high solubility of alumina at low pH²¹ that could lead to the precipitation of alumina at particle contacts on complete drying. This would in turn lead to strengthening of the network without significantly altering the final packing volume

fraction. Such a phenomena is not accounted for in our model and could be the cause for the observed discrepancy. Chiu et al.⁹ also report higher CCT below pH 2 and have attributed this to the higher solubility of alumina at low pH which explains the difference in the observed trend with respect to those of Carreras et al.¹⁴ Nevertheless, our model captures quite well the measured trend for the remaining pH values. The above results point to the importance of capillary pressure and its role in the cracking of drying films of colloidal dispersions.

Figure 4.4 plots the dimensionless critical cracking stress against the dimensionless characteristic scale ($M \phi_m / N^2$) for dispersions with pH of 3.3, 6.5, 7.8, 10.0 and 11.1. Here, the average thickness of the film (h) is used to calculate the dimensionless film thickness ($N \equiv \frac{h}{2R}$). It should be noted that the transverse flow⁶ generated by high capillary pressures at the film edges leads to slight inhomogeneties in the thickness over the film. Thus although the average thickness may be less than the CCT, the actual thickness over certain regions of the film would be well above CCT.⁸ The solid line in figure 4.4 is a fit from the model of Tirumkudulu and Russel (4.1) with an exponent of 1/3.²² As can be seen, the experiments are in good agreement with the model of Tirumkudulu and Russel.⁸ These results are a clear proof that the model developed to explain cracking in the stable dispersions is equally capable of predicting the cracking behavior in flocculated systems. But it is important to note that the model is incapable of predicting the final volume fraction at which a given drying film will crack, which is still an unsolved problem. However, once the final volume fraction of the dry film is known, the critical stress and thickness variation with respect to other system parameters (shear modulus, particle radius etc.) is captured well by the model.

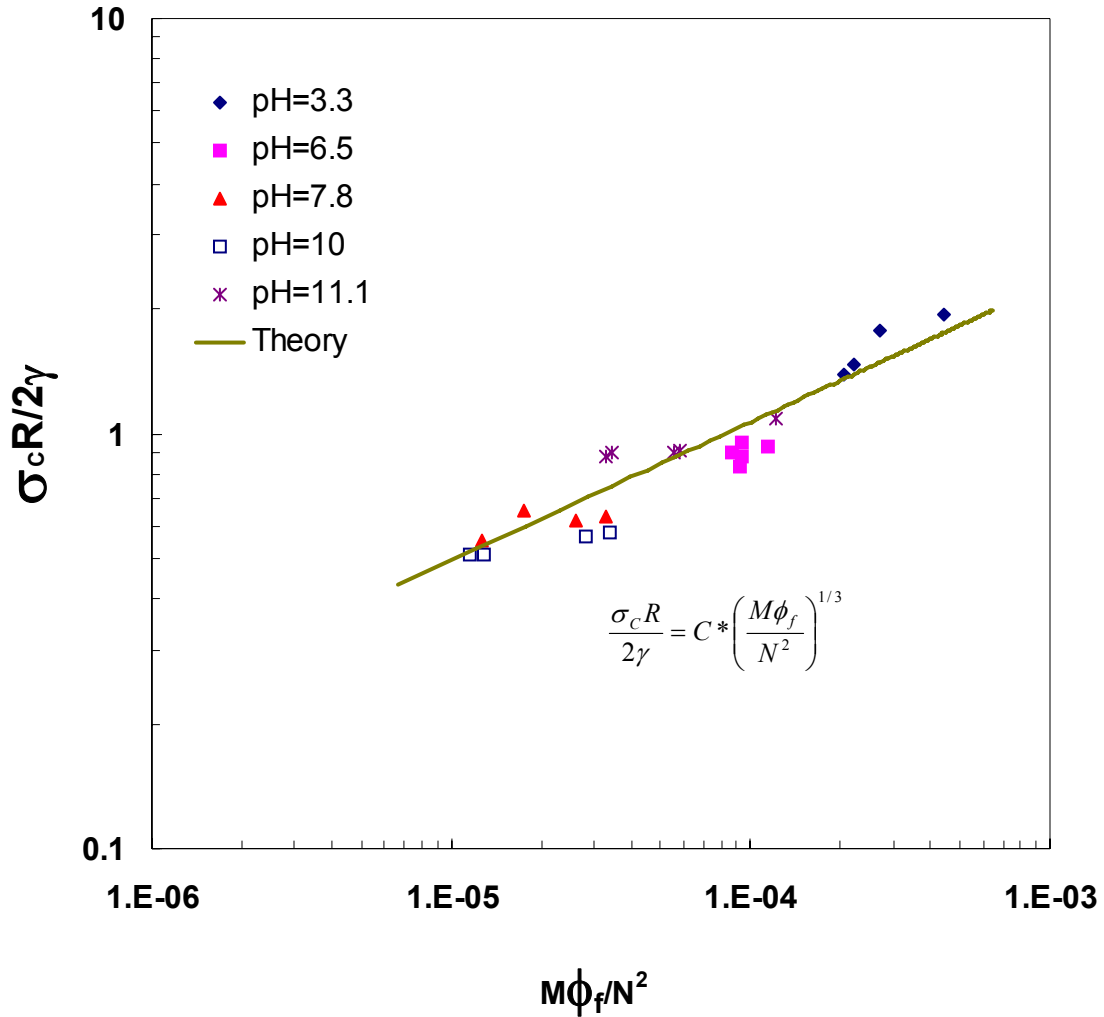


Figure 4.4: Plot of measured dimensionless critical cracking stress ($\sigma_c R / 2\gamma$) vs. the dimensionless characteristic scale ($M\phi_f / N^2$). The data points are for films of AKP-30 dispersion with varying pH. The solid line is a power law fit with an exponent of 1/3. The values for ϕ_f and M at different pH are; [(pH, ϕ_f , M)=(3.3, 0.69, 7.2), (6.5, 0.55, 5.23), (7.8, 0.35, 3.3), (10, 0.29, 2.76) and (11.1, 0.58, 5.51)] respectively.

4.4 CONCLUSION

The cracking behavior of a model flocculated aqueous dispersions over a broad range of pH values is investigated. The measured values of critical stress and thickness in both the stable and flocculated regimes were compared with the prediction of the existing model¹ for stable dispersion. While good agreement was found for $\text{pH} > 6$, some discrepancy was observed in the critical thickness at lower pH. This study highlights the importance of capillary pressure in the cracking of drying films of colloidal dispersions and demonstrates how the cracking characteristics can be drastically altered by merely varying the final packing fraction. The proposed model provides a complete theoretical framework to predict the cracking characteristics of drying colloidal dispersions and could form the basis of efficient design of coating formulations. One such application is the tape-casting technology where thin flat ceramic sheets are produced for a variety of applications such as multilayered capacitors, multilayered ceramic packages, membranes for fuel cell, etc²³⁻²⁶ and the primary concern is to obtain a film with no defects or cracks. Our study can help in optimizing the system variables to control the cracking of these films.

ACKNOWLEDGEMENT

This work was financially supported by the Department of Science and Technology, India, and IIT Bombay research grant. The authors thank Dr. Martin Murray of AkzoNobel for stimulating discussions and for providing AKP-30 particles.

REFERENCES

- [1] K. B. Singh and M. S. Tirumkudulu. Cracking in drying colloidal films. *Phys. Rev. Lett.*, 98: 218302(1)-218302(4), 2007.
- [2] L. R. Bhosale. Cracking in Flocculated Dispersions. Master's thesis, Indian Institute of Technology-Bombay, 2006.
- [3] D. P. Sheetz. Formation of films by drying of latex. *J. Appl. Polym. Sci.*, 9: 3759-3773, 1965.
- [4] A. F. Routh and W. B. Russel. Horizontal drying fronts during solvent evaporation from latex films. *AIChE J.*, 44 (9): 2088-2098, 1998.
- [5] A. F. Routh and W. B. Russel. A process model for latex film formation: Limiting regimes for individual driving forces. *Langmuir*, 15 (22): 7762-7773, 1999.
- [6] M. S. Tirumkudulu and W. B. Russel. Role of capillary stresses in film formation. *Langmuir*, 20 (7): 2947-2961, 2004.
- [7] M. A. Winnik. Latex film formation. *Curr. Opin. Colloid Interface Sci.*, 2 (2): 192-199, 1997.
- [8] M. S. Tirumkudulu and W. B. Russel. Cracking in drying latex films. *Langmuir*, 21 (11): 4938-4948, 2005.
- [9] R. C. Chiu, T. J. Garino, and M. J. Cima. Drying of granular ceramic films: I Effect of processing variables on cracking behavior. *J. Am. Ceram. Soc.*, 76(9): 2257-2264, 1993b.
- [10] W. Man and W. B. Russel. Direct measurements of critical stresses and cracking in thin films of colloid dispersions. *Phys. Rev. Lett.*, 100: 198302(1)- 198302(4), 2007.

- [11] W. P. Lee and A. F. Routh. Why do drying films crack? *Langmuir*, 20(23): 9885-9888, 2004.
- [12] C. Allain and L. Limat. Regular patterns of cracks formed by directional drying of a colloidal suspension. *Phys. Rev. Lett.* 74(15): 2981-2984, 1995.
- [13] R. Buscall and L. R. White. The consolidation of concentrated suspensions: 1. The theory of sedimentation. *J. Chem. Soc. Faraday Trans.*, 83: 873–891, 1987.
- [14] C. F. Carreras, D. E. Dunstan, and G. V. Franks. Avoiding mud cracks during drying of thin films from aqueous colloidal suspensions. *J. Colloid Interface Sci.*, 313: 160-168, 2007.
- [15] D. N. Furlong, P. A. Freeman, and A. C. M. Lau. The adsorption of soluble silica at solid-aqueous solution interfaces I. Leaching from glass-An electro-kinetic study. *J. Colloid Interface Sci.*, 80(1): 20-31, 1981.
- [16] S. B. Johnson, A. S. Russel, and P. Scales. Volume fraction effects in shear rheology and electro-acoustic studies of concentrated alumina and kaolin suspensions, *Colloid and Surfaces*, 141: 119-130, 1998.
- [17] C. Petersen, C. Heldmann, and D. Johannsmann. Internal stresses during film formation of polymer lattices. *Langmuir*, 15: 7745-7751, 1999.
- [18] C. M. Glenn and C.F. Zukoski. Shear and compressive rheology of aggregated alumina suspensions. *AIChE*, 43 (7): 1700-1708, 1997.
- [19] L. R. White. Capillary rise in powders, *J. Colloid Interface Sci.*, 90 (2): 536-538, 1982.

- [20] L. Uri, T. Walmann, L. Alberts, D. K. Dysthe, and J. Feder. Structure of plastically compacting granular packings. *Phys. Rev. E*, 73: (051301-1)-(051301-11), 2006.
- [21] F. B. Charles Jr. and E. M. Robert. The hydrolysis of cations. *John Wiley & Sons, Inc.*, 1976.
- [22] As in case of Singh and Tirumkudulu¹ the coefficient in equation (4.1) was increased by a factor of 2 while comparing this equation with the experimental results
- [23] D. Hotza and P. Greil. Review: aqueous tape casting of ceramic powders. *Mat. Sci. and Engg.*, A202: 206-217, 1995.
- [24] J. Xiang, Z. Xie, and Y. Huang. Processing of Al₂O₃ sheets by the gel-tape-casting process. *Ceramics International*, 28: 17-22, 2002.
- [25] R. E. Mistler. Tape casting: past, present, potential. *Am. Cera. Soc. Bull.*, 77(10): 82-86, 1998.
- [26] M. Descamps, M. Mascart, B. Thierry, and D. Leger. How to control cracking of tape-cast sheets. *Am. Cera. Soc. Bull.*, 74: 89-92, 1995.
- [27] W. Souheng. Polymer interface and adhesion. *Marcel Dekkar*, 1982.

FILM FORMATION IN LATEX
BLENDS: THEORY AND
EXPERIMENTS

Chapter 5

FILM FORMATION IN LATEX

BLENDS: THEORY AND EXPERIMENTS

ABSTRACT

Volatile organic compounds (VOCs) in the traditional paint and coating formulations are an important health and environmental concern and current formulations are increasingly moving towards water-based dispersions. However, even within the water-based systems, small quantities of organic solvents are used to promote particle coalescence. One route to achieving this goal has been to use mixtures of soft and hard particles, also known as latex blends. We investigate the drying of colloidal films containing mixtures of silica and acrylic particles. Since both the particles deform only slightly at room temperature, this work investigates the cracking behavior of films containing elastic particles of two different elastic moduli. We extend an existing model for the stress versus strain relation for identical particles in a colloidal film to that containing a mixture of equal-sized hard and soft elastic spheres while accounting for the non-affine deformation. A transition from soft to rigid-like behavior is observed beyond a critical hard particle volume fraction ratio that matches with published results obtained from computer simulations. The model predictions are validated with extensive experimental data on the critical stress and critical cracking thickness for various ratios of hard and soft particle volume fraction.

5.1 INTRODUCTION

Adverse impact on health and environment are forcing the paint and coating manufacturers to replace the volatile organic compounds in traditional formulations with water-based formulations, also referred to as Latex. However, even the water-based formulations are not completely organic solvent free and contain small amounts of organic compounds to plasticize polymer particles so that a balance between film forming ability and the mechanical properties of the final film can be achieved under ambient conditions.¹ For example, polymers with low glass transition temperature (T_g) will easily film form at room temperature but the final film will be tacky with poor mechanical properties. On the other hand, polymers with high T_g have good elastic properties but the final film suffers with the problem of cracking.^{2,3}

To achieve both, good film forming ability and excellent mechanical properties from aqueous dispersions without the use of volatile compounds, several approaches have been explored. One of these is the use of core/shell latex particles where the core of the particle is a high T_g polymer whereas the shell is a low T_g film-forming polymer. When particles come in contact, the shell coalesces to form a continuous phase whereas the core provides the mechanical strength to the final film. The other approach, which forms the subject matter of this study, is the use of latex blends containing soft (low T_g) and hard (high T_g) polymer particles. In these blends, soft particles coalesce to fill the voids and the hard ones give mechanical strength to the final film.

While most of the existing literature on the film formation and cracking mechanism in drying colloidal films consider monodisperse spheres with identical mechanical properties,^{4,5} a few have focused on latex blends. Winnik and Feng¹ experimented with a latex blend containing a high- T_g polymer [poly(methyl methacrylate), PMMA] and a copolymer of butyl methacrylate and butyl acrylate [P(BMA-co-BA)] with $T_g \leq 10^\circ\text{C}$, and found that the films dry at a slower rate than films cast from dispersions containing only one type of particle. They observed that the rate of drying passes through a

minimum with increasing hard particle volume fraction with the minimum occurring at a value of $\alpha = 0.56$, where α is the ratio of hard particles volume to the total solid volume. As expected, the ratio of hard to total solid volume was found to strongly affect the film formation behavior of the blend. Martinez and Lewis⁶ have reported the film formation in blends of latex and silica. In this study, the film shape evolution and the stress development during film formation were studied for a blend of acrylic latex (particle size of 330 nm and T_g of -6°C) and silica (particle size of 570 nm). It was found that blends with $\alpha < 0.4$ behaved like pure latex films. However, a marked transition from a deformable to rigid-like response was observed as the silica volume fraction increased beyond this value (i.e. $\alpha > 0.4$). They measured the stress of the drying film using the well known cantilever technique and found that the stress peak became sharper as the silica volume fraction in the blend was increased.

Lepizzera et al.² have studied the influence of glass transition temperature and relative particle loading on film forming ability and mechanical properties of latex blend films. The hard latex in this study was synthesized from PMMA with particle size and particle glass transition temperature as 210 nm and 105°C respectively. Soft particles were based on methyl methacrylate-butyl acrylate-acrylic acid with a size ranging from 55 to 210 nm and a T_g ranging from -1 to 18°C . It was found that for blends with soft particle T_g less than 0°C , the maximum weight fraction of hard latex for obtaining crack-free transparent films is constant and equal to $\alpha = 0.55$ irrespective of soft particle T_g . On the other hand, an inverse proportionality between hard particle weight fraction and soft particle T_g was observed for films with soft particle T_g greater than 0°C . Further, irrespective of soft particle T_g , all films crack for $\alpha > 0.55$. Some of the studies have also considered the effect of particle size and size ratio on film formation behavior of latex blends. Colombini et al.⁷ found that higher the soft/hard particle size ratio, the film cracks at lower values of α . The size of the dispersed hard phase also affects the viscoelastic film properties with smaller particles giving mechanically strong films. Tzitzinou and Keddie⁸ have also shown the influence of size ratio on film

formation behavior. Depending on the concentration of small particles, they can form a connecting network around the larger ones leading to a continuous phase inversion. Feng et al.⁹ have reported the effect of particle size, glass transition temperature, evaporation rate and soft particle volume fraction ratio on morphology and transparency of blend films. At high evaporation rates, they obtained turbid films which was attributed to the insufficient time available for the soft particles to deform and close the void spaces in the film. The turbidity of the film is caused by light scattering from defects that are comparable or larger than the wavelength of light. Turbid films were also obtained when the hard particles aggregated and a nonuniform distribution of hard and soft particles was obtained. On the other hand, decreasing the T_g or increasing the fraction of soft particles improved the transparency of the film. They conclude that the size of the soft particles plays a minor role in determining the transparency of the film.

On the theoretical end, Jagota and Scherer^{10,11} have studied the sintering rates and viscosities of two and three-dimensional random packing of hard and soft spheres of identical size using a numerical model. The particle packing was replaced by a network of points (that represent the center of particles) and links (that represent the contacts between the particles). Further, depending on the type of interaction, the links were either represented by springs or by dashpots. Finally the deformation of this network was studied to investigate the sintering and deformation of randomly packed spheres. Here, two different cases were considered. In the first (bonded) case, the contact between hard particles resist all the relative velocities as well as spins. In second (sliding) case, the contacts between hard particles can slide and bend but resist interpenetration. In their analysis, force and moment balance equations were solved at each network point assuming that the system is in equilibrium. It was found that the transition from soft to hardlike behavior occurs at a rigidity threshold which coincides with the percolation threshold ($\alpha = 0.32$) for the bonded case whereas in sliding case, the rigidity threshold was much higher ($\alpha \sim 1$) than the percolation threshold.

We present both the theoretical and experimental investigations of latex blends con-

taining equal sized elastic spheres of two different shear moduli. The model developed here extends the stress versus strain relation of Routh and Russel⁴ for a drying colloidal film containing identical spherical particles to that containing a latex blend. They considered the viscoelastic deformation of a pair of identical particles due to contact and interfacial forces and related the strain at the particle level to these forces. Next, they volume averaged the forces over all orientations to arrive at the macroscopic stress versus strain relationship for a drying film. The model has been successful in predicting not only the stress profile in drying films of both film forming and non film forming dispersions,¹² but also in predicting the cracking mechanism in the latter.^{3,5}

In the present work, a mathematical model for film formation in latex blends has been developed. Here, we have employed the concepts developed for monodisperse systems and derived the constitutive equation for a blend with soft and hard particles. We account for the non-affine deformation in the film and predict critical cracking stress and critical cracking thickness (CCT) that are validated with measurements on a blend of acrylic and silica particles.

5.2 MODEL

Consider a drying colloidal film containing equal sized spherical particles of two different shear moduli. When the particles reach close packing, three different types of contacts between a pair of particles are possible, namely, hard sphere-hard sphere (HH) contact, hard sphere-soft sphere (HS) contact, and soft sphere-soft sphere (SS) contact. The HH and SS contacts for the deformation of a two-particle system have been solved by Routh and Russel.⁴ They assumed that the particle pair is subjected to contact forces, \mathbf{F} , that act along the line joining the centers of spheres and the particles deform such that they remain sections of spheres (figure 5.1(c)) throughout the deformation. For the HS contact, we consider a pair of contacting hard and soft elastic spherical particles of equal

size acted upon by contact forces, \mathbf{F} , again, acting along the line joining their centers but we assume that the hard sphere is rigid while the soft sphere deforms elastically under the applied forces. Therefore, on complete deformation, the soft sphere engulfs the hard sphere. Figures 5.1(a)-5.1(d) present schematics of the hard-soft particle pair at various stages of deformation.

The strain at the particle pair level is defined as the ratio of the change in the inter-particle center to center distance, at any instant to that at complete deformation,

$$\epsilon_{HS} = \frac{\text{change in inter-particle distance (at time t)}}{\text{change in inter-particle distance at complete deformation}} \quad (5.1)$$

For the present case,

$$\epsilon_{HS} = \frac{2R_0 - d_t}{2R_0 - d_f} \quad (5.2)$$

where $d_f = (\sqrt[3]{2} - 1)R_0$. Here, R_0 is the original radius of the two particles, R_t is the radius of the soft sphere after the onset of deformation, d_t is the distance between the centers of the hard and soft sphere during deformation while d_f is the distance between the spheres at complete deformation. The variable z' denotes the axial distance between the center of the soft sphere and the vertical plane passing through the intersection of the two spheres. The first step towards obtaining the stress-strain relation is to relate the radius of the expanding soft sphere to its original radius and the particle strain. The calculation of R_t/R_0 involves volume conservation equation and is presented in Appendix A. Since, the value of R_t/R_0 is known at $\epsilon_{HS} = 0$, (5.35) is successively differentiated with respect to ϵ_{HS} to obtain a Taylor series expansion upto $O(\epsilon_{HS}^2)$,

$$\frac{R_t}{R_0} = 1 + \beta\epsilon_{HS}^2 + O(\epsilon_{HS}^3) \text{ where } \beta \equiv \frac{(3 - \sqrt[3]{2})^2}{8} \quad (5.3)$$

As mentioned earlier, the goal is to relate the strain at the particle pair level to the forces acting on the pair. During the deformation, it is assumed that the surface of the soft sphere deforms radially while the surface of the hard sphere translates in the axial direction. Consequently, the surface displacement vector for the soft sphere is given by,

$$\vec{S}_1 = (R_t - R_0) \hat{n}_1 + g(R_0, \epsilon_{HS}) \hat{e}_z$$

while that for the hard sphere is given by,

$$\vec{S}_2 = -(2R_0 - d_t)\hat{e}_z$$

where, \hat{n}_1 and \hat{n}_2 (see figure 5.1(c)) are unit vectors perpendicular to the surface of the soft and hard sphere respectively while \hat{e}_z is the unit vector in the z- direction. The function, $g(R_0, \epsilon_{HS})$, is introduced to ensure global incompressibility condition. Then, the strain over the volume of the particle pair is given by (Appendix A),

$$\begin{aligned} \int_V \vec{\epsilon}_{HS} dV &= \int_V \frac{1}{2} (\vec{\nabla} \vec{S} + \vec{\nabla} \vec{S}^T) = \int_A \frac{1}{2} (\hat{n} \vec{S} + \vec{S} \hat{n}) dA \\ &= \frac{4}{3} \pi R_0^3 \beta \epsilon_{HS}^2 (\vec{I} - 3\hat{e}_z \hat{e}_z) \end{aligned} \quad (5.4)$$

Since the volume of each sphere is $\frac{4}{3} \pi R_0^3$, the volume averaged strain over the two particles is

$$\langle \vec{\epsilon}_{HS} \rangle = \frac{\beta}{2} \epsilon_{HS}^2 (\vec{I} - 3\hat{e}_z \hat{e}_z) \quad (5.5)$$

Next, we determine the volume averaged stress on the particle pair. The volume integral of stress over the particle pair can be transformed to a surface integral by invoking the Gauss's theorem,

$$\int_V \vec{\sigma} dV = \int_A \hat{n} \cdot \vec{\sigma} \vec{x} dA \quad (5.6)$$

where \hat{n} is the unit normal from the surfaces of both particles and \vec{x} is the position vector. Since we neglect van der Waals force and interfacial tension, only the inter-particle contact force contributes to stress,

$$\hat{n} \cdot \vec{\sigma} = -P_0 \hat{n} \cdot \vec{I} + \frac{F}{2\pi R_t} \delta(z + R_t) \hat{e}_z - \frac{F}{2\pi R_0} \delta(z - d_t - R_0) \hat{e}_z \quad (5.7)$$

where $\delta(z)$ is the Dirac-Delta function and P_0 is the pressure in the surrounding fluid.

On substituting (5.7) in (5.6), we have

$$\int_V \vec{\sigma}_{HS} dV = - \int_{A_1+A_2} \hat{n} P_0 \vec{x} dA + \int_{A_1} \frac{F \delta(z + R_t)}{2\pi R_t} \hat{e}_z (r \hat{e}_r + z \hat{e}_z) dA \quad (5.8)$$

$$\begin{aligned} & - \int_{A_2} \frac{F \delta(z - d_t - R_0)}{2\pi R_0} \hat{e}_z (r \hat{e}_r + z \hat{e}_z) dA \\ & = -\frac{8}{3} \pi R_0^3 P_0 \vec{I} - 4F R_0 \left(1 - \sqrt{\frac{\beta}{2}} \epsilon_{HS} \right) \hat{e}_z \hat{e}_z \end{aligned} \quad (5.9)$$

where A_1 and A_2 represent surface areas of soft and hard surface respectively (see Appendix B). The stress is then averaged over the two spheres to obtain the volume averaged quantity,

$$\langle \vec{\sigma}_{HS} \rangle = \frac{1}{V} \int_V \vec{\sigma}_{HS} dV = -P_0 \vec{I} - \frac{3F}{2\pi R_0^2} \left(1 - \sqrt{\frac{\beta}{2}} \epsilon_{HS} \right) \hat{e}_z \hat{e}_z \quad (5.10)$$

For the particle pair deforming under the contacting force, the deviatoric stress $\langle \vec{\sigma}_{HS} \rangle$ and the strain $\langle \vec{\epsilon}_{HS} \rangle$ are related to stress relaxation modulus of the material by

$$\langle \vec{\tau}_{HS} \rangle = 2 \int_{-\infty}^t G(t-t') \frac{d \langle \vec{\epsilon}_{HS} \rangle}{dt'} dt' \quad (5.11)$$

The deviatoric stress tensor is related to the total stress, $\langle \vec{\sigma}_{HS} \rangle$ and the isotropic pressure P as

$$\langle \vec{\sigma}_{HS} \rangle = \langle \vec{\tau}_{HS} \rangle - \langle P \rangle \vec{I} \quad (5.12)$$

where

$$\begin{aligned} \langle P \rangle &= P_0 + \frac{F}{2\pi R_0^2} \left(1 - \sqrt{\frac{\beta}{2}} \epsilon_{HS} \right), \text{ and} \\ \langle \vec{\tau}_{HS} \rangle &= \frac{F}{2\pi R_0^2} \left(1 - \sqrt{\frac{\beta}{2}} \epsilon_{HS} \right) \left(\vec{I} - 3\hat{e}_z \hat{e}_z \right). \end{aligned}$$

On substituting the averaged deviatoric stress and strain tensor in (5.9), the contact force is related to the particle strain to $O(\epsilon_{HS}^2)$,

$$F = \frac{4\pi R_0^2}{3} \beta \int_{-\infty}^t G(t-t') \frac{d}{dt'} (\epsilon_{HS}^2) dt' \quad (5.13)$$

Note that the trace of the volume averaged stress gives the average isotropic pressure in the particle as well as the equation governing the viscoelastic deformation of two spheres (5.13).

5.2.1 Non-affine deformation

Recall that Routh and Russel⁴ derived the stress-strain relation for a film containing monodisperse identical spheres by assuming affine deformation, where the strain at the particle level is the same as that at the macroscopic level. However, for a latex blend containing equal sized hard and soft spheres, the strain at the particle pair level will depend on the moduli of the interacting particles and will in general be different from that at macroscopic level. Next, we account for the non-affinity by assuming that the strain at the particle pair level for the three types of interactions differs from macroscopic strain by a function that, at lower order, is linear in macroscopic strain,

$$\langle \vec{\epsilon}_{SS} \rangle - \langle \vec{\epsilon} \rangle = a \langle \vec{\epsilon} \rangle, \quad (5.14)$$

$$\langle \vec{\epsilon}_{HH} \rangle - \langle \vec{\epsilon} \rangle = b \langle \vec{\epsilon} \rangle, \quad (5.15)$$

$$\langle \vec{\epsilon}_{HS} \rangle - \langle \vec{\epsilon} \rangle = c \langle \vec{\epsilon} \rangle, \quad (5.16)$$

Here $\langle \vec{\epsilon} \rangle$ is the macroscopic strain tensor and $\langle \vec{\epsilon}_{SS} \rangle$, $\langle \vec{\epsilon}_{HH} \rangle$ and $\langle \vec{\epsilon}_{HS} \rangle$ are respectively the strain tensors at the particle pair level for soft-soft, hard-hard and hard-soft interactions. If the fraction of hard particles (of total particles) is α , then the probability of finding a pair of hard-hard particles in a representative volume is α^2 , a pair of soft-soft particles is $(1 - \alpha)^2$ and a pair of hard-soft particles, $2\alpha(1 - \alpha)$,

$$\alpha^2 \langle \vec{\epsilon}_{HH} \rangle + (1 - \alpha)^2 \langle \vec{\epsilon}_{SS} \rangle + 2\alpha(1 - \alpha) \langle \vec{\epsilon}_{HS} \rangle = \langle \vec{\epsilon} \rangle \quad (5.17)$$

The constraint equation is therefore

$$a(1 - \alpha)^2 + b\alpha^2 + 2c\alpha(1 - \alpha) = 0 \quad (5.18)$$

5.2.2 Orientational average stress-strain relation

We focus on a single particle in the packing and integrate over the configuration of its neighbors to obtain the volume averaged macroscopic stress,⁴

$$\langle \vec{\sigma} \rangle = \frac{1}{V} \int_V \vec{\sigma} dV = \frac{1}{V} \left\{ \sum_{\text{contacts}} \vec{F} \vec{R} - \int_V P_0 \vec{I} dV \right\} \quad (5.19)$$

where, $\vec{\sigma}$ is the macroscopic stress in a representative volume containing the particles, \sum represents the contribution from all its contacting neighbors, P_0 is the pressure in the liquid and \vec{R} is the position vector for the contacting forces (figure 5.1(d)). The averaged stress (in indicial notation) can be rewritten to highlight the contribution from the two phases,

$$\langle \sigma_{ij} \rangle = \underbrace{-(1-\phi)P_0\delta_{ij}}_{\text{liquid}} - \underbrace{\left\{ \phi P_0\delta_{ij} + \frac{1}{V} \sum_n \vec{F}_i^n \vec{R}_j^n \right\}}_{\text{solid}} \quad (5.20)$$

Since the stress generated in the solid phase arises from all possible interaction, we have

$$\sigma_{ij} = -(1-\phi)P_0 - \left\{ \phi P_0\delta_{ij} + \frac{1}{V} \sum_n \left[\alpha^2 (F_i^n R_j^n)_{HH} + (1-\alpha)^2 (F_i^n R_j^n)_{SS} + 2\alpha(1-\alpha) (F_i^n R_j^n)_{HS} \right] \right\} \quad (5.21)$$

The product of the contact force and its position vector for each of the interactions to the lowest order in respective strain is given by

$$(F_i R_j)_{SS} = \frac{\pi R_0^3}{2} \int_{-\infty}^t G_{SS} (t-t') \frac{d}{dt'} \left[\left(\frac{r_m \epsilon_{mn}^{(SS)} r_n}{r^2} \right)^2 \right] \frac{r_i r_j}{r^2} dt' \quad (5.22)$$

$$(F_i R_j)_{HH} = \frac{\pi R_0^3}{2} \int_{-\infty}^t G_{HH} (t-t') \frac{d}{dt'} \left[\left(\frac{r_m \epsilon_{mn}^{(HH)} r_n}{r^2} \right)^2 \right] \frac{r_i r_j}{r^2} dt' \quad (5.23)$$

$$(F_i R_j)_{HS} = \frac{4\pi R_0^3}{3} \beta \int_{-\infty}^t G_{HS} (t-t') \frac{d}{dt'} \left[\left(\frac{r_m \epsilon_{mn}^{(HS)} r_n}{r^2} \right)^2 \right] \frac{r_i r_j}{r^2} dt' \quad (5.24)$$

where the soft-soft (5.22) and hard-hard (5.23) particle contact relations are taken from Routh and Russel⁴ and, G_{SS} , G_{HH} and G_{HS} are the relaxation moduli for the three con-

tacts. Note that G_{HS} becomes equal to G_{SS} when $G_{HH} \gg G_{SS}$. Assuming all orientations of the particles to be equally likely, we average over them to obtain,

$$\sigma_{ij} = -P_0\delta_{ij} - \frac{M\phi}{280} \int_{-\infty}^t \left\{ \begin{array}{l} (1-\alpha)^2(1+a)^2 G_{SS}(t-t') \\ +\alpha^2(1+b)^2 G_{HH}(t-t') \\ +\left(\frac{8}{3}\beta\right) 2\alpha(1-\alpha)(1+c)^2 G_{HS}(t-t') \end{array} \right\} \times \frac{d}{dt'} [\delta_{ij}(\epsilon_{mm}^2 + 2\epsilon_{mn}\epsilon_{nm}) + 4\epsilon_{mm}\epsilon_{ij} + 8\epsilon_{im}\epsilon_{mj}] dt' \quad (5.25)$$

where, ϕ is the total solid volume fraction and M is the average number of nearest neighbors. Up to this point, we have assumed the most general form of constitutive relation for the film deformation. In order to determine the values of a , b and c , we shall now consider special case of a packing containing hard and soft *elastic* spheres where the above relation becomes,

$$\sigma_{ij} = -P_0\delta_{ij} - \frac{M\phi}{280} G_{\text{eff}} [\delta_{ij}(\epsilon_{mm}^2 + 2\epsilon_{mn}\epsilon_{nm}) + 4\epsilon_{mm}\epsilon_{ij} + 8\epsilon_{im}\epsilon_{mj}] \quad (5.26)$$

$$\text{with } G_{\text{eff}} \equiv \left\{ \begin{array}{l} (1-\alpha)^2(1+a)^2 G_{SS} \\ +\alpha^2(1+b)^2 G_{HH} \\ +\left(\frac{8}{3}\beta\right) 2\alpha(1-\alpha)(1+c)^2 G_{HS} \end{array} \right\}$$

Landau and Lifshitz¹³ show that for an isotropic elastic material, the elastic energy density up to third order in strain is given by,

$$\mathcal{E} = \mu\epsilon_{lk}\epsilon_{kl} + \left(\frac{\kappa}{2} - \frac{\mu}{3}\right)\epsilon_{kk}\epsilon_{ll} + \frac{A}{3}\epsilon_{lk}\epsilon_{km}\epsilon_{ml} + B\epsilon_{ll}\epsilon_{km}\epsilon_{mk} + \frac{C}{3}\epsilon_{ll}\epsilon_{kk}\epsilon_{mm} \quad (5.27)$$

where μ , κ , A , B and C are material constants. On differentiating (5.27), with respect to ϵ_{ij} and comparing with (5.26) for elastic spheres, we find that in absence of solvent ($P_0 = 0$),

$$\mu = 0 ; \kappa = 0 ; \frac{A}{8} = \frac{B}{2} = C = \frac{M\phi}{280} G_{\text{eff}}$$

The elastic energy for closed packing of a latex blend (in the absence of solvent) to the lowest order in strain can be obtained by substituting values of A , B and C in (5.27). Next, we hypothesize that the non-affine strains at the particle level will be such that they minimize the elastic energy of the network. Here we use the standard principle

of minimum total potential energy, which states that of all displacements that satisfy the boundary conditions of a structural system, those corresponding to configurations of stable equilibrium make the total potential energy a relative minimum. This approach is similar to the Hashin-Shtrikman's variational method¹⁴ used to determine bounds for the overall shear modulus for composites containing linear elastic phases.

Under a given deformation, minimization of \mathcal{E} with respect to non-affine strains amounts to minimizing the coefficient G_{eff} with the constraint given in (5.18), i.e.

$$\text{Minimize } G_{\text{eff}} \text{ for Constraint : } a(1 - \alpha)^2 + b\alpha^2 + 2c\alpha(1 - \alpha) = 0 \quad (5.28)$$

Using the method of Langrange multipliers we get,

$$1 + a = \frac{1/G_{SS}}{\left[\frac{\alpha^2}{G_{HH}} + \frac{(1 - \alpha)^2}{G_{SS}} + \left(\frac{3}{8\beta} \right) \frac{2\alpha(1 - \alpha)}{G_{HS}} \right]}$$

$$1 + b = \frac{1/G_{HH}}{\left[\frac{\alpha^2}{G_{HH}} + \frac{(1 - \alpha)^2}{G_{SS}} + \left(\frac{3}{8\beta} \right) \frac{2\alpha(1 - \alpha)}{G_{HS}} \right]}$$

$$1 + c = \frac{(3/8\beta)(1/G_{HS})}{\left[\frac{\alpha^2}{G_{HH}} + \frac{(1 - \alpha)^2}{G_{SS}} + \left(\frac{3}{8\beta} \right) \frac{2\alpha(1 - \alpha)}{G_{HS}} \right]}$$

so that the effective shear modulus becomes,

$$G_{\text{eff}} = \frac{1}{\left[\frac{\alpha^2}{G_{HH}} + \frac{(1 - \alpha)^2}{G_{SS}} + \left(\frac{3}{8\beta} \right) \frac{2\alpha(1 - \alpha)}{G_{HS}} \right]}$$

Note that the constitutive relation (5.26) is similar to that derived by Routh and Russel⁴ for identical spheres except that the shear modulus is replaced by the effective modulus.

Tirumkudulu and Russel³ used their constitutive relation to calculate the stress field in a drying film and determined the critical stress for the film to crack by adopting the well known Griffith's energy balance concept. For the case of a drying film containing

latex blends, we can write directly the expression for the critical stress for cracking,

$$\frac{\sigma_{c,i}R_0}{2\gamma} = 0.1877 \left(\frac{2R_0}{h} \right)^{\frac{2}{3}} \left(\frac{G_{\text{eff}}M\phi_{\text{rcp}}R_0}{2\gamma} \right)^{\frac{1}{3}}. \quad (5.29)$$

Here, γ is the liquid-gas interfacial tension, h is the film thickness and ϕ_{rcp} is the random close packing volume fraction. The derivation of the above expression can be understood from a simple scaling analysis. According to the constitutive relation, the in-plane tensile stress generated in the film during drying scales with the square of the strain, $\sigma \sim G\epsilon^2$. On equating the elastic energy recovered per unit length of crack, $E_e \sim h^2\sigma\epsilon$, to the increased surface energy per unit length, $E_s \sim \gamma h$, gives the critical stress for cracking, $\sigma_c \sim G^{1/3}(\gamma/h)^{2/3}$. Note that the critical stress is independent of particle size.

More recently, Singh and Tirumkudulu⁵ identified two regimes for obtaining crack free films for a drying colloidal film containing identical particles. The *strain-limited* regime pertains to the case of a drying film containing soft particles where the particles completely deform to fill the pores under the capillary pressure exerted by the menisci at the top of the film. This is possible only when the tensile stress at maximum deformation is less than the critical stress. Thus the critical cracking thickness h_{max} below which the films are crack-free is obtained from, $G^{1/3}(\gamma/h)^{2/3} \sim G(1 - \phi_{\text{rcp}})^2$ giving $h_{\text{max}} \sim \gamma/G(1 - \phi_{\text{rcp}})^2$. Alternatively, the *stress-limited* regime occurs when the particles are hard and the menisci adjust their curvature till the maximum capillary pressure (P_{max}) is reached, beyond which they recede into the network resulting in partial deformation. Here the critical thickness is obtained by equating the stress at P_{max} to the critical cracking stress, $\sigma_c \sim G^{1/3}(\gamma/h)^{2/3} \sim -P_{\text{max}}$, giving, $h_{\text{max}} \sim \gamma G^{1/2}/(-P_{\text{max}})^{3/2}$. For latex blends, the corresponding critical cracking thickness for the *strain-limited* regime is given by,

$$h_{\text{max}} = \frac{37\gamma}{G_{\text{eff}}M\phi_{\text{rcp}}(1 - \phi_{\text{rcp}})^3} \quad (5.30)$$

while that for the *stress-limited* regime is,

$$h_{\text{max}} = 0.64 \left[\frac{G_{\text{eff}}M\phi_{\text{rcp}}R_0^3}{2\gamma} \right]^{1/2} \left[\frac{2\gamma}{-P_{\text{max}}R_0} \right]^{3/2} \quad (5.31)$$

A single value of the dimensionless capillary pressure, $-P_{\max}R_0/2\gamma \sim 1.4$, resulted in a good match between CCT measurements and above predictions over a wide range of particle sizes and rigidities. The same value was used in this study for all values of α .

5.3 EXPERIMENTS

Experiments were conducted with a blend of silica and acrylic (BX261) particles of same size. Details of the dispersions used in this study are given in table 5.1. Although the particle size is same, there is a significant difference in particle rigidity. The composition of the blend is described in terms of relative hard particle volume fraction ratio, α . The value of α was varied from 0 to 1 and for each composition, the critical stress for cracking as a function of film thickness and critical cracking thickness (CCT) were measured.

The CCT measurements were performed over a temperature range of 25-28°C and a relative humidity of 35-40%. Thin films were cast on glass substrates placed on a spin coater (slow rotation rate~20 rpm) by disbursing small amounts of dispersion. Here, the spin coater was employed to spread the liquid uniformly over a fixed area so as to obtain a nearly circular film. Further, the thickness of the film was varied by disbursing increasing amounts of dispersion over the same area. After the films were cast, they were left to dry under ambient conditions. On complete drying, it was examined under an optical upright microscope (Olympus[®], BX-60) for cracks at varying magnifications. Finally, the thickness profile of the dry film was obtained using a surface profilometer (Dektak-150[®]). It should be noted that in some cases the entire film was crack free which gave the lower limit for CCT.

The classical cantilever technique was employed to measure the stress in a drying film.¹⁵ Here, a thin layer of the dispersion was applied on a thin silicon wafer of dimensions 13 mm (length) by 5 mm (width) by 0.128 mm (thickness) and clamped on one side. A laser beam is reflected from the free end of the substrate and collected by a

position sensitive detector (On-track[®]). The position of the detector is set in such a way that the reflected beam falls normally on the surface of the detector. The entire detector assembly is mounted on a traverse so that the desired positioning can be done with precision. The position data (i.e. the x, y coordinates of the reflected beam) from the detector is directly fed to a computer. As the film dries, the tensile stresses in the drying film bend the substrate that consequently results in the movement of reflected beam on detector surface. Finally, the displacement of the reflected beam is related to the average tensile stress in the film. The details of stress measurement technique and CCT measurements can be found in Tirumkudulu and Russel¹² and Singh and Tirumkudulu⁵ respectively.

We also ensured that the evaporation rate for these experiments was constant throughout the experiment. This was checked by drying films separately under similar conditions on a weigh balance. We also noticed that the drying rate remained constant long after the film cracked. Hence, we could also measure the evaporation rate of the sample used for stress experiments by transferring it to the weigh balance immediately after it cracked and recording its weight change.

In blends, one of the major concerns is the distribution of the constituent soft and hard particles. As reported by Feng et al.,⁹ the morphology of blend films is influenced by the distribution of hard and soft particles. Films were examined using scanning electron microscopy to see the particle distribution.

5.4 RESULTS AND DISCUSSION

As shown in table 5.1, the blends contain particles of similar size but with a very different shear moduli. In order to see the particle distribution in the final film, dried films were viewed under a scanning electron microscope. Figure 5.2 shows the SEM image of the surface of a dried film with $\alpha = 0.5$. The hard particles are uniformly

distributed in the matrix of soft particles. Further, the soft acrylic particles seemed to have undergone significant deformation at the film surface. In order to see the particle distribution throughout the film, the film was cut and the cross section imaged. Again, the cross section or the interior of the film has a uniform distribution of both the soft and hard particles (figure 5.3). Here also, the soft particles can be seen to have deformed significantly. To differentiate between the two types of particles and to ascertain their distribution inside the film, we exposed one of the films to an ambient temperature of about 70°C in an oven for half an hour. Since the glass transition temperature of the soft (acrylic) particles is 40°C, we expect the particles to fuse completely on heating at such an elevated temperature. Figure 5.4 shows the SEM image of one such film where the deformed domains confirm that the distribution of soft-hard particles in the blend is indeed uniform. Figure 5.5 shows the SEM image of the same film close to the film-substrate interface. It appears that the film has a slightly larger number of hard particles at the film-substrate interface compared to the soft particles but this segregation appears to be restricted close to the substrate. We next look at the particle distribution for $\alpha = 0.95$ (figure 5.6). As can be seen, the hard particles in the film are packed in well-ordered domains. Further, the coalesced soft particles can also be seen at a few locations between the hard particles. This is indeed surprising given that the soft particle fraction is very small which suggests that the hard and soft particles are dispersed well at all volume fractions.

Figure 5.7 presents the dimensionless stress evolution as a function of the dimensionless time for four different values of α . Once the particle concentration reaches that for random packing, the stress starts to increase, reaches a maximum at which the film cracks, and then decreases. Note that we do not present the full stress relaxation profile after cracking as the samples are removed for measuring the evaporation rate shortly after the crack initiation. For both $\alpha = 0$ and 0.5, the increase and the decrease in stress is slow suggesting that the film undergoes viscous deformation. This suggests that even with 50% hard particles, the response is essentially that for soft particles. This obser-

vation is in line with the experiments of Martinez and Lewis⁶ who did not find any significant variation with hard particle fraction in stress profile for films containing less than 40% hard particles. In contrast to these profiles, those for $\alpha = 0.9$ and 1 show that the stress reaches a maximum value within $\Delta\bar{t} = 0.01$ and decreases to a negligible value as quickly. The response here is entirely elastic as the stress relaxes to a negligible value immediately after crack nucleation.

5.4.1 Comparison with the model

The dependence of effective shear modulus on α , as predicted by the model, is presented in figure 5.8. The effective shear modulus varies little and is close to the shear modulus of the soft particles for $\alpha < 0.95$. This suggests that the addition of hard particles into the soft matrix for $\alpha < 0.95$ does not significantly contribute to the mechanical properties of the film and hence the blend essentially behaves like the one composed of only soft particles. However, at a value of α close to 0.95, a steep increase in the effective shear modulus is seen. It implies that the transition from soft to rigid-like behavior takes place at this value of α . The experimental results shown in figure 5.6 also point to this type of behavior where the hard particles are packed in a very ordered structure and hence are capable of transmitting the applied load to the entire film. It is interesting to note that the model predictions are in good agreement with the numerical simulations of Jagota and Scherer¹¹ who showed that the rigidity threshold in a mixture of soft-hard particles with sliding contacts between hard particles is at a site fraction close to 0.95. However, it is important to note that for cases where the shear moduli for soft-soft (G_{SS}) and hard-hard (G_{HH}) interactions are comparable, a more gradual transition from soft to rigid-like behavior will be observed unlike the one seen in figure 5.8.

The variations in dimensionless critical stress with the dimensionless film thickness over the entire range of volume fraction ratio (α) are shown in figure 5.9. The dependence

of dimensionless critical stress on dimensionless film thickness for $0 < \alpha < 1$ is similar to the predicted behavior of G_{eff} in that a jump in the critical stress is seen for values of $\alpha \geq 0.95$. The stress measurements also confirm the transition from soft to rigid-like behavior at $\alpha \sim 0.95$. Figure 5.10 compares the stress measurements with those predicted by the model. Here, the theoretical plots are scaled in such a way that the line for $\alpha = 1$ matches with the experiments. The predicted critical stress variation with film thickness matches with all the experiments in that the exponent of two-thirds is close to the observed trend. This confirms the validity of the proposed approach to lump the modulus variations in G_{eff} . However, at lower values of α , the absolute values are lower than the experimental results. The discrepancy can be attributed to the viscous deformation of the soft particles. The energy dissipation reduces the stored elastic energy in the network thereby requiring higher stresses to crack the film.

The experimental results for critical cracking thickness (CCT) are compared with the theoretical predictions for different values of α in figure 5.11. The measured CCT varies almost linearly with α whereas the model shows an abrupt increase in CCT at a value of α close to 0.95. This is somewhat surprising given that the trend for the measured critical stress shows a negligible variation for $\alpha < 0.95$. The model predictions match well with theory for both low and high values of α but exhibit large differences for the intermediate values. One possible reason for the discrepancy could be the following. The critical cracking stress for a thin film varies inversely with film thickness (5.29). For the measurement of critical stress, we typically apply thick films ($\sim 100 - 200 \mu\text{m}$) on our substrates and measure the stress at which the film cracks. Since the stresses are low, we would expect small particle deformations in the film and, for higher values of α , they would be mostly elastic. On the other hand, we apply thin films ($\sim 5 - 20 \mu\text{m}$) to determine the critical cracking thickness. Here, the film experiences the highest possible stress that corresponds to the maximum capillary pressure. Consequently, at such large stresses we can expect significant viscous deformation of the particles. It is possible that the simple assumptions made to account for the non-affine deformation (5.16) may

not be valid at such large deformations. Thus the large mismatch may be due to the significant viscous deformation of the soft particles although the model assumes them to undergo small elastic deformation in the packing. More work is required to resolve these issues.

5.5 CONCLUSION

A mathematical model for film formation in latex blends has been developed. The model captures the main aspects of drying and cracking behavior of the blend films. The model predictions correspond well with the numerical simulations reported in the literature for the transition in soft to rigid-like behavior for blends of hard and soft particles. Further, the model predictions are validated with extensive experimental data. While the predicted critical stresses match well with the measured values, the critical thickness shows a trend different from the experiments. The viscous deformation of the particles in the drying film which has not been accounted for in the model may be the cause for the discrepancy.

5.6 ACKNOWLEDGEMENT

This work was supported by the Department of Science and Technology, India. The authors thank Dr Martin Murray of AkzoNobel for discussions and Dr S L Kamath of Metallurgy and Materials Science Department of IIT-Bombay for help with SEM images. The preliminary theoretical calculations appear in the Masters thesis of Girish Deoghare.¹⁶

REFERENCES

- [1] M. A. Winnik and J. Feng. Latex blends: An approach to zero voc coatings. *J. Coat Technol.*, 68(852):39–50, 1996.
- [2] S. Lepizzera, C. Lhommeau, G. Dilger, T. Pith, and M. Lambla. Film-forming ability and mechanical properties of coalesced latex blends. *J. Poly Sci(B)*, 35: 2093–2101, 1997.
- [3] M. S. Tirumkudulu and W. B. Russel. Cracking in drying latex films. *Langmuir*, 21(11):4938–4948, 2005.
- [4] A. F. Routh and W. B. Russel. A process model for latex film formation: Limiting regimes for individual driving forces. *Langmuir*, 15(22):7762–7773, 1999.
- [5] K. B. Singh and M. S. Tirumkudulu. Cracking in drying colloidal films. *Phys Rev Lett*, 98:218302(1)–218302(4), 2007.
- [6] C. J. Martinez and J. A. Lewis. Shape evolution and stress development during latex-silica film formation. *Langmuir*, 18:4689–4698, 2002.
- [7] D. Colombini, H. Hassander, O.J. Karlsson, and F. H. J. Maurer. Influence of the particle size and particle size ratio on the morphology and viscoelastic properties of bimodal hard/soft latex blends. *Macromolecules*, 37:6865–6873, 2004.
- [8] A. Tzitzinou and J. L. Keddie. Film formation of latex blends with bimodal particle size distribution: Consideration of particle deformability and continuity of the dispersed phase. *Macromolecules*, 33:2695–2708, 1999.
- [9] J. Feng, M. A. Winnik, R. Richard, and B. Clubb. Polymer blend latex films: Morphology and transparency. *Macromolecules*, 28:7671–7682, 1995.

- [10] A. Jagota and G. W. Scherer. Viscosities and sintering rates of a two-dimensional granular composite. *J. Am. Ceram. Soc.*, 76(12):3123–3135, 1993.
- [11] A. Jagota and G. W. Scherer. Viscosities and sintering rates of composite packings of spheres. *J. Am. Ceram. Soc.*, 78(3):521–528, 1995.
- [12] M. S. Tirumkudulu and W. B. Russel. Role of capillary stresses in film formation. *Langmuir*, 20:2947–2961, 2004.
- [13] L. D. Landau and E. M. Lifshitz. *Theory of Elasticity*. Pergamon ,New York, first edition, 1986.
- [14] Z. Hashin and S. Shtrikman. A variational approach to the theory of the elastic behavior of multiphase materials. *J. Mech. Phys. Solids*, 11:127–140, 1963.
- [15] C Petersen, C Heldmann, and D Johannsmann. Internal stresses during film formation of polymer lattices. *Langmuir*, 15:7745–7751, 1999.
- [16] G Deoghare. Mathematical modeling of stress development in a composite film of deformable spheres with rigid inclusions. Master’s thesis, Indian Institute of Technology-Bombay, 2006.

APPENDIX A: CALCULATION OF R_t/R_0 RATIO

Consider the following position of hard and soft spheres. With the origin of the coordinate system fixed at the center of the soft sphere, R_t the radius of the soft sphere, R_0 the radius of the rigid sphere at any stage of deformation and d_t defined as distance between centers of both spheres, the equation for the soft sphere becomes,

$$x^2 + y^2 + z^2 = R_t^2 \quad (5.32)$$

and that for the hard sphere is ,

$$x^2 + y^2 + (z - d_t)^2 = R_0^2 \quad (5.33)$$

The plane of intersection between two spheres is given by solving (5.32) and (5.33) and is at distance $z = z'$ from the origin,

$$z' = \frac{R_t^2 - R_0^2 + d_t^2}{2d_t} \quad (5.34)$$

The sectional volumes are shown in figure 5.12. The volume of the section of the sphere is given by,

$$V_i = \frac{\pi}{6} h_i (3r_i^2 + h_i^2) \quad i = 1, 2$$

where V_1 is the volume enclosed in section ACBA and V_2 is the volume of the section ADBA. The height h_1 and radius r_1 for the sectional volume V_1 are, $h_1 = (R_0 - d_t + z')$ and $r_1 = (R_0^2 - (d_t - z')^2)^{\frac{1}{2}}$. Similarly, for the sectional volume of soft sphere, we have $h_2 = (R_t - z')$ and $r_2 = (R_t^2 - z'^2)^{\frac{1}{2}}$. The hard and soft spheres are assumed to be initially of equal radii. Enforcing the volume conservation condition, we have

$$\frac{4}{3}\pi R_t^3 - V_1 - V_2 = \frac{4}{3}\pi R_0^3 \quad (5.35)$$

APPENDIX B: TWO PARTICLE CO-ORDINATE SYSTEM

Equation of the soft sphere at any time is given by,

$$x^2 + y^2 = R_t^2 - z^2 = f_1(z) \quad (5.36)$$

The equation of the surface is given by,

$$F_1 = x^2 + y^2 - f_1(z)$$

so that the normal unit vector to the surface of the soft particle is given by

$$\hat{n}_1 = \frac{\vec{\nabla} F_1}{|\vec{\nabla} F_1|} = \frac{2x \hat{e}_x + 2y \hat{e}_y - f_1'(z) \hat{e}_z}{\sqrt{4(x^2 + y^2) + f_1'(z)^2}} = \frac{r}{R_t} \hat{e}_r - \frac{f_1'(z)}{2R_t} \hat{e}_z, \quad (5.37)$$

where $f_1'(z) = -2z$. Similarly, the normal to the surface of the harder particle is given by

$$\hat{n}_2 = \frac{2x \hat{e}_x + 2y \hat{e}_y - f_2'(z) \hat{e}_z}{\sqrt{4(x^2 + y^2) + f_2'(z)^2}} = \frac{r}{R_0} \hat{e}_r - \frac{f_2'(z)}{2R_0} \hat{e}_z \quad (5.38)$$

where the equation of the second sphere is given by,

$$x^2 + y^2 = R_0^2 - (z - d_t)^2 = f_2(z) \quad (5.39)$$

The area of the surface element for the first sphere is given by (Figure 5.13),

$$dA = \frac{\sqrt{f_1'(z)}}{\cos\psi} dzd\theta = R_t dzd\theta$$

so that the surface integral of a function $M(z, \theta)$ over the surface of the soft sphere is given by (5.40),

$$(S.I.)_1 = \int_0^{2\pi} \int_{z_1}^{z_2} M(z, \theta) R_t dzd\theta \quad (5.40)$$

Integrating the above surface integral for the soft sphere within limits, $z_1 = -R_t$ and $z_2 = z'$, the value of surface deformation is given by

$$(S.I.)_1 = \int_0^{2\pi} \int_{-R_t}^{z'} \frac{1}{2} [2(R_t - R_0) \hat{n}_1 \hat{n}_1 + g(R_0, \epsilon_{HS}) (\hat{n}_1 \hat{e}_z + \hat{e}_z \hat{n}_1)] dzd\theta \quad (5.41)$$

For the hard sphere, the limit of definite integral becomes $z_1 = z'$ and $z = R_0 + d_t$, the value of the surface integral then becomes,

$$(S.I.)_2 = \int_0^{2\pi} \int_{z'}^{R_0+d_t} -(2R_0 - d_t) R_0 (\hat{n}_2 \hat{e}_z + \hat{e}_z \hat{n}_2) dz d\theta \quad (5.42)$$

Calculation of the trace

For an incompressible material, the trace of $\{\int_V \vec{\epsilon} dV\}=0$. The strain integrated over the volume of the two spheres, can be written in terms of the surface integral over surface displacements,

$$\int_V \vec{\epsilon}_{HS} dV = \int_V \frac{1}{2} (\vec{\nabla} \vec{S} + \vec{\nabla} \vec{S}^T) dV = \int_A \frac{1}{2} (\hat{n} \vec{S} + \vec{S} \hat{n}) dA \quad (5.43)$$

For the soft sphere, the displacement vector is along the outward direction radial from its center,

$$\vec{S}_1 = (R_t - R_0) \hat{n}_1 + g(R_0, \epsilon_{HS}) \hat{e}_z$$

The normal \hat{n}_1 to the surface of soft sphere is given by (5.37), so that

$$\hat{n}_1 \hat{n}_1 = \frac{r^2}{R_t^2} \hat{e}_r \hat{e}_r + \frac{f_1'(z)^2}{4R_t^2} \hat{e}_z \hat{e}_z - \frac{r f_1'(z)}{2R_t^2} (\hat{e}_r \hat{e}_z + \hat{e}_z \hat{e}_r) \quad (5.44)$$

The zero trace condition results in two surface integrals, I_1 with terms containing $\hat{e}_x \hat{e}_x$ and $\hat{e}_y \hat{e}_y$, and, I_2 and I_3 with terms containing $\hat{e}_z \hat{e}_z$ for the soft sphere while I_4 is obtained

for the hard sphere,

$$\begin{aligned}
I_1 &= \int_0^{2\pi} \int_{-R_t}^{z'} \frac{r^2}{R_t^2} (R_t - R_0) R_t (\cos \theta \hat{e}_x + \sin \theta \hat{e}_y) (\cos \theta \hat{e}_x + \sin \theta \hat{e}_y) dz d\theta \\
&= \pi \int_{-R_t}^{z'} \left(\frac{R_t - R_0}{R_t} \right) (R_t^2 - z^2) (\hat{e}_x \hat{e}_x + \hat{e}_y \hat{e}_y) dz \\
&= \pi (R_t - R_0) \left[R_t z' - \frac{z'^3}{3R_t} + \frac{2}{3} R_t^2 \right] (\hat{e}_x \hat{e}_x + \hat{e}_y \hat{e}_y) \\
I_2 &= \int_0^{2\pi} \int_{-R_t}^{z'} \frac{f_1'^2}{4R_t^2} (R_t - R_0) R_t \hat{e}_z \hat{e}_z dz d\theta \\
&= 2\pi \int_{-R_t}^{z'} \frac{(R_t - R_0)}{R_t} z^2 \hat{e}_z \hat{e}_z dz \\
&= 2\pi (R_t - R_0) \left[\frac{z'^3}{3R_t} + \frac{R_t^2}{3} \right] \hat{e}_z \hat{e}_z \\
I_3 &= \int_0^{2\pi} \int_{-R_t}^{z'} \frac{f_1'}{2R_t} g(R_0, \epsilon_{HS}) R_t \hat{e}_z \hat{e}_z dz d\theta
\end{aligned}$$

For the hard sphere, the displacement is along the \hat{e}_z direction, so that the surface displacement vector is,

$$\vec{S}_2 = -(2R_0 - d_t) \hat{e}_z \tag{5.45}$$

Hence, $\left\{ \int_A \frac{1}{2} (\hat{n}_2 \vec{S}_2 + \vec{S}_2 \hat{n}_2) dA \right\}$ is given by :

$$\begin{aligned}
I_4 &= \int_0^{2\pi} \int_{z'}^{d_t+R_0} \frac{f_2'(z)}{2R_0} (2R_0 - d_t) R_0 \hat{e}_z \hat{e}_z dz d\theta \\
&= -2\pi \int_{z'}^{d_t+R_0} (2R_0 - d_t)(z - d_t) dz \\
&= -2\pi(2R_0 - d_t) \left[\frac{z^2}{2} - d_t z \right]_{z'}^{d_t+R_0} \\
&= -2\pi(2R_0 - d_t) \left[\frac{R_0^2 - d_t^2}{2} - \frac{z'^2}{2} + d_t z' \right] \hat{e}_z \hat{e}_z
\end{aligned}$$

The other terms in the trace $\left\{ \int_V \vec{\epsilon}_{HS} dV \right\}$ go to zero because for the co-ordinate system defined,

$$\int_0^{2\pi} \hat{e}_r d\theta = \int_0^{2\pi} (\cos \theta \hat{e}_x + \sin \theta \hat{e}_y) d\theta = 0 \quad (5.46)$$

Also , it can be verified that,

$$\int_0^{2\pi} \hat{e}_r \hat{e}_r d\theta = \int_0^{2\pi} (\cos \theta \hat{e}_x + \sin \theta \hat{e}_y)(\cos \theta \hat{e}_x + \sin \theta \hat{e}_y) d\theta = \pi(\hat{e}_x \hat{e}_x + \hat{e}_y \hat{e}_y) \quad (5.47)$$

Table 5.1: *Details of dispersions used in the present study*

Dispersion	Particle Composition	Particle Diameter (nm)	T_g ($^{\circ}\text{C}$)	Shear Modulus G (GPa)
Colloidal Silica	Silica	330		31
Acrylic (BX 261)	Acrylate	353	40	0.8

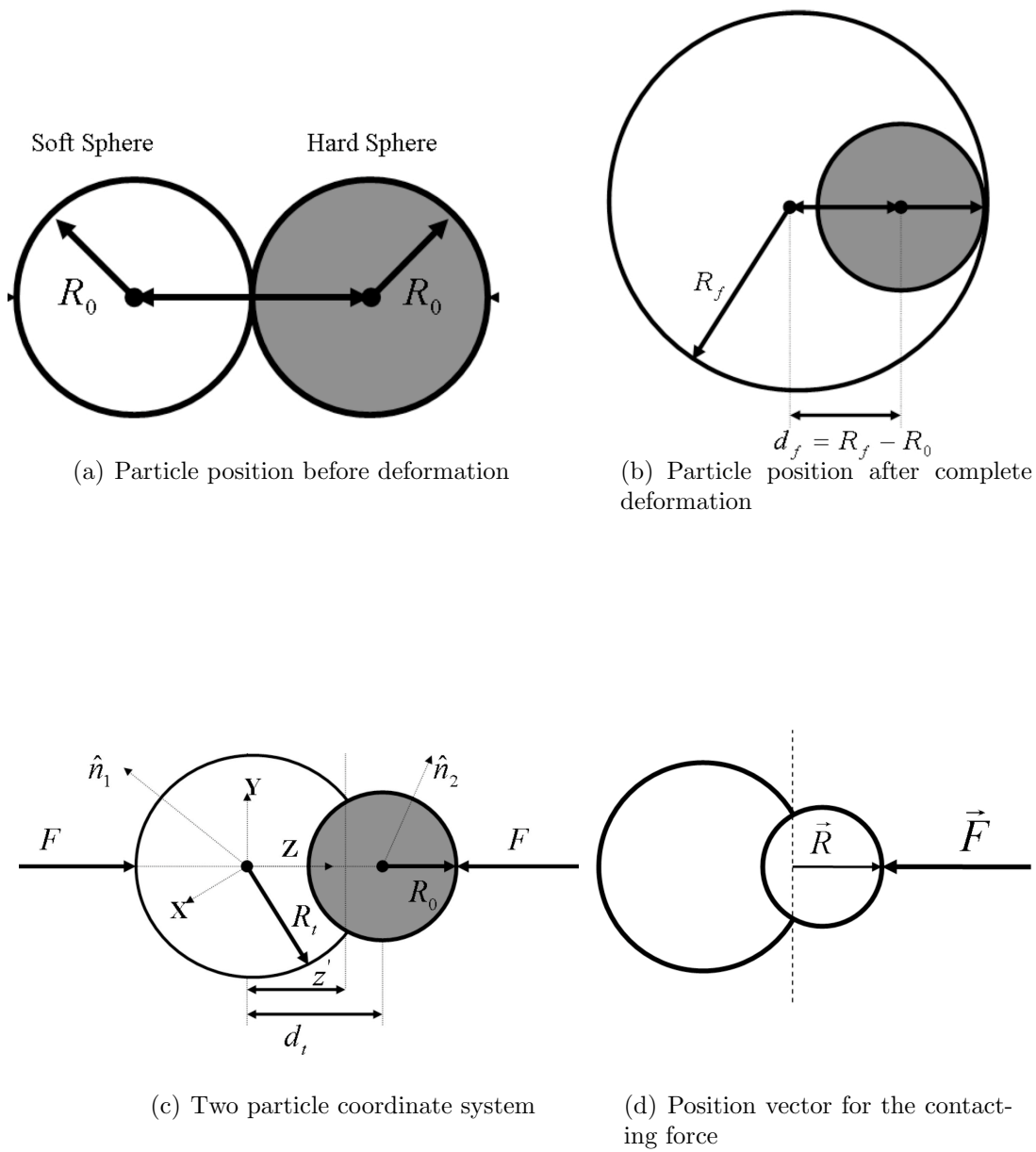


Figure 5.1: Particle positions during deformation

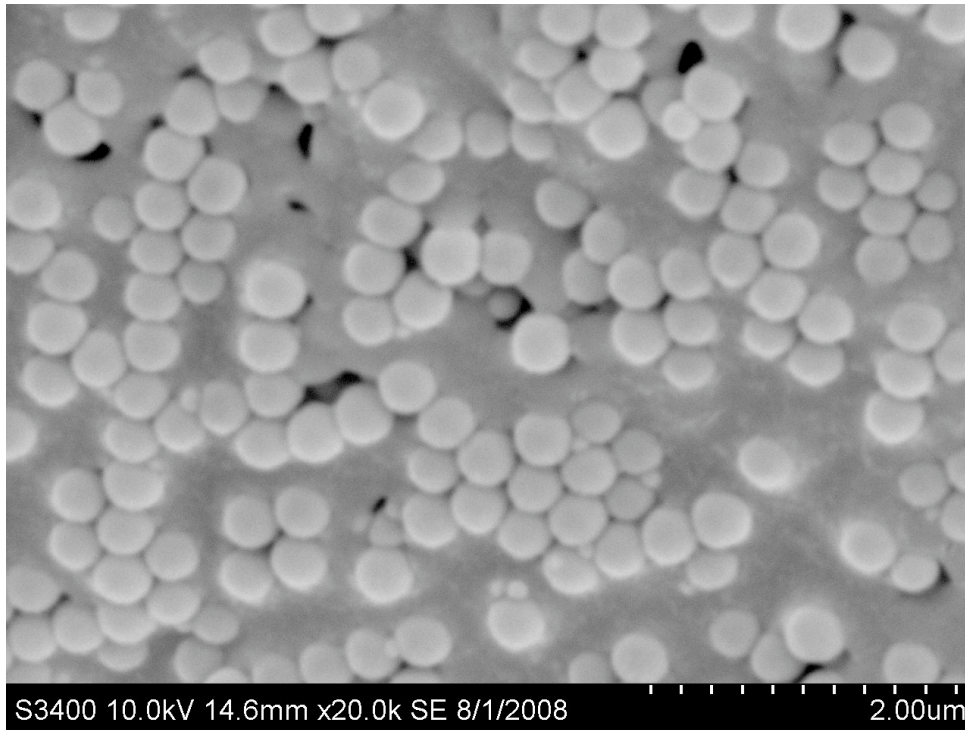


Figure 5.2: Scanning electron micrograph of the surface of a blend film with $\alpha = 0.5$.

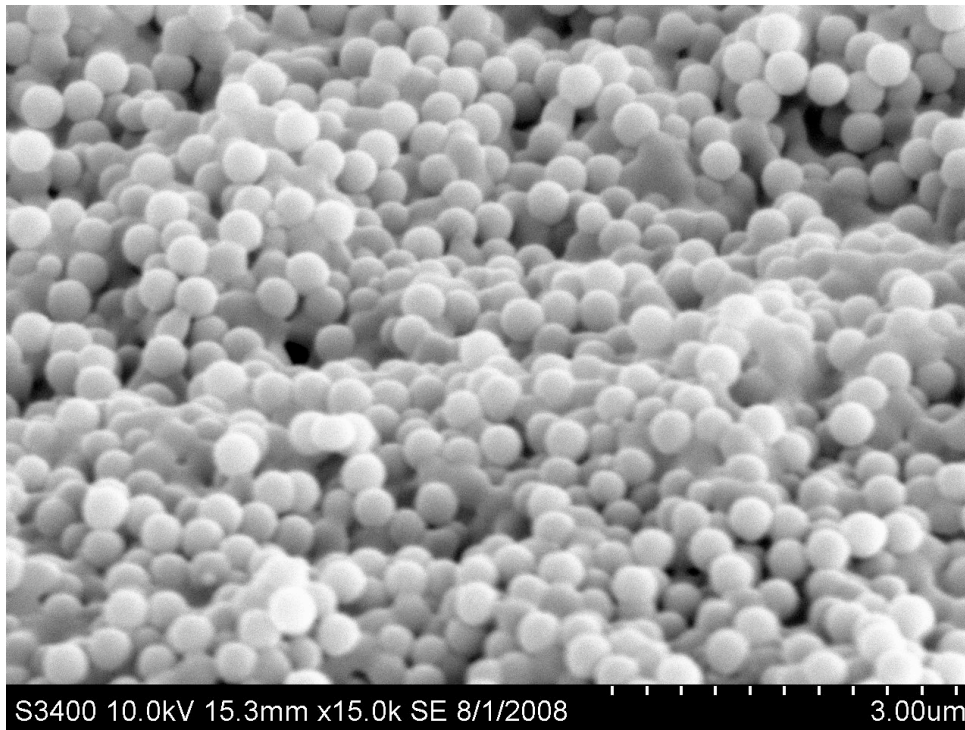


Figure 5.3: Scanning electron micrograph of the cross-section of a blend film with $\alpha = 0.5$.

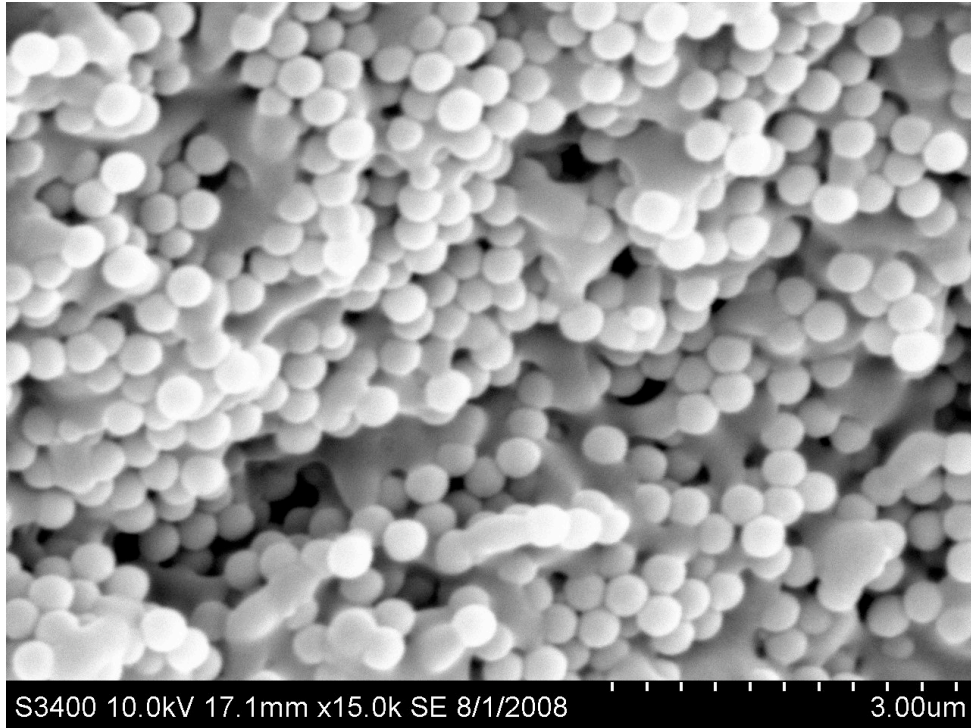


Figure 5.4: Scanning electron micrograph of the cross-section of a blend film with $\alpha = 0.5$, heated at 70°C for about half an hour.

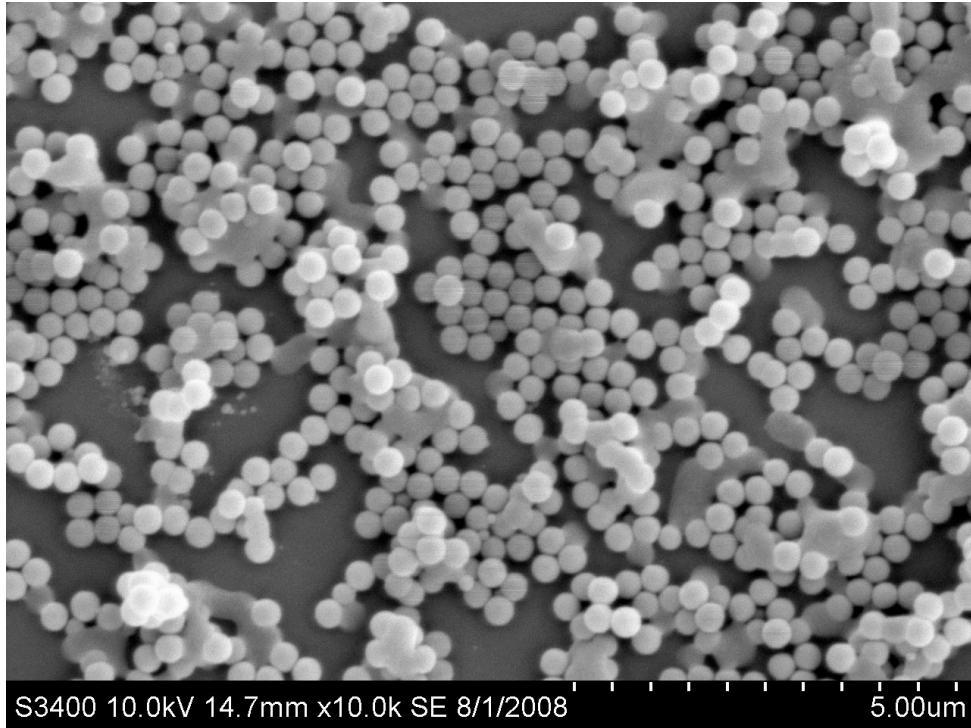


Figure 5.5: Scanning electron micrograph of the film-substrate interface of a blend film with $\alpha = 0.5$, heated at 70°C for about half an hour.

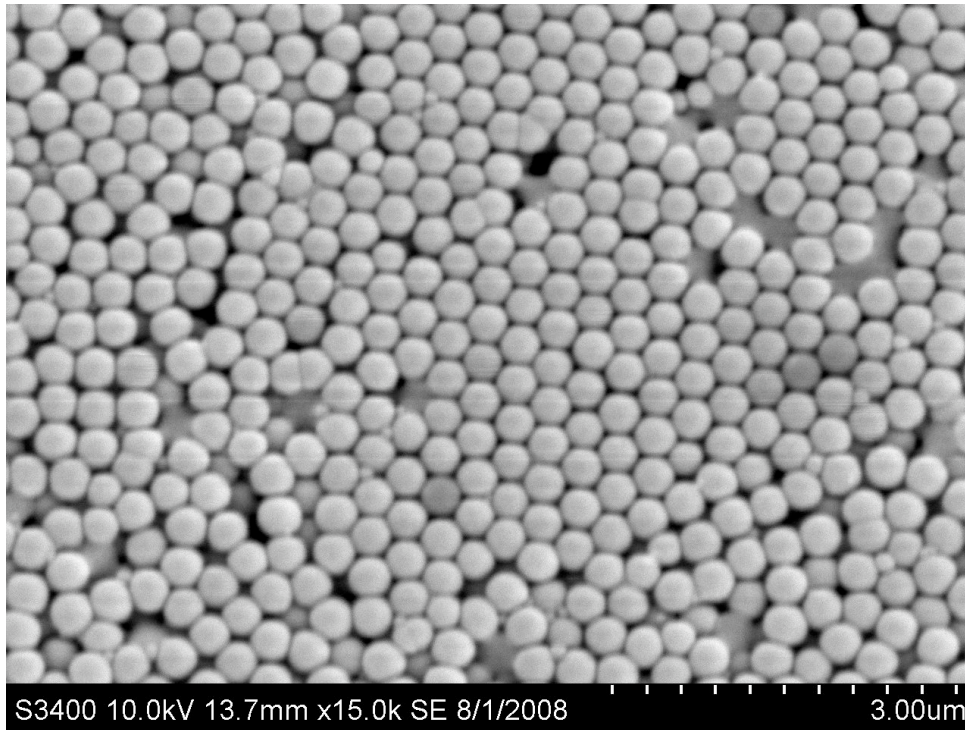
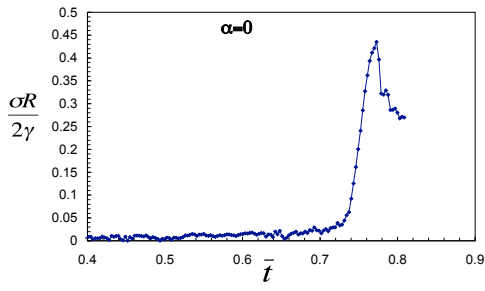
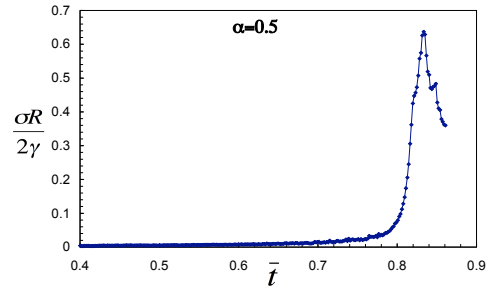


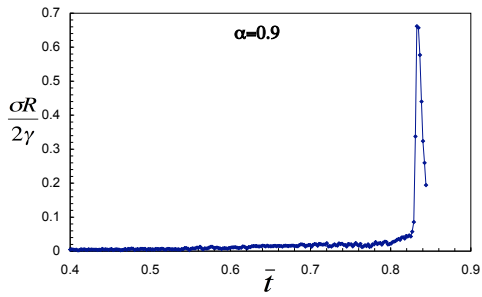
Figure 5.6: Scanning electron micrograph of the surface of a blend film with $\alpha = 0.95$.



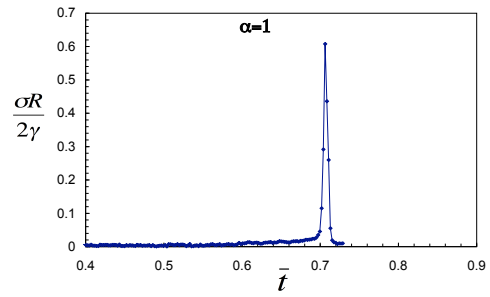
(a) $\alpha = 0$



(b) $\alpha = 0.5$



(c) $\alpha = 0.9$



(d) $\alpha = 1$

Figure 5.7: Dimensionless stress versus dimensionless time, $\bar{t} \equiv \dot{E}t/(h_o(1 - \phi_o))$, for various α , where \dot{E} is the evaporation rate, h_o is the initial average wet film thickness and ϕ_o is the initial particle volume fraction. Note that the initial thickness is different in the four cases.

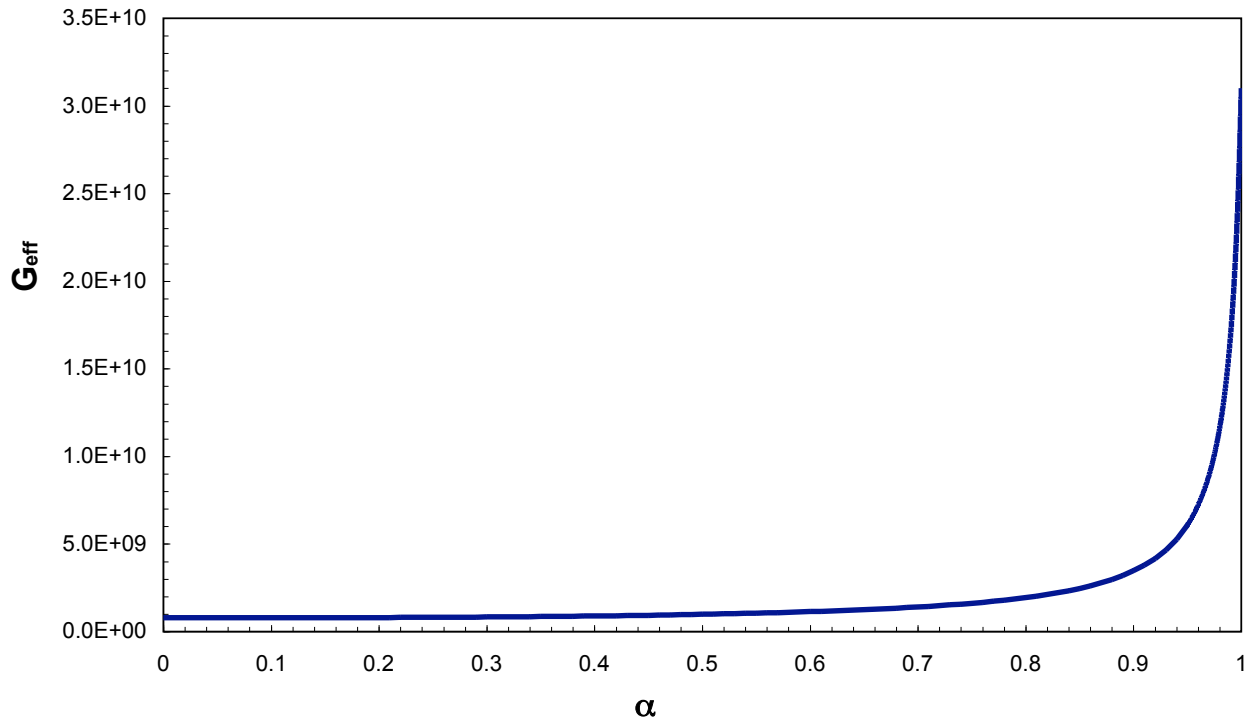


Figure 5.8: Variation of effective shear modulus (G_{eff}) with α . Note that the shear moduli for different interactions are $G_{\text{HH}} = 31$ GPa, $G_{\text{SS}} = 0.8$ GPa and $G_{\text{HS}} = 0.8$ GPa.

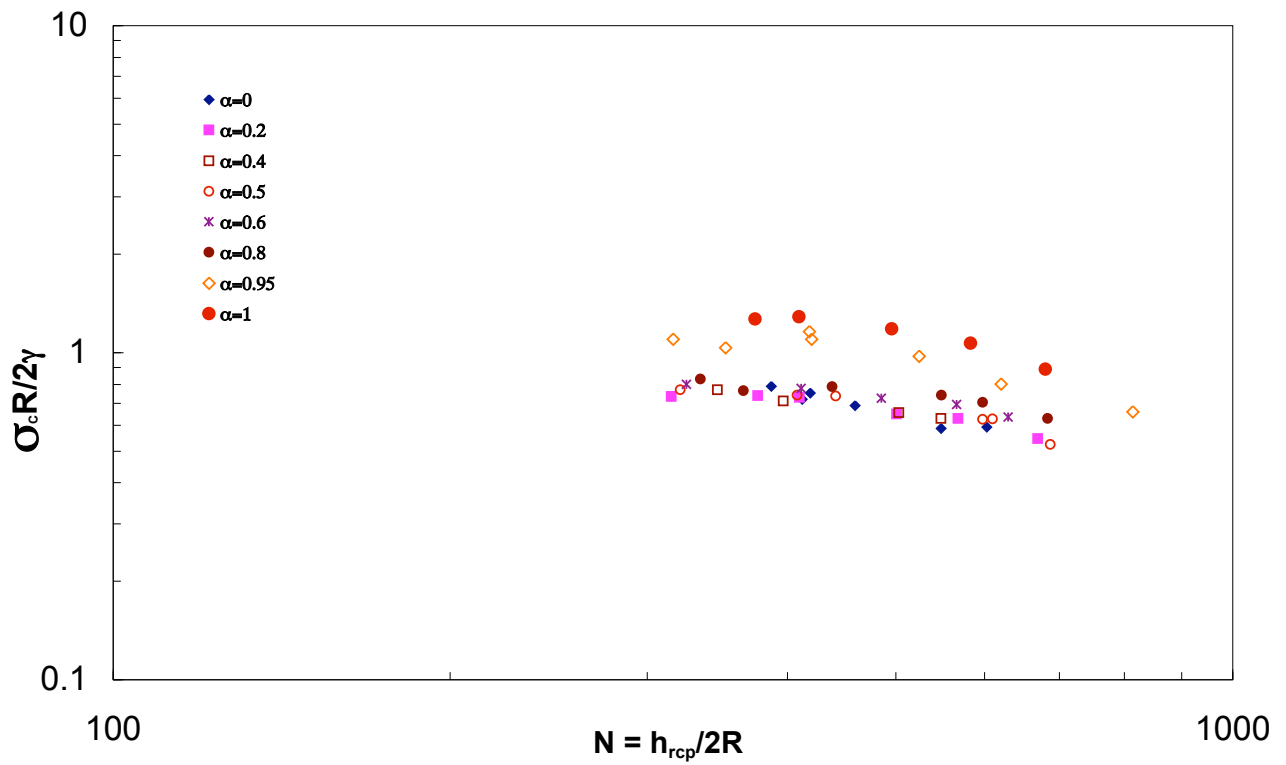


Figure 5.9: Variation of dimensionless critical stress with dimensionless film thickness for a blend of silica and acrylic (BX261) for different hard particle volume fractions.

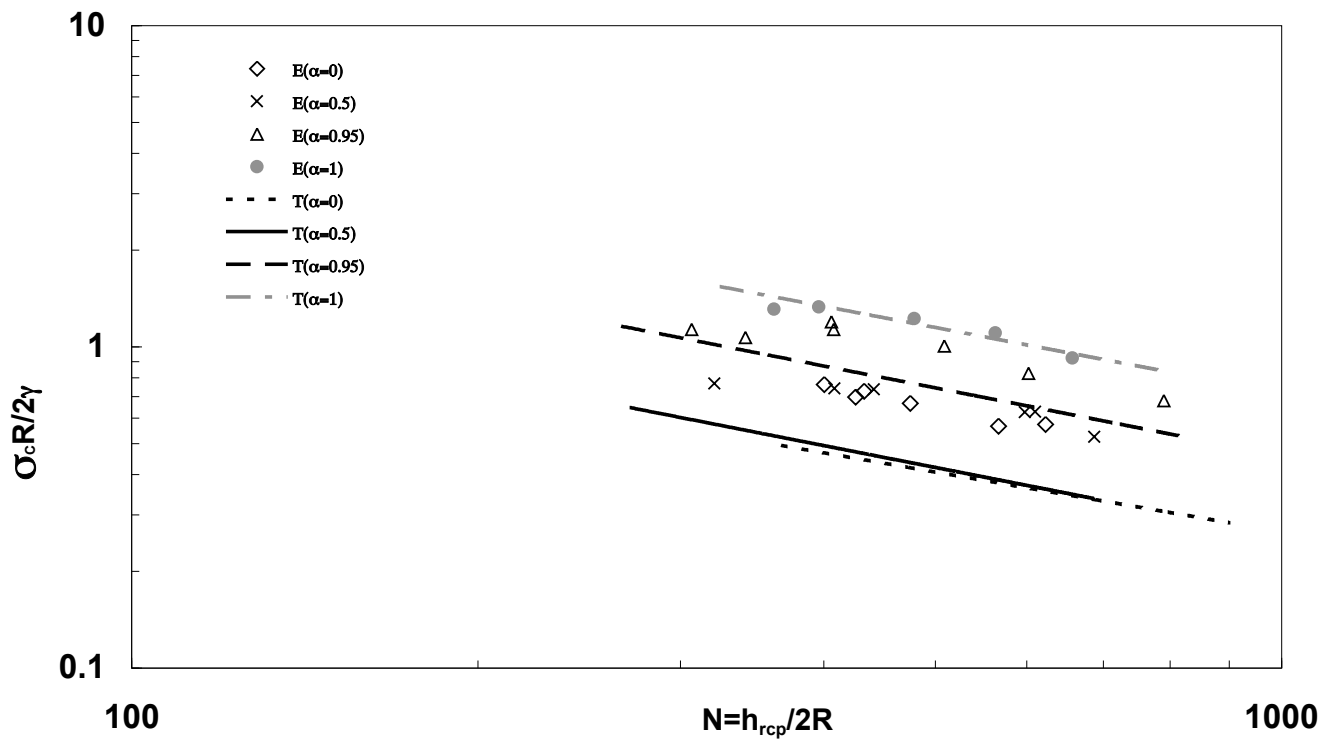


Figure 5.10: Comparison of experimental results with the theoretical predictions for various values of α . Here, E represents experimental measurements while T refers to the theory.

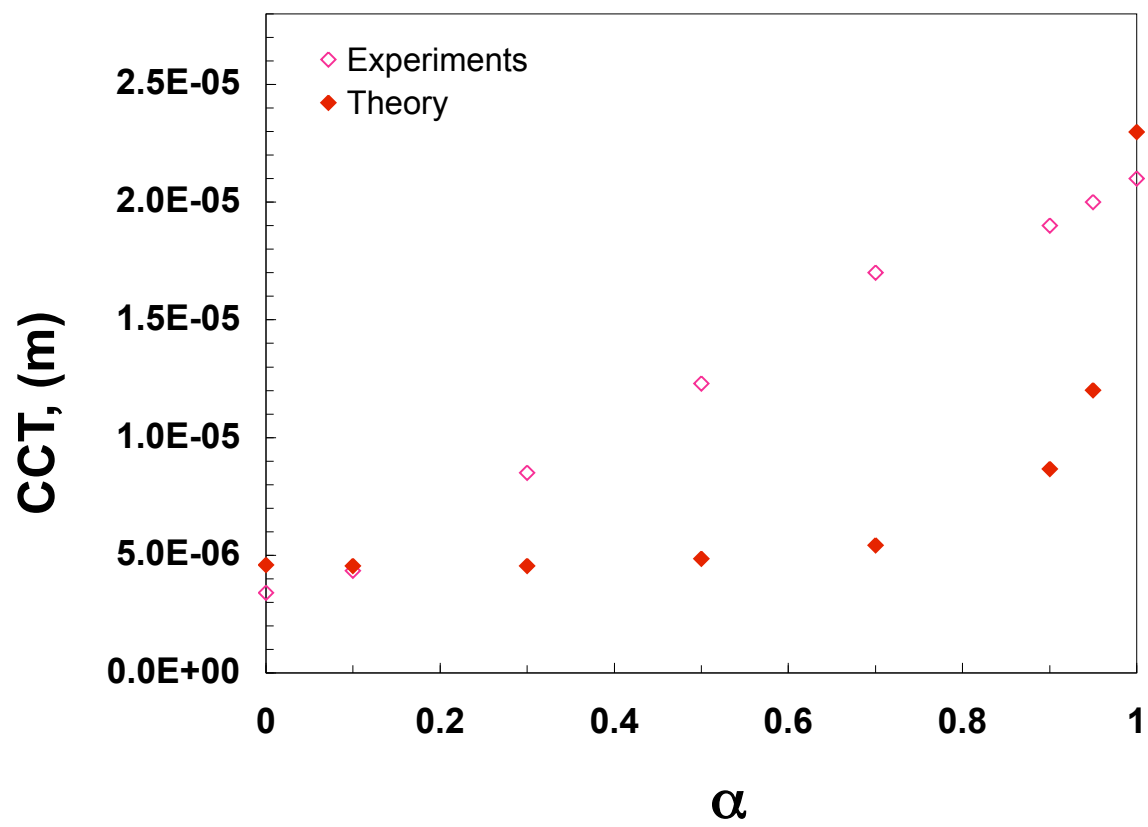


Figure 5.11: Comparison of experimental results for CCT with model predictions for different blends

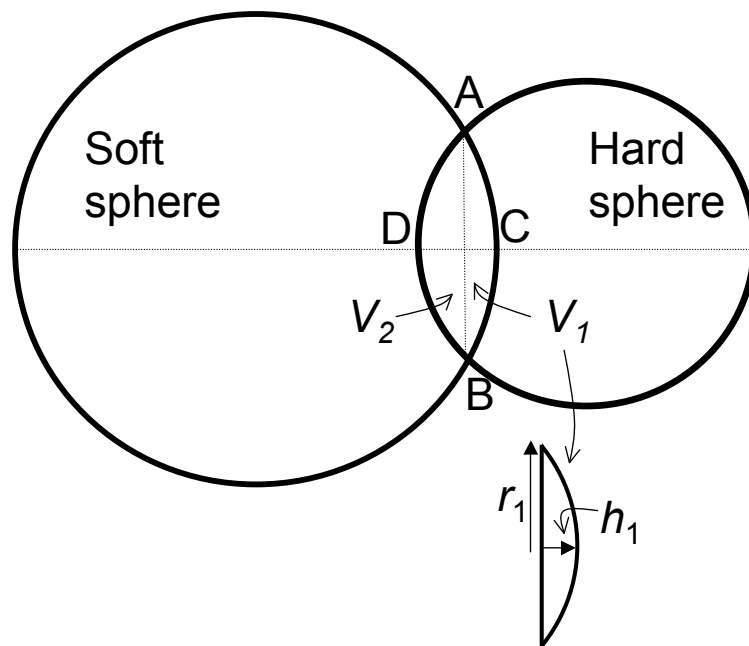


Figure 5.12: Sectional volumes, V_1 and V_2 .

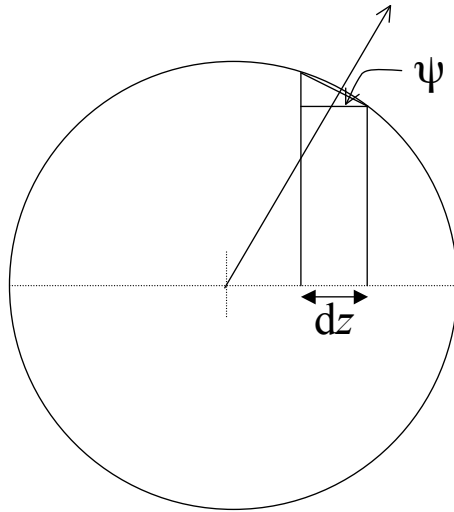


Figure 5.13: Calculation of area for the surface element.

CONCLUSIONS AND RECOMMENDATIONS

Chapter 6

CONCLUSIONS AND RECOMMENDATIONS

6.1 SUMMARY AND CONCLUSIONS

The work described in this thesis deals with the film formation and cracking in aqueous dispersions. The goal of the work was to get an in-depth understanding of the film formation process in water based dispersions. The various contributions of the present investigation are

- We have investigated the phenomena of cracking in drying films of stable colloidal dispersions. Here, two different regimes of cracking have been identified. It has been shown that based on the magnitude of compressive strain in the film, the mechanism of cracking could entirely be different. In the case of strain-limited regime, film formation leads to impermeable films where as in the case of stress-limited regime, film formation can yield porous crack free films. A universal theory for cracking of hard particle systems has been developed. It has been demonstrated that not only the particle properties but the way they pack during drying can also influence their cracking behavior.
- The film formation in drying films of flocculated dispersion was studied next. It has been shown that the theory that was developed for the stable dispersions is equally capable of describing the cracking behavior of flocculated dispersions as

well. Here, the importance of particle packing on critical cracking thickness is demonstrated over a wide range of pH values.

- The final part of the thesis deals with the soft-hard latex blends. Here, a mathematical model for the film formation in latex blends has been developed. It has been shown that the governing equations for monodisperse identical particles are also applicable to the blends with simply replacing the shear modulus with the effective shear modulus given by the model.

6.2 RECOMMENDATIONS FOR FUTURE WORK

As stated above, the two regimes of film formation have been identified in this work. However, the experimental validations are done only for the stress-limited regime (hard particle systems). It would be interesting to carry out experiments on soft particles having glass transition temperature very close to the room temperature. This would help to validate the predictions of the strain-limited regime and thus would help in establishing the overall theory of film formation in aqueous dispersions.

For the case of soft-hard latex blends, the model is developed for the systems where soft particles deform elastically to engulf the hard ones. However, the experimental results show that the deformation in the soft particles were beyond the elastic limit. Hence a different experimental study with blends where soft particles undergo deformation within the elastic limit would help to check the overall validity of the model developed in this work. The results also highlight the need for understanding cracking in viscoelastic systems which are close to the real systems.

CONTRIBUTIONS:

PATENTS/PUBLICATIONS/CONFERENCES

CONTRIBUTIONS:

PATENTS/PUBLICATIONS/CONFERENCES

- ❖ **Karnail B. Singh and Mahesh S. Tirumkudulu**, Cracking in Drying Colloidal Films, *Phys. Rev. Lett. (PRL)*, **98**, 218302 (2007).
- ❖ **Karnail B. Singh, Girish Deoghare and Mahesh S. Tirumkudulu**, Film formation in soft-hard latex blends: Theory and experiments, *Langmuir*, **In press** (2008).
- ❖ **Karnail B. Singh, Laxman R. Bhosale and Mahesh S. Tirumkudulu**, Cracking in drying colloidal films of flocculated dispersions, *Langmuir*, **Under review**.
- ❖ **Karnail B. Singh and Mahesh S. Tirumkudulu**, Cracking in Drying Colloidal Films, *81st ACS Colloids and Surface Science Symposium*, University of Delaware, US (June 24-28, 2007).
- ❖ **Mahesh S. Tirumkudulu and Karnail B. Singh**, Cracking in Thin Films of Aqueous Suspensions: Experiments and Theoretical Considerations, *80th ACS Colloids and Surface Science Symposium*, Boulder, US (June 18-21, 2006).
- ❖ **Karnail B. Singh and Mahesh S. Tirumkudulu**, On understanding the Phenomenon of Cracking in Latex films, *CHEMCON*, Delhi, India (Dec 14-17, 2005).
- ❖ **Karnail B. Singh and Mahesh S. Tirumkudulu**, Film Formation and Cracking in Latex Dispersions, *Research Scholars Symposium 2008*, IIT Bombay, Mumbai, India (June 2008).

- ❖ **Karnail B. Singh and Mahesh S. Tirumkudulu**, Cracking in Drying Films of Aqueous Dispersions, A Poster presented at *Research Scholars Symposium 2007*, IIT Bombay, Mumbai, India (Feb 2007).

AWARDS AND HONORS

AWARDS AND HONORS

- ❖ The work on “Cracking in Drying Colloidal Films” was reported in Physics Web & Physics World, the leading website and magazine of Institute of Physics (IOP) publishing house.
 - *Physics World, Vol. 20 (7), Page 5.*
 - *<http://physicsworld.com/cws/article/news/30117>.*
- ❖ A news story on this research work appeared in a leading Indian Newspaper, DNA dated *June 25, 2007, Page 9.*
- ❖ The research work was also cited on the front page of IIT Bombay Website.
- ❖ Received Best Poster award in Research Scholars Symposium held at IIT Bombay, February 2007.
- ❖ Selected among top 5 presentations during Research Scholars Symposium held at IIT Bombay, April 2008

ACKNOWLEDGEMENT

ACKNOWLEDGEMENT

*My first and the most earnest acknowledgement must go to my advisor **Prof. Mahesh S. Tirumkudulu** whose invaluable guidance and continuous support helped me in successful completion of my PhD. I owe a lot to him and would always be indebted for all his help and encouragement during my stay at IIT Bombay. This is due to all his efforts and motivation that I am able to materialize my four years of work into a PhD degree.*

I am also very much grateful to Prof. Kartic C. Khilar and Prof. Devang V. Khakhar who have always been there for any help and favor that I required during my stay in Fluid Mechanics Lab. I must also admit that all my Fluid Mechanics Lab mates were always very co-operative and have helped me a lot on many occasions during my experimental work. Special thanks to Arijit and Laxman for their help in experimental work on flocculated dispersions. Other than personal help, Fluid Mechanics Lab has always been an exciting place to work at. I feel happy to have been associated with such a large group of people who always maintain a congenial and enthusiastic atmosphere in the lab. Company of people like Rajitha, Prasad Prabhu, Subhasis and others has always made me happy and has never let me feel alone and low. They have always been very nice to me and my family and we have had a great and memorable time with them during my IIT days. I also take this opportunity to thank all my other friends such as Mantri, Laloo, Sunil, Dahe, Pravin, Makrand, Kirti, Vimal, Patro, etc who made my stay comfortable during my campus life.

Special thanks are further due to Prof. Vinay A. Juvekar and Prof. Kartic C. Khilar who were my RPC members and have spent their valuable time in evaluating my progress and giving some critical suggestions during

my PhD tenure. I also acknowledge Dr. S. L. Kamath of Metallurgical Engineering and Materials Science department and the people at SAIF for their support in analytical part.

It is a proud and privilege for me to be a member of the IIT family. I sincerely thank the Institute in general and the Department of Chemical Engineering in particular for providing me the infrastructure to carry out this research. I would also like to thank the Department of Science and Technology (DST) for providing me the financial assistance during my PhD programme.

My parents have always encouraged me to pursue higher studies. They have endured all the pains and put lot of efforts to make their kids reach the highest standards of life. Words would be insufficient to acknowledge their efforts in making me see this day. Further, I would also like to express my gratitude towards my in-laws who showed the courage and gave their only daughter to an unemployed person. Thanks for all their support and well-wishes.

My last and the most loving acknowledgement must go to my wife Seema and my daughter Ishu who have always been on my side irrespective of what it is. This is due to Seema's patience and understanding that I could devote sufficient time for my research.

..... **Karnail** 